

**OPTOACOUSTIC SYSTEM AND METHOD
FOR MESOSCOPIC IMAGING**

Dissertation

Andreas Oancea

2012

TECHNISCHE UNIVERSITÄT MÜNCHEN

Lehrstuhl für Biologische Bildgebung

Optoacoustic System and Method for Mesoscopic Imaging

Dipl.-Phys. Univ. Andreas Oancea

Vollständiger Abdruck der von der Fakultät für Elektrotechnik und Informationstechnik der Technischen Universität München zur Erlangung des akademischen Grades eines

Doktor-Ingenieurs

genehmigten Dissertation.

Vorsitzender: Univ.-Prof. Dr.-Ing. Werner Hemmert

Prüfer der Dissertation:

1. Univ.-Prof. Vasilis Ntziachristos, Ph.D.
2. Univ.-Prof. Dr. rer. nat. Franz Pfeiffer

Die Dissertation wurde am 29.01.2013 bei der Technischen Universität München eingereicht und durch die Fakultät für Elektrotechnik und Informationstechnik am 18.09.2013 angenommen.

COPYRIGHT

Andreas Oancea

2012

Optoacoustic System and Method for Mesoscopic Imaging

Abstract - English

In the last decade, optoacoustic imaging has emerged as a potent imaging method enabling to non-invasively study processes and structures at the interior of biological samples such as small animals. The method synergistically combines the advantages of optical imaging, i.e., high optical contrast with the advantages of acoustical imaging (sonography), i.e., high resolutions at large penetration depths.

This work targets the visualization of mouse tumor vasculature throughout entire subcutaneous solid tumors. To implement this task, a modular optoacoustic system for high resolution mesoscopic imaging (penetration depths up to 10mm, resolutions below 100 μ m) as well as various optoacoustic system setups based thereon were developed. By phantom experiments and theoretical calculations, the imaging performance of the system was evaluated for diverse experimental arrangements, and the setup arrangement best-suited for mouse tumor imaging was determined. Thereby, optoacoustic tomography proved to be the most advantageous method for imaging the tumor vasculature, owing to the high tomographic in-plane resolution.

For accurately adapting the experimental imaging parameters and reconstruction methods to the tumor, the tumor's physical properties were characterized. In a subsequent step, a tumor model exhibiting dense tumor microvasculature and heterogeneous structure was determined, the illumination and detection geometry was optimized, and suitable validation methods for confirmation of the optoacoustic tomograms were established by means of *post mortem* optoacoustic imaging experiments.

Based on the best results of the *post mortem* imaging experiments, an *in vivo* optoacoustic tomography experiment was designed and performed. Therein, the tumor vasculature was imaged intrinsically at various illumination wavelengths in the visible and in the near-infrared spectral range. By intravenous administration of nanoparticles, the contrast of the tumor vasculature in the near-infrared was at least doubled, which allowed visualizing the entire tumor vasculature. The biodistribution of the nanoparticles in the tumor was determined, wherein it was observed that the nanoparticles colocalized with the blood vasculature. The results were confirmed by optical imaging methods such as cryoslice imaging and fluorescence microscopy.

Although the optoacoustic imaging system was primarily developed for non-invasive imaging of tumors, its field of application is significantly wider. In additional biological imaging experiments, the imaging system showed to accurately visualize the head vasculature of a

mouse, zebrafish in the early developmental stage (less than 0.8mm high), Crustaceans such as Gammarus of various sizes, as well as tissue samples of animals such as pigs. Furthermore, the applicability of (X-ray) micro-CT for the validation of optoacoustic tumor images was investigated. Therefore, tumors were stained in an iodine-metaloxide solution post mortem after the optoacoustic imaging experiment, and subsequently imaged by micro-CT. The results indicate that such a method is suited significantly better for the validation of optoacoustic tumor images than the common optical methods.

Optoakustisches System und Verfahren für mesoskopische Bildgebung

Abstract - deutsch

Optoakustische Bildgebung hat sich im letzten Jahrzehnt als ein leistungsfähiges Bildgebungsverfahren herauskristallisiert, welches ermöglicht, Prozesse und Strukturen im Inneren von biologischen Proben, z.B. von Kleintieren, zu studieren. Das Verfahren kombiniert die Vorteile optischer Bildgebung, d.h. den hohen optischen Kontrast, den Vorteilen akustischer Bildgebung (Sonographie), d.h. mit den hohen Auflösungen bei großen Eindringtiefen, auf synergetische Art und Weise.

Diese Arbeit behandelt die Visualisierung von Maustumorvaskulatur durch ganze subkutane solide Tumoren. Zum Umsetzen dieser Aufgabe wurden ein modulares optoakustisches System für hochauflösende mesoskopische Bildgebung (Eindringtiefen bis 10mm, Auflösungen unter 100 μ m) sowie diverse darauf basierende optoakustische Systemaufbauten entwickelt. Anhand von Phantomexperimenten und Berechnungen wurde die Abbildungsleistung des Systems für verschiedene experimentelle Anordnungen ausgewertet und die für die Visualisierung von Maustumoren am besten geeignete Anordnung des Aufbaus bestimmt. Dabei stellte sich heraus, dass optoakustische Tomographie das vorteilhafteste optoakustische Verfahren für das Abbilden der Tumolvaskulatur ist, insbesondere dank der hohen tomographischen Auflösung innerhalb der Bildebene.

Um die experimentellen Bildgebungsparameter und die Rekonstruktionsmethoden an den Tumor anzupassen, wurden die physikalischen Eigenschaften des Tumors charakterisiert. In einem folgenden Schritt wurde ein Tumormodell, das eine dichte Mikrovaskulatur und eine heterogene Struktur aufweist, bestimmt, die Beleuchtungs- und Detektionsgeometrie optimiert und geeignete Validierungsmethoden zum Bestätigen der optoakustischen Schnittbilder anhand von *post mortem* optoakustischen Bildgebungsexperimenten etabliert.

Basierend auf den besten Ergebnissen der *post mortem* Bildgebungsexperimente wurde ein *in vivo* optoakustisches Tomographieexperiment entworfen und durchgeführt. Dabei wurde die Tumolvaskulatur intrinsisch bei diversen Lichtwellenlängen im Sichtbaren und Nahinfraroten abgebildet. Mittels intravenöser Applikation von Nanopartikeln wurde der Kontrast der Tumolvaskulatur im Nahinfraroten mindestens verdoppelt, was das Visualisieren der Vaskulatur des gesamten Tumors erlaubte. Die biologische Verteilung der Nanopartikel im Tumor wurde ermittelt, wobei beobachtet wurde, dass sich die Nanopartikel mit der Blutvaskulatur kolokalisieren lassen. Die Ergebnisse wurden anhand von optischen Bildgebungsverfahren, wie beispielsweise Cryoschnittbildgebung und Fluoreszenzmikroskopie, bestätigt.

Obwohl das Optoakustiksystem primär für die nichtinvasive Bildgebung von Tumoren entwickelt wurde, ist sein Anwendungsgebiet wesentlich größer. In weiteren biologischen Bildgebungsexperimenten bewies das Bildgebungssystem, die Kopfvaskulatur einer Maus, Zebrafische im Anfangsstadium der Entwicklung (weniger als 0.8mm hoch), Krustentiere, wie Gammariden in diversen Größen, sowie Gewebeproben von Tieren, wie Schweinen, genau visualisieren zu können. Ferner wurde die Anwendbarkeit von Röntgen-Mikrocomputertomographie (micro-CT) als Validierungsmethode für optoakustisch generierte Tumorbilder untersucht. Dazu wurden die Tumoren *post mortem* nach dem optoakustischen Bildgebungsexperiment in einer Iod-Metalloxidlösung gefärbt und anschließend mittels micro-CT analysiert. Die Ergebnisse verdeutlichen, dass solch ein Verfahren wesentlich besser für die Validierung von optoakustisch erzeugten Bildern geeignet ist, als es die üblichen optischen Verfahren sind.

Acknowledgements

The last three and a half years, in which I have performed the work presented in this thesis, have been very remarkable for me, and I am very grateful for having been given this unique possibility. I would like to thank everyone who has supported my work, especially during the times when system developmental processes required patience. In particular, I would like to thank the following people.

Being advised by the elite is probably the greatest wish of every PhD student. **Prof. Vasilis Ntziachristos** gave me this unique opportunity, for which I am very grateful. With his trust in my work, I sometimes found myself doing things which I had considered not to be possible at first. One of many examples for this was the optoacoustic imaging of a fish that was not even a millimeter high. His advice helped me to not lose the goals of this work out of sight, but stay on the right track, avoiding time-costly detours. Vasilis Ntziachristos was much more than just my advisor, he was a true mentor: a person having the answers to my questions, a pusher showing me deficits and instructing me how to permanently improve, and a visionary knowing where the path shall lead. Thanks to his support and openness to my ideas, I could perform promising novel investigations like proof-of-principle validation experiments for volumetrically validating optoacoustic images of tumors entirely *post mortem* by micro-CT. I truly enjoyed our scientific discussions on current topics of biomedical imaging, going far beyond optoacoustic imaging, but also on non-imaging subjects like diamonds and windsurfing; and I still hope for a rematch in table-soccer or table-tennis against Ursula Mühle and Katharina Lang.

I was in the exceptional position to receive support by not one, but even two excellent professors. I would therefore equally like to thank **Prof. Dr. Franz Pfeiffer** for supporting my work and providing me with a very valuable view on optoacoustic imaging from a different perspective. Also, I am very grateful for his support of the (co-operational) investigations on validations by micro-CT of stained samples. The discussions with Franz Pfeiffer at seminars, summer schools, colloquia, and meetings have always given me new impulses and ideas for further developing the system and performing new interesting experiments, and I am highly thankful for this.

Developing an optoacoustic system requires the purchase of many hardware parts. This work could therefore not have been realized without the assistance of the IBMI administration team, and I would like to thank especially **Silvia Weinzierl, Susanne Stern, Zsuzsanna Öszi, Christiane Ogorek, Dr. Andreas Murr, Dr. Veronika Erben, and Christian Wiest** for their efforts. Susanne Stern and Zsuzsanna Öszi, I would also like to thank a lot for assisting the administrative procedure of my PhD.

Working in such a fast-growing group as the optoacoustics group of IBMI was a very special experience for me, and I enjoyed the group internal dynamics a lot. Discussing procedures and results with other group members was very valuable for me, and I would like to thank especially **Prof. Dr. Daniel Razansky** for supporting my work and awakening my enthusiasm for optoacoustic imaging. For the many scientific discussions on optoacoustic and other biomedical imaging, for being a work partner and sometimes a challenger, and for sharing basically all highs and lows of our time as PhD candidates at the Helmholtz Zentrum München, I truly thank my dear long-time room mate **Rui Ma**. I am also truly thankful to **Dr. Jing Claussen, Michael Dobosz, Dr. Xosé Luís Déan Ben, Daniel Queirós, Stephan Kellnberger, and Dr. Amir Rozenal** for the many discussions and ideas that arose out of those discussions. I would like to thank **Miguel Angel Araque Caballero, Adrian Taruttis, Dr. Nikolaos Deliolanis, Andreas Bühler, Stefan Morscher, Dr. Jérôme Gâteau, Dr. Wouter Driessen, Dr. Karin Schäfer, Murat Omar, Xiaopeng Ma** as well as all other members of IBMI for all our discussions and for illuminating my work from different perspectives. For assisting with the cryoslice imaging system, I would particularly like to thank **Athanasios Sarantopoulos** and **Panagiotis Symvoulidis**; for assisting with the fluorescence microscope, I would like to thank **Karin Radrich**; and for assisting with preparation of the mouse tumors as well as mouse handling and immunohistochemical procedures I particularly thank the technical assistants **Sarah Glasl, Claudia Mayerhofer, Florian Jurgeleit, and Uwe Klemm**.

Many components of the system that I have developed required custom manufacturing. I thank the work shop team of the Helmholtz Zentrum München, in particular **Josef Promoli, Martin Scherer, and Thomas Gerlach** for their patience and prompt reaction.

I would also like to thank the administration of the Graduate School for Information Science in Health, particularly **Dr. Ursula Mühle** and **Katharina Lang**, for financial support, administrative support, and for providing a multi-disciplinary exchange platform. The sym-

posia, colloquia, seminars and discussions with other members have helped me to broaden my knowledge.

Great thanks goes to all my family and friends, especially **Tobias Lechner**, **Dr. Armin Höll-Steier**, and **Stefanie Berlin**, who were very patient with me when experiments or other work sometimes took longer than expected.

Probably the most support I have received during my time as PhD candidate came from my parents, **Olga Dana** and **Nikolaus**. They taught me not only to believe in what I have done, but also to do what I believe in, for which I am very grateful to them. I truly thank my parents for the 'Kampfgeist' that they have taught me, and for the extra portions of impulse that surely contributed to the completion of this thesis.

He who asks is a fool for five minutes, but he who does not ask remains a fool forever.

Confucius.

Contents

1	Introduction	1
2	Theory	9
2.1	General considerations	10
2.2	Propagation of light	11
2.2.1	Geometric optics in optoacoustic setups	11
2.2.2	Light diffusion in absorbing and scattering media	13
2.3	Acoustic wave creation and propagation	16
2.4	Considerations for biological tissue	18
3	Scanning and tomography methods	21
3.1	Scanning methods	22
3.1.1	General considerations on detectors.	22
3.1.2	Tomography with a line-focused transducer	23
3.1.3	Raster scanning with a point-focused transducer	24

3.2	Methods for reconstructing the initial pressure distribution	25
3.2.1	Cylindrical reconstruction methods	25
3.2.2	Cartesian reconstruction methods	28
3.3	Multi-spectral decomposition of absorbers' spatial distributions	29
3.3.1	Linear decomposition	29
3.3.2	Independent component analysis (ICA)	29
3.4	Empiric adaptations of the backprojection algorithm and image corrections . . .	30
4	Experimental arrangement and characterization	31
4.1	General considerations for development of the optoacoustic system	32
4.2	The open microscanning system	33
4.2.1	The hardware design	33
4.2.2	The illumination	36
4.3	System configurations and their characteristics	39
4.3.1	Components	40
4.3.2	Configuration designs for tomography	46
4.3.3	Configuration designs for raster scanning	50
4.4	Characterization by proof of concept experiments with phantoms	52
4.4.1	Tomography	52
4.4.2	Raster scanning	56

4.5	Conclusion for tumor imaging experiments	63
5	Optoacoustic tomography of tumor vasculature <i>post mortem</i>	65
5.1	Materials for experimental cancer imaging	66
5.1.1	Animals and tumors	66
5.1.2	Contrast agents for MSOT	70
5.2	The optoacoustic imaging experiments	73
5.2.1	Experimental procedure	73
5.2.2	Results	79
5.2.3	Discussion and conclusion	87
6	Optoacoustic imaging of tumor vasculature with natural and exogenous contrast agents, <i>in vivo</i>	95
6.1	Experimental procedure	97
6.1.1	Experimental arrangement	97
6.1.2	Image reconstruction	98
6.1.3	Animals and imaging	99
6.1.4	Validation studies	100
6.2	Results	100
6.2.1	Intrinsic contrast imaging of superficial microvasculature	100
6.2.2	Imaging in the near-infrared	102

6.2.3	Validation studies	104
6.2.4	Three-dimensional rendering	106
6.3	Discussion	107
7	Other applications	112
7.1	Tomographic optoacoustic imaging	112
7.1.1	Mouse head vasculature	112
7.1.2	Mouse subcutaneous tumor vasculature - superficial imaging	114
7.1.3	Zebrafish in early developmental stage	115
7.1.4	Gammarus imaging	121
7.1.5	Kidney nerve of a pig	124
7.2	Validation studies by micro-CT	124
8	Conclusions and Outlook	131
8.1	Conclusions	131
8.2	Outlook	133
	Bibliography	135
	Figures	144
A	Appendix	149

A.1	Light absorption by water and blood	149
A.2	PZT and PVDF ultrasonic detectors for optoacoustic imaging - a phenomeno- logical comparison	150
A.3	Supplementary results on <i>in vivo</i> imaging of tumor vasculature	152

Chapter 1

Introduction

Photoacoustic imaging is a hybrid imaging modality that synergistically combines the advantages of optical imaging and sonography, offering optical contrast at sonography-like imaging depths of multiple millimeters to centimeters and resolutions well below 50 microns. It is based on the photoacoustic effect:

Upon illumination of an absorber with an electromagnetic wave with time-variant intensity, the electromagnetic energy will be instantaneously converted to heat, causing thermo-elastic expansion of the absorber, and creating a radially propagating acoustic wave.

Photoacoustic imaging is generally classified into optoacoustic imaging, in which the electromagnetic wave is light in the ultraviolet, visible or near-infrared (NIR) spectral range, and thermoacoustic imaging, which uses radio-frequency electromagnetic waves to create images of magnetic permeability contrast instead of optical contrast. Even though the work presented herein handles optoacoustic imaging exclusively, many results and findings of this work are unrestrictedly transferable to radio-frequency excitation as well.

While the exciting electromagnetic wave is of transversal nature, the emitted ultrasonic wave is an acoustic wave with longitudinal character and the advantage of experiencing approximately two orders of magnitude less scattering and absorption. The optical contrast information is then preserved in the acoustic wave, essentially enabling an optical contrast view into

millimeters to centimeters of tissue far beyond the diffusion length of light. This unique feature has reserved photoacoustic imaging a position in the field of biomedical imaging, enabling a variety of biological and medical applications.

The history of optoacoustics dates back to 1880/81, when Alexander Graham Bell experimented with the transmission of sound by light in a device that he called the Photophone [1] [2]. Back then, he diverted pulses of (chopped) sunlight onto a selenium cell and listened to the emitted sound wave. It took almost another century though, until the method's full potential could be exploited. Until the 1970s, before the first optoacoustic image, the use of optoacoustics and its derivatives had been restricted to the spectroscopy of gases, liquids and solids [3] [4] [5] [6] [7]. The idea to perform spectroscopy also arose out of investigations by Bell, however from the Spectrophone (1881), a further development of the Photophone, which had been used for spectroscopy of solids. The early experimental designs employed high-intensity flashes of light from a gas discharge lamp for excitation of the sound wave. With the discovery of lasers in 1960, lasers took over the role of the illumination source, as the monochromatic, coherent and directional nature of laser light has allowed for more precise and versatile experiments. Subsequently to that key invention, the performance of photoacoustic spectroscopy systems was boosted. In consequence, for example in the detection of soot particles in exhaust, up to $10\mu\text{g}/\text{m}^3$ have become detectable, or, for example, in the field of gas spectroscopy, sensitivities of 10 parts per trillion (e.g. for sulfur hexafluoride) have become state of the art [8] [9]. Such high precision has turned photoacoustic spectroscopy into a key tool for investigations on pollution of the environment, like the processes that lead to the depletion of the ozone layer. More particular, since the terrorist attack with the nerve gas Sarin on the Tokyo metro in 1995, and recent terrorist actions, photoacoustic spectroscopy has even been considered for crime prevention. Regarding the spectroscopy of solids, photoacoustic spectroscopy has been used to detect down to 0.1 monolayers of SF_6 on a silver surface [10]. For these high sensitivities, and other reasons that will be described in the following, the potential of the optoacoustic effect was soon translated to the field of imaging. The laser technology has been a key (limiting) factor for optoacoustic imaging performance since then.

Utilizing the optoacoustic effect for biomedical imaging. The first optoacoustic images are dated back to 1978, when a group at Stanford University around Wickramasinghe modified

an acoustic microscope to an *optoacoustic* microscope by replacing the ultrasonic transmitter with a focused beam of a mode-locked or Q-switched Nd-YAG laser [11]. In that experiment, a thin, structured metallic foil was scanned by moving the sample between the confocal optical excitation and the acoustic detector in transmission geometry. Although the achieved optoacoustic imaging resolution of two microns was remarkably high, the differences between the optoacoustic images and the correspondingly presented validation images were significant. Especially the limitations in transducer, acquisition, and evaluation technology were the reasons for this. Nevertheless, the setup contained not less components than today's state-of-the-art optoacoustic microscopy setups.

In the subsequent decade, various optoacoustics-based microscopy techniques were presented. Photodisplacement microscopy is one example thereof [12] [13] [14] [15]. Mostly applied in material science for non-destructive surface and subsurface inspection of solids like silicon, photodisplacement microscopy is capable of visualizing the height profile with sub-micrometer precision by interferometric detection of the propagating ultrasonic wave. Many of those microscopy techniques still play a major role in today's material science [16]. The transition of optoacoustics from being only a method for non-destructive material testing to also being applied for biomedical imaging occurred in the 1990s. At first, optical properties of tissue were determined optoacoustically [17]. Key technologies necessary for this transition were especially the further development of giant-pulse lasers, high-frequency and -sensitivity ultrasound detectors and computing capacity.

In consequence, it did not take much time until optoacoustic imaging of tumors found attention, setting the base for biological investigations that had afore been reserved for radiological, ionizing or invasive imaging methods [18]. Also around the turn of the millennium, reconstruction algorithms for performing optoacoustic tomography were presented. Among all biomedical imaging modalities that are applicable for preclinical mesoscopy, like X-Ray computed tomography (XCT) or magnetic resonance imaging (MRI), optoacoustic imaging has the following unique advantages:

1. Non-ionizing electromagnetic radiation.

Since the illumination is not harmful for tissue, assuming a suitable light intensity, it is expected that any tissue sample would neither suffer from changes throughout the experiment, nor in the long term. Therefore, it also applies:

2. Applicability for *in vivo* experimentation.

Biological processes, like the growth of tumors, are time-variant. In order to deduce valid statements regarding their development, it is, therefore, advantageous to image the same organism in longitudinal studies.

3. Non-invasive deep-tissue imaging of optical contrast.

Superior to conventional optical imaging methods like intravital imaging, the optical contrast vision through tissue provided by optoacoustic imaging does not require the implantation of glass windows in the skin.

4. Molecular specificity by multispectral optoacoustic imaging (MSOT).

Molecular imaging has witnessed increasing importance in biomedical research. It refers to the visualization of the biodistribution of biomarkers upon injection. MSOT uses absorption images of different illumination wavelengths to decompose the spatial distributions of the comprising absorbers.

5. Scalability.

Similar to sonography, optoacoustic imaging setups may be designed for specific penetration depths and corresponding resolutions. Given that the sound attenuation increases with frequency, large penetration depths require low frequencies, thus provide lower resolution. Nevertheless, the span of applications is manifold; up to 70mm penetration depth or below 5 micrometers resolution have been achieved.

6. Cost-effectiveness.

Optoacoustic imaging fills the gap for comparably cheap imaging of soft tissue contrast well below the tissue surface. Before the time of biomedical optoacoustic imaging, deep-tissue visualization of soft tissue was generally reserved for MRI, which requires expensive instrumentation.

7. Applicability for real-time three-dimensional imaging.

While for general investigations on optoacoustic imaging single element transducers are mostly in use because of their variety of nominal parameters, *in vivo* experiments require shorter acquisition times. Multi-element detectors are, therefore, specifically developed in order to avoid the time-consuming scanning of a single element detector, allowing for even three-dimensional real-time imaging.

These advantages have been exploited in a large variety of studies, most of them addressing the

biodistribution of blood or biomarkers in humans and small animals [19] [20] [21] [22].

State of the art in preclinical cancer imaging. The average distance a photon travels through skin before it is scattered is in the order of, depending on tissue and light wavelength, less than a few hundreds of micrometers [23]. Preclinical optical imaging of cancer is, therefore, not capable of accurately visualizing tumors that are thicker than a few hundreds of micrometers, limiting the method's applicability to skin melanoma or the like [21]. Beyond non-invasive optical inspection of tissue, histology has been a gold standard investigation method for a long time [24]. Especially in combination with immunochemistry and fluorescent probes, histology has allowed studying biological mechanisms of tumor growth [25]. On the other hand, by means of macroscopic (typically NIR) fluorescence imaging, tumors could be precisely localized during clinical trials - an approach which recently has shown success in intra-operative imaging [26]. Nevertheless, strong scattering of tissue also denied this method detailed insights into the tumor heterogenic structure. One approach for imaging deeper into tumors was presented in the 1990s by Jain et al. [27] [28] [29]. They visualized biological processes like tumor neoangiogenesis by optical microscopy through a glass window that had been implanted into the skin of a mouse. Also, radiologic methods like micro-CT or MRI have been used to visualize the tumor microvasculature, but their experimental disadvantages such as low contrast mechanisms or long measurement durations restrict their applicability to validation purposes [30].

With the impact of optoacoustic imaging, intra-tumoral heterogeneities could be visualized non-invasively with optical contrast. Thereby, a steady increase in the resolutions and penetration depths has been observed. For various applications, like cancer imaging, tomographic as well as raster scanning methods have been employed so far, while three-dimensional tomography has been the exception [31]. In mesoscopic imaging (1-10mm imaging depth), three-dimensional tomography has been applied for imaging adult zebrafish [20]. More efforts for three-dimensional imaging have been done by raster scanning of focused laser beams over samples like mouse ears to achieve diffraction-limited optical resolutions, usually termed optical resolution photoacoustic tomography (OR-PAM) [21]. In order to exceed the attributed low penetration depths (a few hundred micrometers) to the domain of mesoscopic imaging, though, acoustic resolution photoacoustic microscopy (AR-PAM) has been proposed. As dark field microscopy, it has been used to investigate the subcutaneous vasculature on the back of small

animals, which sample is well-suited for being scanned by AR-PAM. Due to the coaxial ring illumination geometry, application to subjects of interest with small radii, such as subcutaneous mouse tumors, could not be demonstrated yet. Furthermore, despite the superior penetration depths of AR-PAM (as compared to OR-PAM), the tight focusing of the ultrasonic (point) detector limits the depth of the field of view to subjects as thin as melanoma or tumors in the early stage of growth (less than five days) for high resolution imaging [32]. Larger tumors and physiological human subcutaneous vasculature have been investigated by optoacoustic technologies based on optical interferometry for the ultrasound detection, but the achieved lower resolution constrained this method's imaging performance to the level of the large blood vessels instead of tumor fine structure [33]. Optoacoustic tomography on the other hand has been, for example, applied to image progression of subcutaneous vasculature in the early stage of tumor growth. Since the system design has been based on the same two-dimensional imaging geometry as for tomography of small animal head vasculature [21], the image resolutions were low, and no insights into tumor heterogeneity were obtained. Thereby, only the vasculature lying 400 μm below the skin surface, a depth commonly attributed to the subcutis, was investigated [34].

The work presented herein focuses on **non-invasive imaging of cancer**, particularly for preclinical research. Even today, in the time of advanced imaging modalities, the success of tumor therapy is often determined by measuring the sizes of tumors with calipers. If adequately employed, calipers do not harm the tumor, and they are, hence, applicable for non-invasive *in vivo* investigations. However, to obtain more detailed insights on tumor growth processes, and on the effect of medication against tumor growth, visualization of the tumor interior is indispensable. In particular, the shape and distribution of the tumor vasculature is of interest for biological angiogenesis studies.

Tumor growth strongly correlates with the development of vasculature (neoangiogenesis). In the early stage of tumor growth, the tumor is supplied with nutrition and oxygen via diffusion through the surrounding tissue. After the growing tumor has reached a volume of a few cubic millimeters, the supply by diffusion is not sufficient for further growth. Therefore, the tumor sends out growth factors such as the Vascular Endothelial Growth Factor (VEGF) that causes the genesis of blood vessels towards in the tumor region. In conclusion, tumor growth can be suppressed, if angiogenesis is suppressed, providing the key for modern tumor therapy. Along this path, optoacoustic imaging provides insights to the development of blood vessels non-invasively, *in vivo*, and with high resolution. Therefore, by imaging the tumor vas-

culature, the tumor's reaction to tumor therapy is directly indicated. Hence, imaging the tumor vasculature provides a basis for biological investigations on the progression of cancer and the effectiveness of treatment methods, which constitutes the core of this work.

Tumor vasculature has formerly been visualized by purely optical imaging modalities, which play an important role in cancer research. Thereby, a large part of optical cancer imaging is performed by microscopy methods, which offer high resolution interrogation of volumes that are typically smaller than a cubic millimeter. However, many events during tumor development or treatment occur at depths larger than 1 mm. By employing optoacoustic mesoscopy as a tool for anatomical and functional optical imaging of entire experimental solid tumors, achieving better than 40 micrometer resolution, the visualization of depths below 1mm is enabled. This work, in particular in chapter 6, discusses how mesoscopic optoacoustic imaging enables a new cancer investigation approach, examining optical contrast through entire tumors.

The **goal** of this work is, therefore, to provide a method and system that allow for **high resolution visualization of whole mouse tumors three-dimensionally, non-invasively, and *in vivo***. To achieve this, first a modular optoacoustic setup was developed that exceeds the tumor imaging performance of state-of-the-art optoacoustic systems with respect to resolution, penetration depth, three-dimensionality, and other parameters. After characterizing the system and its components, the system was applied to reproduce scientifically accepted *post mortem* small animal experiments and phantom experiments. Although the system was mainly conceived for imaging mouse subcutaneous tumors, its applicability for imaging of other species of small animals, for example zebrafish or Gammarus, and for further *ex vivo* biomedical imaging, for example tissue of pigs, was investigated in various experiments. Both scanning geometries, raster scanning as well as tomography, were further developed, and their applicability to various subjects of interest was assessed in calculations and experiments. Thereby, the technologically most advanced setup arrangement of backward detection was mainly applied (cf. [35]). In the backward detection configuration, the sample is illuminated from the same direction as the acoustic wave is detected.

Although optoacoustic imaging can generally be performed in various ways, for example with single-element detectors or multi-element detector arrays, with modulated lasers or nanosecond Q-switched pulsed lasers, at single or multiple illumination wavelengths, etc., the framework conditions of this work are defined to nanosecond pulse illumination in the visible

and NIR spectral range, and single-element detection. As coupling medium serves distilled water. Transferability to other specifications is generally given, but may require adaptations. This thesis demonstrates how optoacoustic imaging performance is improved by precise adaptation of the illumination and ultrasound detection to the sample of interest, i.e. under consideration of all known or determined physical properties of the sample and propagation media. **Chapter 2**, therefore, discusses the physical processes occurring along the path of energy transmission: from the propagation of the laser pulse through the different media to the sample of interest, the optoacoustic creation of the ultrasonic wave, and the propagation of the ultrasonic wave to the ultrasonic detector. Furthermore, limitations due to realistic properties of small animal tissues, such as their heterogeneous character, are described therein. Based on these theoretical considerations, **chapter 3** discusses algorithms for reconstruction of the initial pressure distribution in tomographic and raster scanning geometries. In addition, analytically and empirically derived adaptations of the reconstruction algorithms are described therein. The subject-matter of chapters 2 and 3 constitutes the theoretic basis for all experimentation of this work. **Chapter 4** focuses on describing and characterizing the developed optoacoustic system (including setup configurations) by calculations, characterizing measurements and phantom experiments. Altogether, chapters 2, 3, and 4 describe the development of the optoacoustic system to be used for the biological and proof-of-principle experiments discussed in chapters 5, 6, and 7.

The main aspect of the biological imaging experiments presented in this work is the imaging of optical contrast in different tissues. In particular, intrinsic contrast agents, such as hemoglobin or skin pigments, as well as extrinsic contrast agents, such as fluorochromes, chromophores, and nanoparticles, are imaged in phantoms and small animals. **Chapter 5** discusses the optoacoustic imaging of a set of tumors of diverse cell lines and growth durations in diverse system configurations. The intention is to assess a well-suited combination of experimental parameters for *in vivo* imaging of mouse tumor vasculature according to the goal of this thesis. Such *in vivo* experimentation is discussed in **chapter 6**, wherein the vasculature of a HT29 tumor is investigated optoacoustically in a plurality of ways to evaluate the self-consistency of the results, and the experiments are further confirmed by optical validation and immunohistochemical methods. In **chapter 7**, other biological optoacoustic imaging experiments are presented, indicating the wide range of investigations that the setup is applicable for, comprising, for example, imaging of a few days old zebrafish (less than 1mm thin). **Chapter 8** finally provides conclusions, and offers an outlook for potential steps to overcome the limitations witnessed in this work.

Chapter 2

Theory

Optoacoustic imaging is based on a complex interplay of many physical effects. This chapter reviews these effects along the energy propagation path. Important general considerations on the physical processes involved in optoacoustic imaging in biomedicine, as well as their relevance for developing an efficient, elaborate optoacoustic setup, are provided in **section 2.1**. **Section 2.2** of this chapter discusses the physics of light (pulse) propagation from the laser to the specimen, as well as the light diffusion into the specimen. The subsequent **section 2.3** continues with a mathematical description of the optoacoustic effect and of the radial expansion of the ultrasonic wave. Up to that point, certain assumptions are made in order to be able to solve the underlying mathematical problems analytically. How biological tissue may not meet those assumptions, and what this implies for the resulting optoacoustic images, is shortly discussed in **section 2.4**.

Essentially, this theory chapter summarizes and reviews publications by Vo-Dinh et al. [23] regarding the entire light propagation, Wang et al. [36] [37] for the optoacoustic conversion, and Szabo et al. [38] concerning the (ultra)sound propagation, while the contents of those publications partly overlap. As background for developments derived from ultrasound imaging serves the book by Angelsen [39]. The reader is referred to the literature for further details. Formulations not addressed therein are derived ab initio in this thesis.

2.1 General considerations

Upon its emission, the nanosecond laser pulse is redirected and shaped by optical components, such as mirrors, lenses, beam splitters, fibers, and fiber bundles, in order to illuminate the sample in the desired way. To design an optoacoustic system energy- and cost-efficiently, the overall losses due to reflections or transitions between media of different refractive indexes are to be minimized. This becomes particularly important, if the functionality of the setup shall not be restricted to one wavelength, but extend over the visible (e.g., 532nm) and the NIR (e.g., 700nm to 900nm), because off-the-shelf highly reflective or transmissive optical coatings cannot cover such a large wavelength band. Yet before the light diffuses into the sample, and before it is converted to sound by the optoacoustic effect, the laser pulse has to cross at least an air-water-interface and a water-sample-interface, eventually also additional water-membrane / membrane-sample-interfaces. Such interfaces, i.e. sources of losses, are evaluated as described by the formulations in the next sections when developing the optoacoustic setup. Once the water-sample-interface is crossed, the light pulse propagates into the sample. In addition to the exponential decrease in intensity with penetration depth, according to the Beer-Lambert law, the light is also scattered, potentially to regions out of the focus of the detector. Assessing the overall intensity decrease with depth will, therefore, be helpful for optimizing the reconstruction methods.

Biological material is rarely optically or acoustically homogeneous. The size and spatial distribution of inhomogeneities, however, is generally known, and shall, therefore, be taken into consideration for the experimentation (e.g. for illumination arrangement) and the reconstruction. Examples for such heterogeneities are the thorax of a mouse with the lungs containing alveoli (gas-tissue-interface), or the limbs of a mouse with the bone surrounded by muscle and soft tissue. Each of these acoustic impedance mismatches act as interfaces, causing reflections that may lead to artifacts in the images. To avoid such artifacts, measures such as precise adaptation of the illumination and detection geometry to the sample, or optimization of the orientation of the sample, are taken. Generally, scanning through such interfaces was avoided in this work. Therefore, a particularly advantageous sample witnessing a reduced amount of such reflections is investigated - i.e. a subcutaneous tumor. In the case of subcutaneous tumors, typically the just thin skin (see chapter 6) separates the acoustically (in first approximation) homogeneous tumor mass from the surrounding water.

As optoacoustic imaging is an absorption-contrast-based imaging modality, re-emission effects like fluorescence are primarily negligible. In summary, the discussion of the relevant optical processes, therefore, focuses on refraction, reflection / transmission, absorption and scattering to deduce the excitation and propagation of the acoustic wave accurately.

2.2 Propagation of light

2.2.1 Geometric optics in optoacoustic setups

Upon emission, the nanosecond pulse of laser light propagates first through air with refractive index $n_0=1$ and speed of light in air $c_{air} \approx c_0=3 \times 10^8$ m/s. The subsequent transition to water is subject to refraction, according to Snell's law:

$$\frac{\sin(\theta_1)}{\sin(\theta_2)} = \frac{c_1}{c_2} = \frac{n_2}{n_1}. \quad (2.1)$$

Therein, θ are the angles of incidence versus the normal and n represent the refractive indexes, with the values for water and glass being (in best approximation) $n_w=1.33$ and $n_g=1.51$. In optoacoustic imaging, the sample necessarily needs to be surrounded by an optoacoustic coupling medium, such as water. For shaping the laser beam by means of glass lenses under water, however, the focal lengths of the lenses have to be re-evaluated for under water use. If only the refractive index and the focal length of a lens, e.g. a spherical lens, on air are known, the respective thin lens equation is derived as follows.

Considered is a transition from medium 1 to medium 2 and from medium 2 to medium 3, wherein medium 2 is glass. The glass lens shall at first be a thick lens with curvatures r_1 at the entry side and r_2 at the exit side; directionality is parallel to the light propagation, which is why r_2 is negative.

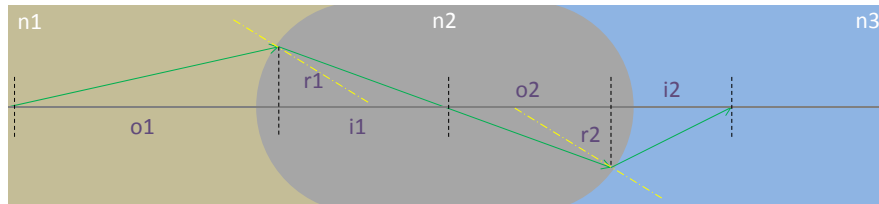


Figure 2.1: Schematic of a thick spherical lens (n_2).

Furthermore, the object distance o is defined as the distance between the object and the refraction plane, and the image distance i is defined as the rest of the distance between the object and the image (e.g. o_1 : object distance of transition from n_1 to n_2). Moreover, a large lens (paraxial) approximation is assumed ($\sin(\alpha) \approx \alpha$, $\cos(\alpha) \approx 1$). With Snell's law and geometric considerations, the formula for refraction on the first spherical surface is:

$$\frac{n_1}{o_1} + \frac{n_2}{i_1} = \frac{n_2 - n_1}{r_1}. \quad (2.2)$$

The transition on the opposite surface of the presumably thick lens is described accordingly, and summation of these two formulas results in the general equation for a thick lens:

$$\frac{n_1}{o_1} + \frac{n_3}{i_2} = \frac{n_2 - n_1}{r_1} + \frac{n_3 - n_2}{r_2}. \quad (2.3)$$

Out of this equation is derived the classical thin lens equation as the special case of $o_1 \rightarrow \infty$, $i_2 = f$ and $n_1 = n_3$ [40]:

$$\frac{1}{f} = \left(\frac{n_2}{n_1} - 1 \right) \left(\frac{1}{r_1} - \frac{1}{r_2} \right) \quad (2.4)$$

In this case, the focal length will increase when water instead of air is the ambient medium with refractive index n_1 :

$$f' = f \cdot \frac{n_1' \cdot (n_2 - n_1)}{n_1 \cdot (n_2 - n_1')} = f \cdot 3.8. \quad (2.5)$$

Beyond refraction, reflection is another relevant effect along the propagation path, and, depending on the sample, eventually also at the interface between the coupling medium and the sample. The physical description is represented by the four Fresnel equations, as derived, for example, in [41]. The reflectance R , defined as the transmitted fraction of light intensity, of a wave with E-field vector perpendicular to the refraction plane, which represents the case relevant for the setup presented herein, is calculated by:

$$R_{\perp} = \left| \frac{n_1 \cos \theta_1 - n_2 \cos \theta_2}{n_1 \cos \theta_1 + n_2 \cos \theta_2} \right|^2. \quad (2.6)$$

Assuming no absorption occurs at the interface ($A = 0$), the respective transmittance according to energy conservation is $T = 1 - R$. Since the laser pulse energy is limited, this formulation is taken into account in the setup development process, in order to reduce avoidable losses. For example, at the surface of the coupling medium, an incidence angle of 45° would increase the reflection losses to 5.2% compared to the standard 2% for perpendicular incidence ($\theta = 0$)

(calculation according to equation 2.6 for air-water boundary).

One special optical component, used to create rings of light in the developed setups, are conical lenses, so called axicons. Formulas for their most relevant parameters, namely the radius of the ring and the aperture angle, are again derived from Snell's law and geometrical considerations for collimated light at the entry side.

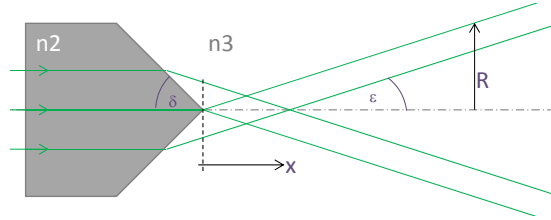


Figure 2.2: Schematic of a conical lens (axicon) with geometrical optics.

In the above nomenclature, the aperture angle on the image side ϵ can be expressed as a function of the lens's half apex angle δ :

$$\epsilon = \arcsin\left(\frac{n_2}{n_3} \cos\delta\right) - 90 + \delta. \quad (2.7)$$

The outer radius of the ring is, consequently, $R = x \cdot \tan(\epsilon)$.

2.2.2 Light diffusion in absorbing and scattering media

While absorption and scattering are negligible along the path through air, they become significant under water or in biological tissue. Due to the comparably long distance that a photon travels in technically distilled water before it witnesses the first scattering event, also referred to as the scattering mean free path, scattering shall only be taken into account in the tissue. Therein, light is described in the particle model, rather than as an electromagnetic wave, thus, prohibiting interference. The photons constitute a light intensity distribution, which may be under certain conditions derived analytically from the Boltzmann equation in the Radiation Transport Model. For the special case of a homogeneous, absorbing, non-scattering medium though, the absorption coefficient μ_a is derived directly by introducing the absorption cross section σ_a (in area units), as the cross section necessary to absorb a certain amount of power P_a of the light beam with irradiance I (in power per area). With the the number density of

absorbers ρ_a , it follows:

$$\mu_a = \frac{P_a}{I} \cdot \rho_a = \sigma_a \cdot \rho_a. \quad (2.8)$$

Assuming a homogeneous absorber, the irradiance is expected to decrease according to $dI = -\mu_a \cdot I$, which yields the classical Lambert-Beer law after integrating over a path of length z :

$$I(z) = I(z = 0) \exp[-\mu_a z]. \quad (2.9)$$

For the scattering environment, the diffusion equation is derived for scattering coefficients that are much larger than absorption coefficients $\mu_s \gg \mu_a$, which holds for the biological tissues investigated in this work. Assuming a package of photons is at time point $t_0 = 0$ in the origin of the laboratory coordinate system, has a radiance L_0 [$\text{W}\cdot\text{m}^{-2}\cdot\text{sr}^{-1}$] with impulse along the unit vector \hat{s} , and expands into the semi-infinite scattering medium (e.g. tissue), the governing Boltzmann equation for the radiance L at position \vec{r} , time t , and in direction \hat{s} is given by:

$$\begin{aligned} \frac{1}{c} \frac{\partial L(\vec{r}, \hat{s}, t)}{\partial t} = & -\hat{s} \cdot \nabla L(\vec{r}, \hat{s}, t) - (\mu_a + \mu_s) L(\vec{r}, \hat{s}, t) + \\ & + \frac{\mu_a + \mu_s}{4\pi} \int_{4\pi} p(\hat{s} \cdot \hat{s}') L(\vec{r}, \hat{s}', t) d\Omega' + Q(\vec{r}, \hat{s}, t). \end{aligned} \quad (2.10)$$

Regarding only the left side and the first term on the right side, this represents the continuity equation: The larger the intensity gradient is in direction \hat{s} , the faster is the decrease in intensity. The second term on the right side handles the photons that are scattered away from the direct path or have been absorbed, and the third term refers to the photons that witnessed multiple scattering to re contribute to the radiation at position \vec{r} in direction \hat{s} , where p is the so called scattering phase function that describes the probability for a scattering process from \hat{s} to \hat{s}' . The final term Q handles the illumination source [23].

Although the optoacoustic effect necessitates a non-stationary light distribution, the time scale of photon propagation throughout the region of interest in the sample is by more than two orders of magnitude shorter than the typical duration of the excitation pulses, which is why the time dependency can be modeled as an envelope, and the intensity distribution can be approximated as stationary. For dominance of the scattering over absorption, the diffusion equation is derived from the Boltzmann equation after approximation by a first order expansion of the radiance into spherical harmonics, hence, elimination of the unit vector \hat{s} . Instead of

regarding the directional radiance, the Boltzmann equation is simplified to an expression in the total fluence rate $\Phi(\vec{r}, t)$:

$$\frac{\partial}{\partial t}\Phi_d(\vec{r}, t) = D\nabla^2\Phi_d(\vec{r}, t) - \mu_a c\Phi_d(\vec{r}, t) + Q_c + Q_d. \quad (2.11)$$

The anisotropy g , describing the average cosine of scatter, is then contained in the diffusion constant D , as are μ_a and μ_s :

$$D = \frac{1}{3 \cdot ((1 - g)\mu_s + \mu_a)} = \frac{1}{3 \cdot (\mu'_s + \mu_a)}. \quad (2.12)$$

While in isotropic media, the integral of all cosines cancels out to zero, g takes values between 0.6 to 0.99 for tissue, meaning that the light scattering is highly anisotropic, i.e., particularly directed forward. The variables Q_c and Q_d are the coherent and diffuse source terms.

A time-dependent solution is deduced analytically for the instantaneous injection of a photon package into the infinitely extended diffuse medium [23]:

$$\Phi_d(\vec{r}, t) = E_0 \frac{c}{(4\pi cDt)^{3/2}} \exp \left[- \left(\frac{r^2}{4Dct} + \mu_a ct \right) \right]. \quad (2.13)$$

Here E_0 [J] is energy of the incident light package. The package travels at the speed of light c , which has to be evaluated in the medium according to $c = c_0/n$, wherein n is the refractive index of the medium or tissue, and c_0 is the speed of light in vacuum. The second exponential term is nothing more than part of the above derived Lambert-Beer law, describing the absorption along the path of an 'average' photon. With this equation, the radiance distribution within the sample is estimated, which is most useful for assessment of ideal illumination conditions during the system design process, but also for post-processing by light distribution corrections, for example, as described in [42].

An evaluation of the fluence rate after instantaneous injection of the incident light package (photon package) for optical parameters of moderately scattering and absorbing tissue ($\mu_a=1.15/\text{cm}$, $\mu_s=10/\text{cm}$, $n=1.4$ for skin) is illustrated in Fig. 2.3. It is shown how instantaneously the light fluence reacts to changes in illumination. In values, after one tenth of a nanosecond, the fluence rate (e.g. at the surface) reduces to 0.3% of its initial value. In the optoacoustic experiments performed in this work, the laser pulses are, however, approximately 8ns long, so that the true change in fluence rate is caused by the laser pulse time profile only,

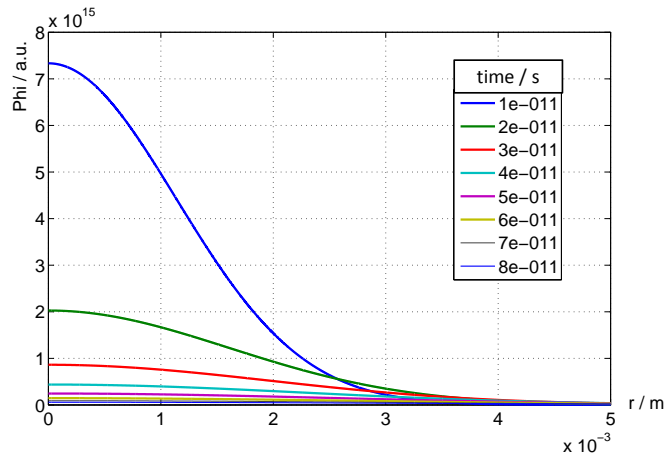


Figure 2.3: Fluence rate distribution in arbitrary units after initial injection of a photon package of energy E at $t=0$.

and the propagation duration of the pulse in the semi-infinite medium is negligible. Referring to the delta pulse, immediately after injection of the package the fluence rate is highest at $r=0$. With increasing duration, the pulse propagates towards larger r , causing the fluence rate gradient to decrease, indicating a more homogeneous fluence distribution. In summary, for the parameters assigned in this evaluation, imaging depths of less than 4mm appear reasonable with respect to penetration depth.¹ Well-designed illumination geometries, as will be described in the following chapters, are able to extend these imaging depth boundaries.

2.3 Acoustic wave creation and propagation

The energy conversion from electromagnetic (light) energy to the acoustic wave occurs significantly faster than the stress relaxation or heat diffusion. Due to inertia of the sample, this process is physically an isochoric pressure rise / change. The ignition in an internal combustion engine serves as an illustrative analogon hereto. When the gasoline-air mix is ignited, heat is brought into the system, and because of the piston's inertia, the temperature increase leads to an instantaneous pressure increase. Generally, stress and thermal confinement are provided. With only a few principles of mechanics of continua, the differential equation governing the acoustic propagation is derived. At first, the medium displacement $\vec{\xi}$ in dependence of pressure

¹Assumption: a point source at $r=0$, and radial expansion of the light pulse into the semi-infinite half space.

p and temperature T is considered according to the generalized Hooke law:

$$\nabla \cdot \vec{\xi}(\vec{r}, t) = -\kappa p(\vec{r}, t) + \beta T(\vec{r}, t). \quad (2.14)$$

Therein κ and β represent the isothermal compressibility in [1/Pa] and the isobar coefficient of thermal expansion in [1/K]. Application of a Nabla operator to Newton's second law of motion,

$$\rho \frac{\partial^2}{\partial t^2} \vec{\xi}(\vec{r}, t) = -\nabla p(\vec{r}, t), \quad (2.15)$$

in which ρ is the density, and substitution of equation 2.14 into 2.15 yields the **general photoacoustic equation**

$$\left(\nabla^2 - \frac{1}{v_s^2} \frac{\partial^2}{\partial t^2} \right) p = -\frac{\beta}{\kappa v_s^2} \frac{\partial^2}{\partial t^2} T \quad (2.16)$$

with the constant speed of sound $v_s = 1/\sqrt{\kappa\rho}$. The condition of thermal confinement is then exploited by regarding the converted thermal energy, the so called heating function H ,

$$\rho C_v \frac{\partial T(\vec{r}, t)}{\partial t} = H(\vec{r}, t), \quad (2.17)$$

yielding the simplified photoacoustic equation

$$\left(\nabla^2 - \frac{1}{v_s^2} \frac{\partial^2}{\partial t^2} \right) p(\vec{r}, t) = -\frac{\beta}{C_p} \frac{\partial}{\partial t} H(\vec{r}, t). \quad (2.18)$$

Therein C_v represents the specific heat in [J/(kgK)] for isochoric processes. It is indicated that the illumination may not be stationary, such in order to excite an acoustic wave. The confinements, furthermore, allow separating the temporal and spatial dependencies of the heating function into $H(\vec{r}, t) = A(\vec{r})I(t)$. By approximating the temporal part as a Dirac delta $I(t) = \delta(t)$, equation 2.18 is further simplified:

$$\left(\nabla^2 - \frac{1}{v_s^2} \frac{\partial^2}{\partial t^2} \right) p(\vec{r}, t) = -p_0(\vec{r}) \frac{\partial}{\partial t} \delta(t). \quad (2.19)$$

Therein, $p_0(\vec{r}) = v_s^2 \beta A(\vec{r})/C_p$ represents the initial photoacoustic pressure field, with the spatial electromagnetic absorption function A in [J/m³]. It is commonly also expressed as

$$p_0(\vec{r}) = \Gamma \eta_{th} \mu_a F, \quad (2.20)$$

where Γ is the dimensionless Grueneisen parameter, η_{th} is the heat conversion efficiency and F denotes the optical fluence [J/m²].

The general forward solution of equation 2.18, assuming thermal confinement, is commonly derived by applying the free-space Green's function [36], yielding

$$p(\vec{r}, t) = \frac{\beta}{4\pi C_p} \int d^3r' \frac{1}{|\vec{r} - \vec{r}'|} \left. \frac{\partial H(\vec{r}', t')}{\partial t'} \right|_{t' = |\vec{r} - \vec{r}'|/v_s}. \quad (2.21)$$

It describes the pressure distribution due to the photoacoustic wave, which expands radially with the material's speed of sound, as a function of time and place. Introducing again the above discussed separation of spatial and temporal dependence of the heating function, and evaluating the integrand on the sphere surface, the delta heating response results:

$$p_d(\vec{r}, t) = \frac{\partial}{\partial t} \left[\frac{1}{4\pi v_s^3 t} \int d^3r' p_0(\vec{r}') \delta \left(t - \frac{|\vec{r} - \vec{r}'|}{v_s} \right) \right]. \quad (2.22)$$

Evidently, this pressure $p_d(\vec{r}, t)$ is measurable by a point detector at $\vec{r} = \vec{r}_d$ during an optoacoustic experiment. For delta pulse excitation of a sphere, for example, the measured pressure curve takes a bipolar shape. Equation 2.22 means that the pressure distribution due to the photoacoustic wave at a time t and place \vec{r} is given by the time derivative (slope) of the integral of the initial pressure distribution evaluated along the shell of a sphere with radius $t \cdot v_s$.

Reconstructing the initial pressure distribution p_0 from the detected pressure p_d is the task of the inversion algorithms discussed in the next chapter. Before addressing the reconstruction though, the limitations of the theory with respect to practical applications are discussed in the following section.

2.4 Considerations for biological tissue

The deduction of the optoacoustic pressure distribution was done under the assumptions that the sample is homogeneous and isotropic, and thermal diffusion and stress relaxation take much longer than the illumination process (laser pulse). However, in some biological samples, these assumptions might not be valid. Their validity and limitations thereof are discussed in this section.

Internal reflections. Homogeneity is, for example, one of the major problems in whole body imaging of small animals like mice [43]. In the thorax region, the ultrasonic wave propagates through various kinds of heterogeneous tissue, like muscles, lungs, ribs, and skin. The wave is thereby reflected at each tissue interface, scattered at rough interfaces, and strongly damped in the air that is located in the lungs. While these reflections are the basic requirement for sonography, in optoacoustic imaging their occurrence is, together with scattering and damping, the main cause of artifacts. In order to obtain trustworthy images of the mouse thorax, a precise adaptation of the detection geometry is, therefore, necessary. One approach to cope with this challenge would be to limit the region of interest to a domain which can be scanned through a minimum amount of tissue interfaces. In analogy to the Fresnel equation 2.6 for light reflection at the interface between materials of different refractive indexes, the reflectivity R of sound is dependent on the acoustic impedances $Z = v_s \rho$ of the adjacent materials

$$R_{\perp,ac} = \left(\frac{Z_1 \cos \theta_1 - Z_2 \cos \theta_2}{Z_1 \cos \theta_1 + Z_2 \cos \theta_2} \right)^2 \quad (2.23)$$

The following examples demonstrate the relevance of distortions of the optoacoustic signal by reflections. At the interface of compact bone ($Z_b=6.1 \cdot 10^5 \text{g}/(\text{cm}^2\text{s})$) and muscle ($Z_m=1.6 \cdot 10^5 \text{g}/(\text{cm}^2\text{s})$) [39], more than one third of the sound intensity is reflected, assuming a perpendicular incidence. Less problematic for optoacoustic imaging, is the interface between fat ($Z_f=1.42 \cdot 10^5 \text{g}/(\text{cm}^2\text{s})$) and water ($Z_w=1.49 \cdot 10^5 \text{g}/(\text{cm}^2\text{s})$), where 99.9% of the sound intensity is transmitted.

Thermal confinement and stress confinement. It is now evaluated, if stress confinement and thermal confinement are really given in biological tissue. Thermal confinement is valid, if the light pulse is negligibly short compared to the thermal relaxation time τ_{th} , which is defined as:

$$\tau_{th} = \frac{d^2}{\alpha_{th}}. \quad (2.24)$$

A typical value for thermal diffusivity in biological tissue is $\alpha_{th}=1.3 \cdot 10^{-3} \text{cm}^2/\text{s}$. For a structure of interest as small as $d=30$ microns, τ_{th} is 6.92ms, hence, more than five orders of magnitude longer than a 10ns laser pulse used in this work.

The stress confinement condition turns out to be more peculiar to fulfill. The stress

relaxation time τ_s is the time that it takes for a sound wave, such as the optoacoustic ultrasonic wave, to propagate the distance of interest d :

$$\tau_s = \frac{d}{v_s} = \frac{30\mu m}{1.5mm/\mu s} = 20ns. \quad (2.25)$$

Thus, the stress relaxation time is only twice as long as the mentioned 10ns pulse. To overcome such resolution-limitation, a laser that provides shorter pulses needs to be applied.

Initial pressure distribution within the specimen. As described in equation 2.20, the initial pressure field is directly proportional to the field of the absorption coefficient μ_a , and the field of the optical fluence F . This is particularly relevant for designing an optoacoustic scan arrangement for scanning tumors. Again, we consider a subcutaneous tumor: starting at the periphery, the light passes through the mainly scattering epidermis and dermis, as well as the densely vascularized (absorbing) subcutis, before it penetrates into the tumor tissue having lower absorption than the subcutis. In an optoacoustic experiment, the strong signals from the highly absorbing subcutaneous vasculature may distort the images of the tumor vasculature. For example, if the subcutaneous tumor is assumed as a free-standing half sphere oriented with the top towards positive z in cylindrical coordinates, and the laser pulse propagates along the z -axis towards negative z (i.e. tumor is illuminated from the top, see also chapter 5), strong out-of-plane signals from the top may overweigh in-plane signals at lower levels. The strength of this effect is, however, priorly unknown. It strongly depends on the specimen and the laser beam profile, and will be investigated experimentally. The effect needs to be taken into account for the development of the setup, too.

Chapter 3

Scanning and tomography methods

Optoacoustic imaging can be performed in a variety of ways, but the imaging arrangement needs to be adapted to the sample of interest, in order to obtain meaningful, artifact-free images. The key experimental processes for obtaining an optoacoustic image are scanning a detector to sample the propagating pressure wave at various positions, and reconstructing the initial pressure distribution, thus, the distribution of absorbed light fluence. One possible approach is to scan the formerly mentioned point detector, for which the time-resolved optoacoustic pressure curve has been derived analytically. As the point detector's sensitivity field is, however, not restricted, this approach requires three-dimensional reconstructions and generally large numbers of projections. Transducers more commonly used in optoacoustics are, therefore, focused. Other than point detectors or flat detectors, focused detectors have a typically cylindrically or spherically curved transducer surface, which means that their sensitivity is respectively constricted to a line- or a point-shaped focal zone. Hence, the fewer degrees of freedom allow for reducing the complexity of the inversion algorithms.

As described in **section 3.1**, the setup developed in this work allows scanning the detector or detectors along the Cartesian coordinates x , y , z , and along the azimuth ϕ in polar coordinates, thus, three-dimensionally in different geometries. Of interest for biomedical imaging are especially the raster scanning geometry and the tomographic geometry. The illumination is adapted according to the sensitivity field of the transducer, with the purpose to reduce the amount of light that is deposited out of the focus of the detector. In **section 3.2**, the reconstruction of the initial absorption distribution is discussed, addressing the applied in-

version algorithms, and adaptations thereof to specific experimental configurations. In case of tomography, the backprojection algorithm [44] and model-based inversion algorithm [45] were mainly used in this work, providing the basis for final visualization of the sample by three-dimensional rendering as well as maximum intensity projections. When the absorption distribution is recorded for several illumination wavelengths, the distribution of the constituting absorbers with differing absorption spectra can be decomposed multi-spectrally, which is described in **section 3.3**. The methods for spectral decomposition applied in this work were linear decomposition and independent component analysis (ICA) [46]. Concluding this chapter, **section 3.4** discusses empiric adaptations of the reconstruction methods that were useful for the performed optoacoustic image reconstructions.

3.1 Scanning methods

3.1.1 General considerations on detectors.

The transducer parameters that define the properties of optoacoustic images are the focal length F , the element diameter D , and the detectable frequency (band) f . The size of the focal zone of the ultrasonic detector is limited by diffraction effects, thus, the focus is not ideally tight, but of finite dimensions. Characteristic parameters are the width and the length of the focal zone, defined by the decrease by 6dB with respect to the maximal sensitivity. In first approximation, the value for the respective beam diameter BD is given by [47]:

$$BD = \frac{1.02Fv_s}{fD}, \quad (3.1)$$

and that of the beam length BL is given by

$$BL = N \cdot S_F^2 \cdot \frac{2}{(1 + 0.5S_F)}. \quad (3.2)$$

Herein, v_s represents the speed of sound in the coupling / transmission medium. $N = D^2 f / 4c$ is the near field length, and $S_F = F/N$ is the normalized focal length. Although near field interferences as well as the exact shape of the transducer element geometry are not taken into account in those equations, the estimations are sufficiently accurate for determining key parameters of the imaging performance, such as elevational resolutions for tomographic imaging or

lateral resolutions for raster scan imaging (cf. section 3.1.3). From these values, the sensitivity field in proximity of the focus and in the far field of the transducer, thus, farther away than the near field distance N

$$N = \frac{D^2 f}{4v_s}, \quad (3.3)$$

is evaluated in Gaussian approximation [38].

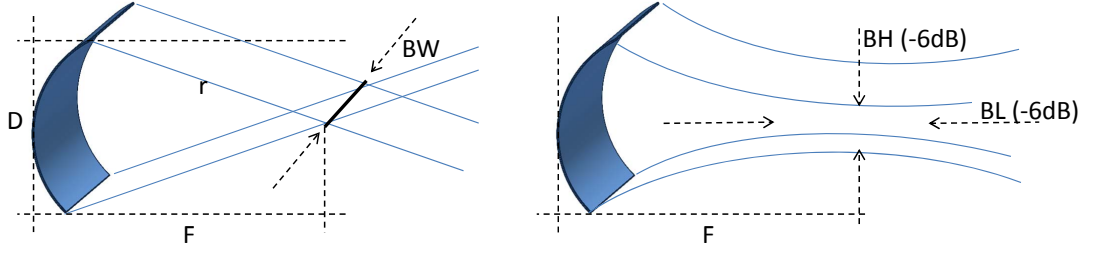


Figure 3.1: Sensitivity field for the example of a cylindrically focused transducer.

3.1.2 Tomography with a line-focused transducer

During a tomographic scan, the transducer is rotated around the specimen at a fixed radius, typically (but not necessarily) over an angle of $\phi_{max} - \phi_{min} = 360$ degrees. By rotation of the respective line-shaped focal zone, the imaging plane is defined. Its finite thickness, the elevational resolution, is, therefore, defined by the beam width of the transducer. Tight focusing for the transducer, thus, allows reducing the thickness of the imaged region, and building a stack of images at different elevations z , to provide a three-dimensional visualization of the specimen. The radius of the imaginary cylinder shell, along which the transducer is moved, does not have to equal the focal length of the transducer - to the contrary: For certain samples and reconstruction algorithms, the thickness of the image plane is reduced, if the transducer is positioned farther away from the center than its focal length (cf. section 3.4).

The unique advantage of tomography is the solely by the transducer's frequency band limited in-plane resolution. If the resolution criterion is that two point absorbers are still resolved as long as their centers are separated by the full width half maximum of their hull curves, the resolution R_i is given by [37]

$$R_i = 0.8 \frac{v_s}{f_{max}}, \quad (3.4)$$

wherein f_{max} represents the highest frequency detected during the imaging experiment.

Besides the angles ϕ and elevations z , over which the detector is scanned in cylindrical coordinates, the tomographic scanning process is defined by the amount of signal curves acquired and averaged N_{av} at each position, and the motion mode of the scanning procedure, i.e., if the scan is performed step-wise or continuously. In stepwise scanning, the transducer is moved to the initial angle ϕ_{min} and held in place to acquire N_{av} sound wave signals, before it is moved to the next angle, and so on, until it reaches the final angle ϕ_{max} . By averaging, the immediate signal-to-noise ratio of the signal curve before the inversion is increased. Continuous acquisition on the other hand, does not average at every angle, but during the reconstruction process. In this case, the amount of desired projections N_p , as well as the initial and final angles are specified, and the scan is performed at the calculated angular velocity:

$$\dot{\phi} = \frac{\phi_{max} - \phi_{min}}{N_p} \cdot f_L. \quad (3.5)$$

Therein f_L represents the repetition rate of the light source.

3.1.3 Raster scanning with a point-focused transducer

Different from line focused transducers, the beam width of point-focuses transducers equals their beam height, so the sensitivity field is approximated as a two-dimensional Gaussian profile. Line (raster) scans are performed exclusively along the axes of the Cartesian coordinate system. To reduce the duration of a scan by avoiding the stop-and-go of the driving stages, single lines are optionally scanned in continuous acquisition mode as long as the laser pulse energy fluctuations are negligible, and the signal exceeds the noise level significantly.

The scans are performed orthogonally, which means that the transducer never turns by an angle different from 90 degrees. In correspondence with the nomenclature for sonography, the scans are categorized into, A-, B-, and C-scans. In A-scans, herein described for reasons of completeness, the transducer is not moved mechanically, but only the time-dependent pressure curve at a defined transducer position and orientation is acquired. B-scans are performed by scanning the transducer along a straight line, typically the x -axis, allowing to reconstruct a sectional view of the sample. Truly (x and y) raster scanning the transducer over the sample allows reconstructing C-scan images (cf. section 3.2.2). Ideally, the plane of interest is, therefore, positioned in the focus of the transducer. A typical experimental scan runs along the x

coordinate from x_{min} to x_{max} , then moving to the second position of y to perform the same x-scan from x_{min} to x_{max} again. When the position y_{max} is reached, the same x- and y-scans can be repeated for another z -position, if relevant.

3.2 Methods for reconstructing the initial pressure distribution

3.2.1 Cylindrical reconstruction methods

Back-projection

The universal back-projection (backprojection) algorithm [44] is derived analytically from the photoacoustic wave equation 2.19 for an infinite acoustically homogeneous medium, yielding the initial pressure distribution as

$$p_0(\vec{r}) = \int_{\Omega_0} b(\vec{r}_0, \bar{t} = |\vec{r} - \vec{r}_0|/v_s) \frac{d\Omega_0}{\Omega_0}. \quad (3.6)$$

Therein $b(\vec{r}_0, \bar{t})$ is called the backprojection term

$$b(\vec{r}_0, \bar{t}) = 2p(\vec{r}_0, \bar{t}) - 2\bar{t} \frac{\partial p(\vec{r}_0, \bar{t})}{\partial \bar{t}}. \quad (3.7)$$

and $d\Omega_0$ is the solid angle, covered by the transducer surface. The essential instruction for reconstruction by this backprojection equation is, thus, to project the values of the measured, time-dependent pressure curve $p_m(t)$ onto spheres with radii $r = v_s t$. The detector, hence, needs to be scanned over $4\pi sr$ around the sample in case of a spherical scanning geometry. The inversion is comparable to a spherical radon transformation.

In practical use, the integral is often evaluated for each of the two terms separately, wherein the first term is referred to as direct backprojection, or classical sum-and-delay, and the second term is referred to as derivative backprojection. The derivative acts similarly to a high-pass filter on the images. The applicability of the reconstruction method, as well as eventually necessary adaptations, are assessed in section 4.4.1 of the next chapter.

In two dimensions, sum-and-delay reconstruction can be illustrated as shown in Fig.

3.2. The method contains features of classical triangulation.¹ The measurement starts when

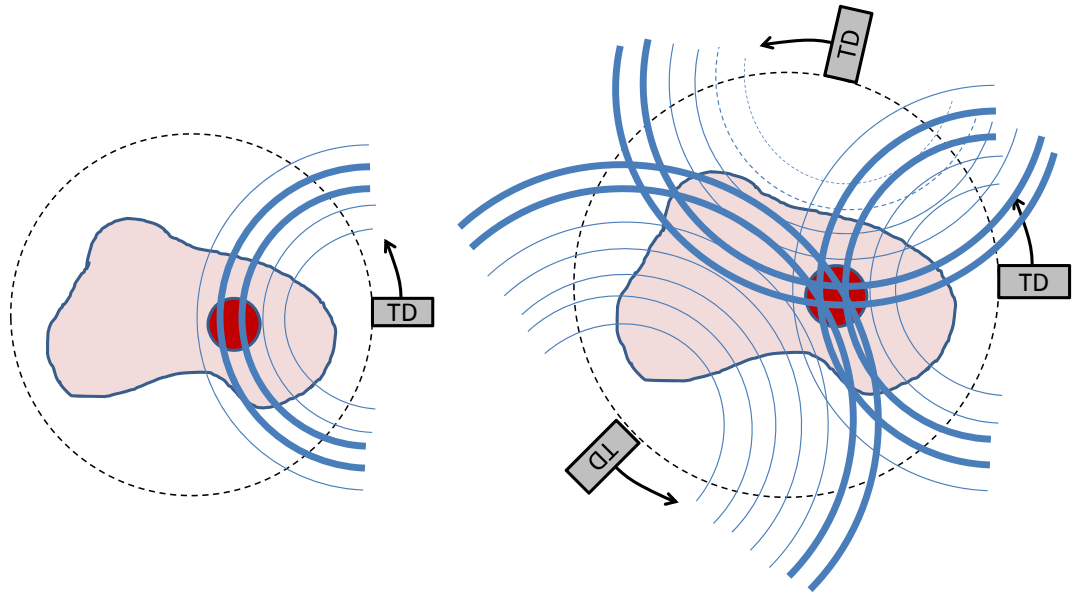


Figure 3.2: Principle of the sum-and-delay algorithm. Left: Shown is the first projection. Right: shown are three projections, including the first projection, illustrating the reconstruction process. The exemplary sample consists of a weak background absorber with a highly absorbing round region inside of its boundaries. The absorbers are optically inhomogeneous. The line widths of the circles represent the signal amplitudes projected along them.

the detector is positioned at ϕ_{min} . The signal curve $U(t)$ is projected along concentric circles with radii $r = t \cdot v_s$. The transducer is then rotated to the second projection angle, the respective second curve is projected and added to the first, and so on, until the transducer arrives at the final position ϕ_{max} . The value projected along a circle with radius $r = (t_0 + i\Delta t) \cdot v_s$ that intersects the highly absorbing insertion exceeds the others. As the projections are summed up, the resulting pixel intensity is finally high in the area of high absorption. Hereby, it is shown how important it is to maintain the light fluence distribution constant throughout the entire scan. If it is not constant, distinct projections are emphasized, causing streak artifacts within the image [48]. The same applies for insufficient amounts of projections. Methods to correct for sub-optimal partial illumination and non-uniform acoustic detection fields have been successfully applied for imaging tissue mimicking agar phantoms, but not yet for imaging samples having a complex structure, such as tumors. It is, thus, a goal to optimize the illumination by means of the setup design.

¹The illustrated method of modeling the backprojection algorithm by triangulation is mathematically not accurate, because the optoacoustic signals are in fact bipolar, so that the thick circles in Fig. 3.2 should be radially bipolar, too. However, the tomographic backprojection reconstruction compensates for this effect, if an ideal detector that can detect all frequencies of the optoacoustic pressure wave is considered. As an auxiliary model, the signal acquired at each projection may be integrated over time before the backprojection, to provide a signal curve with only positive amplitude.

Model-based inversion

Model-based reconstruction is an algebraic method based on numerical solutions of equation 2.21. The approach applied in this work uses a linear interpolation of the heating function, in order to give the discretized matrix relation for each projection k [45]:

$$p^k = M^k z. \quad (3.8)$$

This equation relates the pressure curve p^k at projection k to the initial pressure distribution (optoacoustic image) on the image grid $z_j = H(r_j)$ via the model matrix M . The k single matrix equations are grouped into a large matrix by stacking the vectors and matrices. By inverting equation 3.8, the image can be calculated directly after inverting the model matrix M . One possible method for inverting the model matrix is provided by the Moore-Penrose pseudoinverse, which needs to be evaluated once for a given experimental arrangement: [49]:

$$z = M^+ p. \quad (3.9)$$

Although the model-based inversion has shown more quantitative optoacoustic tomography results than inversion by backprojection (cf. [49]), its applicability to high resolution optoacoustic imaging is limited due to high demand on computing capacity, especially in comparison with backprojection. For a typical tomographically defined resolution of 30 μm , and a 10mm x 10mm region of interest, the grid of the image needs to contain at least $10000 \cdot 1.4/30 = 467$ pixels, in order to avoid a loss of information. For a typical value of 400 projections per slice, the model matrix would have the dimension $467 \times 467 \times 400$, so that it would not be computable with standard personal computers. In addition to that, certain reconstruction parameters are a-priori unknown, and they need to be determined during the reconstruction process. Therefore, the model matrix would have to be calculated multiple times, which would in turn further increase the duration of the experiment. To avoid this, exact the same configuration would have to be used for all experiments, as done in setups that use transducer arrays [50].

3.2.2 Cartesian reconstruction methods

In the present work, only point-focused transducers are used for raster scanning. The constricted sensitivity field of such transducers allows for simpler inversion methods, because the source of the optoacoustic signal is essentially pre-localized by the hardware.

In A-Scans, only the time-dependent pressure signal due to the incoming pressure wave is recorded, hence, only a longitudinal profile is visualized. For certain experiments, though, like measuring the thickness of a tissue sample, this information is sufficient. Multiple A-scans aligned along a line span up a two-dimensional B-scan image, in which the image's x and y axes are the mechanically scanned direction and the time (of flight) axis, and the pixel intensity is given by the signal amplitude. By adding a second scan direction, a C-scan, the two-dimensional projection of the maximal signal amplitude (MAP), is acquired. If three-dimensional samples are of interest, the C-scan is preformed for a number of depths, to build an image stack. Depending on the sample of interest, the signal may also be cut to the focal zone, to increase the x - y -resolution.

Another approach for three-dimensional raster scan optoacoustic imaging is based on the extension of the depth of focus by the synthetic aperture focusing technique (SAFT) / virtual detector technique. For the reconstruction, not only the signal detected at a specific position is projected along a line, but also the signals detected at the neighboring detector positions are taken into account. The finally projected signal consists of a coherence-weighted and delayed sum of all considered signals [51] [52] [53]. This reconstruction method has been proposed and demonstrated for optoacoustic microscopy, requiring particularly constant light fluence throughout the sample, which can be achieved by a dark-field illumination approach [21]. Such techniques have shown to be applicable for longitudinally extending the depth of focus, but the lateral resolution in the focal plane (i.e., highest lateral resolution) is not affected thereby. However, the techniques were mainly applied to samples with a de facto plane surface. If the geometry of the sample surface is curved or heterogeneous, as it is the case for subcutaneous tumors, the parameters for coherence weighting cannot be estimated analytically. In this case, the corrections may even cause additional corruption of the images, as proof-of-principle investigations that were done within the framework of the work presented herein showed, but shall not be further presented in this thesis.

3.3 Multi-spectral decomposition of absorbers' spatial distributions

3.3.1 Linear decomposition

A well established method for spectral unmixing of the absorbers' spatial distributions is linear decomposition. Since it is performed pixel by pixel, it is not particularly disturbed by artifacts in the single wavelength images. Linear decomposition is based on the concept of molar absorptivity: the absorption coefficient μ_a of a material is given by the sum of the concentration-weighted molar extinction coefficients ϵ [1/(M cm)] of the constituting absorbers k :

$$\mu_a = \sum_{k=1}^n c_k \cdot \epsilon_k. \quad (3.10)$$

As described in equation 2.20, the intensity of a pixel $I = p_0$ in the optoacoustic image is proportional to the deposited fluence and the absorption coefficient. Assuming that the Grueneisen parameter and the heat conversion efficiency are constant, the reconstructed single wavelength images need to be corrected for wavelength-dependency of laser pulse energies and absorption along the water path, before the linear decomposition. The spatial concentration distribution c of the absorber k is then evaluated according to the matrix equation

$$I(\lambda) = \epsilon(\lambda, k)c_k \longrightarrow c_k = \epsilon(\lambda, k)^{-1}I(\lambda). \quad (3.11)$$

3.3.2 Independent component analysis (ICA)

Independent component analysis is an algebraic method employing statistics for determining the distribution of absorbers in optoacoustic images. It has only played a marginal role for this work, so that the reader is referred to the literature (e.g. [46]) for a detailed description. In short, the method analyses images acquired at the same location but various wavelengths, however, other than linear decomposition, it does not require a-priori knowledge of absorption spectra. Yet, recent developments have shown that feeding ICA with a-priori known absorption spectra as an initial guess potentially improves the accuracy of the method when used for optoacoustic imaging. Such approach is referred to as *guided* ICA in the following. The images of the components are identified by comparison of initially known absorption spectra with resulting absorption spectra.

3.4 Empiric adaptations of the backprojection algorithm and image corrections

Recent work by Dean Ben et al. has shown how scattering of optoacoustic signal in heterogeneous media influences images, and how to correct for this effect [54]. A simplified correction method based on these findings was applied to the reconstructions of the optoacoustic images presented in this work. The optoacoustic signal arising from a tumor (represented by a sphere) typically extends from time point t_0 to t_1 , wherein the $t_1 - t_0$ corresponds to the runtime difference of the wave propagating at speed of sound. Strong high-pass filtering limits the elevation of the field of view, as described in section 4.3.1. The method, therefore, firstly filters the signal to about $150\mu\text{m}$ in elevation. Subsequently it determines t_0 and t_1 by the time points at which the (eventually averaged) signal curve exceeds the noise threshold, wherein the noise threshold is set to the maximum noise amplitude of the signal curve outside of the interval t_0 to t_1 . The center of the signal package is determined as the average of t_0 and t_1 , and the signal curve is cut at that center (rest of curve set to zero). In consequence, under consideration of the sensitivity field of the transducer, positioning of the focal zone of the transducer slightly off center of rotation may be used as a means of further increasing the elevational resolution.

The above described effect of restricting the imaging plane in elevation by high-pass filtering may equally be used for masking the tumor. Thereby, a binary signal-like curve is defined, in which all values between t_0 and t_1 are set to 1, whereas all other values are 0, and same backprojection reconstruction is performed in parallel. All non-zero values of the resulting image are subsequently set to 1, resulting in a true in-plane hardware mask, which may restrict the optoacoustic image of the tumor to within in-plane boundaries without necessity of high-pass filtering the true optoacoustic signal and respective negative side effects of signal information losses.

To correct the reconstructed optoacoustic images for depth-dependent and wavelength-dependent variations in light fluence, the images were multiplied with wavelength-dependent linear factors and with two-dimensional Bessel functions of the first kind, according to [42].

Chapter 4

Experimental arrangement and characterization

In order to investigate the microstructure of subcutaneous mouse tumors, an optoacoustic setup was designed that exceeded the current boundaries of mesoscopic imaging. In particular, structures within the tumor smaller than 40 micrometers needed to be resolved depth-independently, i.e., independently of the depth below the top of the tumor and the surface of the tumor. Imaging up to 1 centimeter deep into highly scattering tissue, such as tumor tissue, was enabled. Although the setup was developed specifically for mouse tumor imaging, its field of applications was much wider, allowing to perform other biological investigations as well. The system was designed in a modular way, which provided high flexibility on illumination wavelength and geometry, detection wavelength and geometry, as well as on the scanning geometry. Some examples for further applications are described in chapter 7. In general, the scanner part of the system was developed for scanning in the geometries indicated in Fig. 4.1, categorized into six groups according to the combination of illumination and scanning geometry.

In this work, the arrangements written in green in Fig. 4.1 have been applied for biological experimentation, the ones written in yellow have been tested for their applicability in proof-of-principle experiments, and those written in red have been developed, but no experiments were performed beyond characterization. The system consisted of a basis part called the **open microscanning system**, which was the same for all experiments, and which was combined with various active scanner modules that were integrated into the basis system.

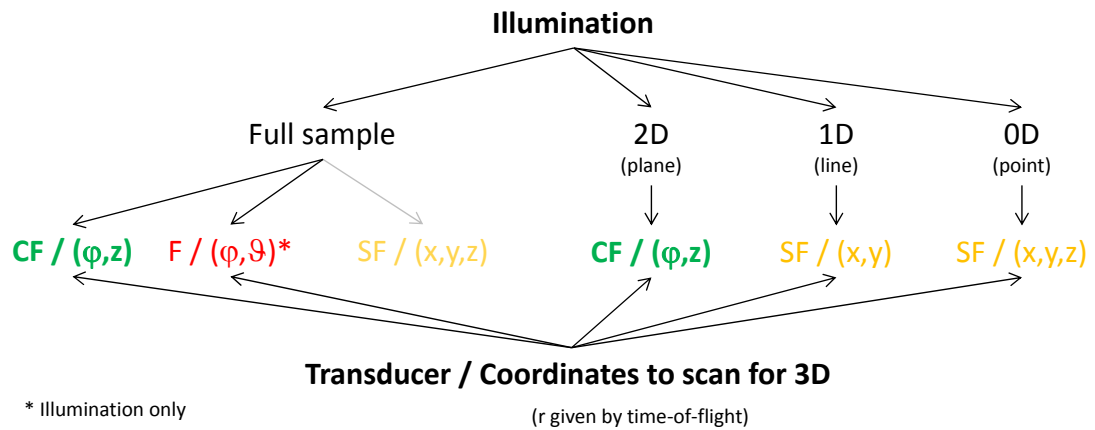


Figure 4.1: Scheme of the developed scanning geometries indicating advantageous combinations of illumination and detection. F: flat/unfocused, CF: cylindrically focused (line-focused), SF: spherically focused (point-focused)

After discussing the general requirements on the optoacoustic system in **section 4.1**, the components of the basis hardware as well as significant developmental processes are described in **section 4.2**. The different system configurations based on the scanner modules are accurately characterized in **section 4.3**. To assess the applicability of each scanner module for mouse tumor imaging and other biomedical imaging, I performed the phantom experiments described in **section 4.4**. Finally in **section 4.5**, a discussion on which scan arrangement is best-suited for the subsequent biomedical investigations, and why, concludes this chapter.

4.1 General considerations for development of the optoacoustic system

The optoacoustic system was shaped around the biological samples of interest, i.e., subcutaneous tumors on the backs of mice. Imaging shall ideally be performed *in vivo*. As the tumors are to be submerged in liquid for optimal transmission of the ultrasonic wave from the sample to the detector, and the mouse may not breathe that liquid, the head of the mouse is to be kept in air (or at least under a snout mask). Essentially, the mouse was positioned in the setup in two different ways: Either the head of the mouse was kept above the liquid level with the tumor hanging into the liquid, or the mouse was fixed in a box that was submerged in the liquid with the tumor (optionally elevated) in transient contact with the liquid through a thin membrane. On the other hand, limitations due to *in vivo* handling of the animal needed to be taken into account. Furthermore, the light distribution on the sample surface needed to be controlled and

adapted to the detection geometry / transducer sensitivity field in order to reduce the amount of artifacts, as, for example, arising from out-of-plane signals, and not exceed tissue damage thresholds in aqueous medium.

With regard to the detection mechanism, the Nyquist theorem is taken into account to avoid aliasing. Therefore, a data acquisition system having a sampling rate of at least twice as high as the maximum detected acoustic frequency generated by the imaging target was selected. The detection bandwidth and sensitivity field of the transducers needs to be high enough for achieving image resolutions in the 30 μ m range. Furthermore, in order to allow for precise reconstruction, experimental conditions needed to be kept constant. I.a., this required a constant water temperature of around 36°C, provided by constant flow of liquid between two tanks, as will be further described in the following sections.

4.2 The open microscanning system

4.2.1 The hardware design

The developed optoacoustic system is shown in Fig. 4.2. It is composed of a high pulse energy laser (L), optics arrangement for illumination control (O), a sufficiently large experiment basin (B) connected to a heated water reservoir (R), a scanner unit (S) for displacement of the detection components, and a PC-based data acquisition system. To provide a high level of flexibility for the illumination design, and ensure safe operation with respect to laser hazards, the optical part of the system is mounted on an optical table. Constant experimental conditions for *in vivo* experiments are maintained by circulating the water in the 60x60x15cm³ experimental basin through the water reservoir that has a capacity of 70l and is equipped with 300W aquarium heating (Jaeger, Eheim, Deizisau, Germany). Circulation (cf. Fig. 4.2b) is driven by a 65W centrifugal pump (1260, Eheim, Deizisau, Germany). Furthermore, for the *in vivo* experiments, a small animal Isoflurane anesthesia unit was developed.

The water circulation is sufficiently slow, so that the hydrodynamic force exerted upon the sample is negligible. By the flow direction indicated in Fig. 4.2b, temperature gradients, potentially distorting the propagation of the pressure wave, are reduced in proximity of the sample. The sample, optical components, or any other instruments are fixed on the custom-

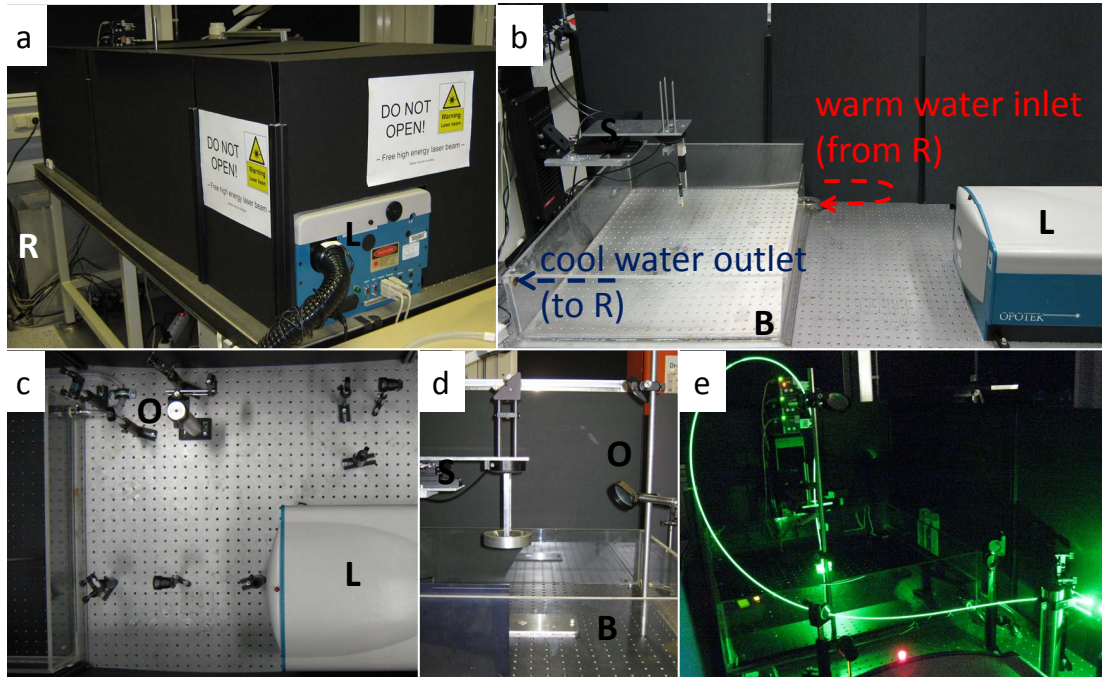


Figure 4.2: The open microscanning setup. Illustrated is the arrangement of the high pulse energy laser (L), exemplary optics arrangement for illumination control (O), the experiment basin (B), the heated water reservoir (R), and the scanner unit (S). a: Enclosed configuration - no laser light can escape out of the setup, allowing unconventional laser beam paths, b: side view on the system, c: top view on one possible configuration of optics arrangement wherein the SHG 532nm light is directed to a fiber coupler (see green arrow), d: optics arrangement in the basin with scanner configured as free-beam ring illuminator (see section 4.3.2), e: exemplary implementation as single fiber coaxial microscanning device (see section 4.3.3).

made M6 threaded aluminum ground plate with 25mm distance between the holes. To absorb eventually disturbing laser light reflections, the ground plate is painted black.

The scanner unit consists of three translation stages that are arranged perpendicularly to each other, to scan in Cartesian coordinates, upon which one rotation stage is mounted, as illustrated in Fig. 4.3. The rotation stage PRM1-Z7 (Thorlabs, Dachau, Germany) can rotate more than 360 degrees at a maximum angular velocity of $14^\circ/\text{s}$. Hence, the minimum tomographic scan time per slice is 26s. Within this period of time, a laser with pulse repetition rate of 20Hz (see section 4.2.2) emits 520 pulses. Therefore, at least 520 projections were acquired in any tomographic scan. The stage is constructed with a 25mm hole along its rotation axis, which is used for interruption-free illumination or sample fixation for full rotation scans. To displace the transducer along Cartesian coordinates for alignment or scanning, the stages NRT100/M (100mm travel, z-axis, elevation) and two MTS50-Z8 (50mm travel, x- and y-axis) (all Thorlabs, Dachau, Germany) are used.

The transducers are connected to an active amplifier (AU1332, Miteq, Hauppauge, NY,

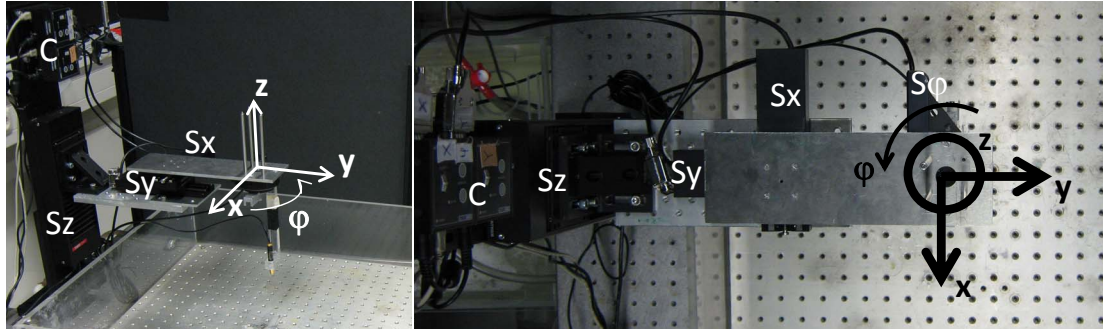


Figure 4.3: The scanner device comprising stages (S) for linear (x,y,z) and rotational (ϕ) displacement of the ultrasonic transducer and respective controllers (C). The scan coordinate system is Euclidian (right-handed) with the z -vector oriented upwards, i.e., pointing antiparallel to the gravity vector. Left: side view. Right: top view.

USA) with gain larger than 54dB. After amplification, the signal is digitized by the dual channel Gage Octopus (Compuscope 8327, Gage, Lockport, IL, USA) with 14bit vertical resolution. The range is set manually before the acquisition to adapt to the signal strength. For data recording and hardware control, a Labview virtual instrument was designed, with implemented live reconstruction based on backprojection algorithm. Based on the dual channel acquisition capability of the acquisition card, two images are reconstructed simultaneously. Except of the truly detected signal, the water temperature measured by the detector USB-Temp (Cleware, Hollingstedt, Germany) as well as manually determined or defined parameters such as light wavelength, scan ranges, scan type (continuous or stepwise), and distance from the transducer to the center of rotation are recorded. The (wavelength-dependent) pulse energy is saved and used for accurate normalization before multispectral decomposition.

For *in vivo* experimentation, the animals are anesthetized. Mice are usually sedated by injection of a low dose of a Ketamine-Xylazine-Mix, or through inhalation narcosis, where inhalation narcosis allows the better control of physiological parameters such as breathing. The developed Isoflurane inhalation narcosis unit is illustrated in Fig. 4.4. Therein, purified oxygen gas is enriched with Isoflurane by means of the evaporator Vapor 2000 (Draeger Medical, Luebeck, Germany). Before the evaporator, the gas flow is adjusted by a ball valve. After the evaporator, the narcosis gas is distributed to the hoses connected to snout mask or narcosis boxes through bore holes in the aluminum plate, it is built on. This design prevents from gas leakage. Before final distribution, further valves are built in, so that distribution of the gas to the distinct consumers is controlled independently.

To ensure continuous flow of the narcosis gas without emission into the free air, the gas

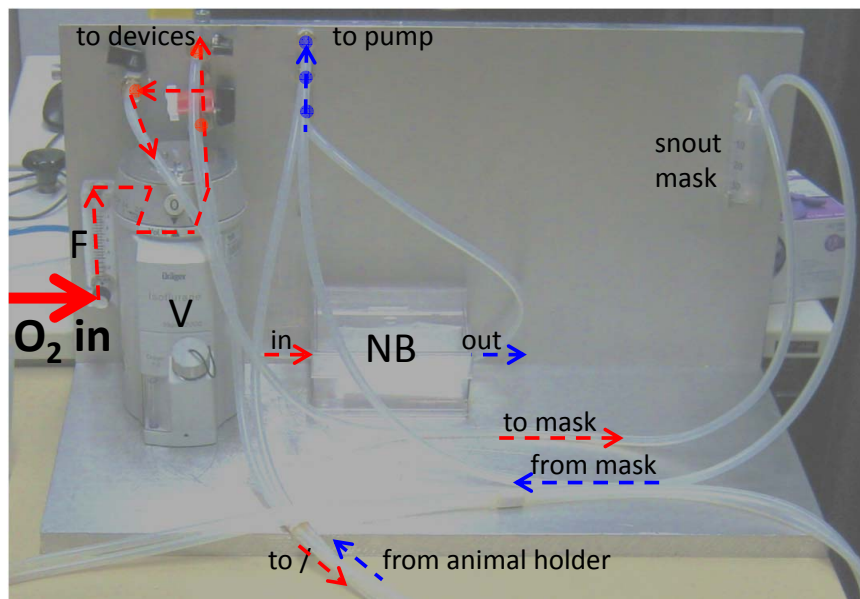


Figure 4.4: The developed inhalation narcosis device. Gas distribution occurs within the thick back plate. F: flow-meter with valve, V: Isoflurane vaporizer, NB: narcosis box. Red lines indicate the path of the inhalation narcosis gas (Oxygen-Isoflurane-Mix), blue lines indicate path of exhaled air that is led to an active coal filter for absorption.

is aspirated by a vacuum pump and dumped in an exhaust active coal filter.

4.2.2 The illumination

The heart piece of the system is the class IV laser Vibrant 532I (Opotek, Carlsbad, CA, USA), illustrated in Fig. 4.5, which uses a flash lamp excited Nd:YAG laser (Brilliant, Quantel, Les Ulis, France) as source. The pump Nd:YAG laser's pulse length, wavelength, pulse energy, and beam diameter are 8ns, 1064nm, 300mJ, and 6mm respectively. The beam shape is Gaussian. Along the beam path, the laser is, upon emission, first linearly polarized parallelly to the table by means of a $\lambda/4$ -plate, after which it passes through a nonlinear crystal for second harmonics generation (SHG). The photon energy is thereby doubled, thus, the wavelength after the SHG is 532nm. To free the laser beam from parasitic transmitted 1064nm light potentially causing harmful interference effects and spectral broadening, the beam is subsequently reflected four times by HR532/HT1064 mirrors typically reducing the 1064nm intensity by a factor of 100 at each reflection. The second harmonics generation is necessary for ultimately being able to tune the laser in the NIR range by means of optical parametric oscillation. An optical parametric oscillator (OPO) technically resembles a simplified laser without the active medium. Instead of stimulated emission, the 532nm beam is coupled into the resonator by an input coupling

mirror. Furthermore, a non-linear Beta-Bariumborat (BBO) crystal, having two optical axes of different refractive indexes, is located within the resonator. By tilting the BBO crystal, the phase matching is changed, and the emission wavelength is tuned. The ultimate effect of the OPO is a wavelength splitting according to energy conservation $1/532nm = 1/\lambda_s + 1/\lambda_i$ where λ_s refers to the signal wavelength, in this case tunable in the range 690nm-950nm, and λ_i is the idler wavelength, tunable to 1200nm-2450nm. The work presented herein uses the signal beam only. Some disadvantages of the idler are the significantly lower pulse energies (approximately 1/3 of the signal) and the high absorption in the sample surrounding water at the respective spectral range. The larger wavelengths of the idler, however, have the advantage of higher maximum permissible exposure (MPE) of tissue to laser radiation. High conversion efficiency of the OPO is ensured by high irradiations, which in turn are achieved by having created a slightly converging beam by the pump laser. The final emission beam of the OPO is of high order mode with low laser beam quality factor M^2 , thus, inhomogeneous and intrinsically diverging. Before emission to free space, its strong divergence is corrected by a convex lens to result in about 1 degree divergence.

In the system development process, the performance of the Vibrant was significantly improved, making it applicable for the optoacoustic experiments presented in this work. Before the development, it provided a maximum of 25mJ for less than one hour, after which the power dropped continuously to below 10mJ. I.a., this was an effect of non-constant pump beam profile. For example, large laser power fluctuations as effect of the low power needed to be compensated by large amounts of averages, hindering effective *in vivo* imaging sessions.

At first, the stability of the pump beam was improved. Therefore, several optical components were replaced to provide a constant beam-profile and stable pulse energies with less than 0.5% laser power fluctuations (standard deviation). The pump beam profile for near field as well as far field is shown in Fig. 4.5.¹ Secondly, the Vibrant laser system was disassembled for checking and replacing damaged optics. After reassembling the Vibrant, the OPO was upgraded to contain a longer BBO crystal to increase the conversion efficiency. Supplementary optics and mechanics were added to the Vibrant laser system for (instantaneous) extraction of the direct SHG 532nm pump beam and the formerly dumped 532nm beam retro-reflected from the OPO. For reproducible extraction of the direct 532nm pump, the Vibrant laser system was equipped with a high-precision motorized flipping mirror module (angular repeatability:

¹System revision in collaboration with manufacturer.

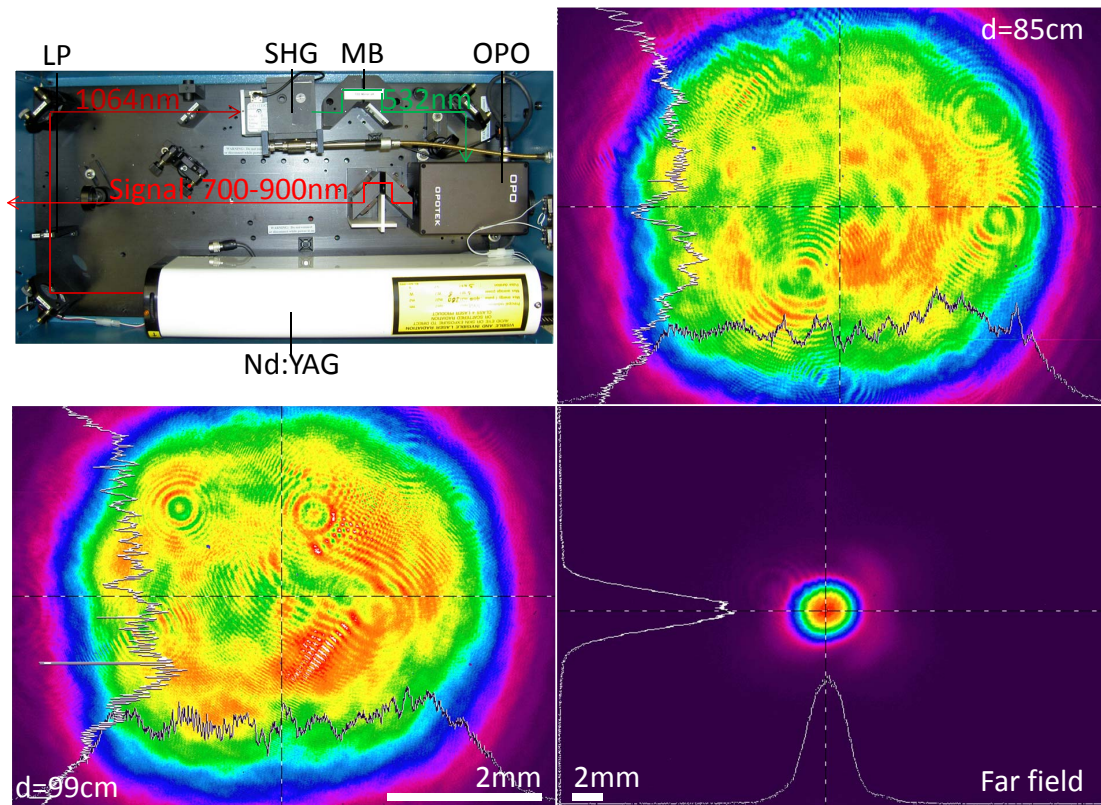


Figure 4.5: Upper left: The Opotek Vibrant 532I laser system. The major optical components of the Vibrant are the Nd-YAG laser, the lambda/4 plate (LP), the second harmonics generator (SHG), the mirror block (MB), and the optical parametric oscillator (OPO). Right and lower left: The beam profile of the Nd:YAG laser at various distances from the aperture (near field). Lower right: The beam profile of the Nd:YAG laser in the far field. The beam profile does not contain excessive intensities (cold / hot spots).

50 μ rad, MFF001/M, Thorlabs, Dachau, Germany). The direct 532nm pump beam was well collimated to a diameter of 6mm, providing a maximum pulse energy of 95mJ. Other than the retro-reflected beam, which provided up to 45mJ, the direct 532nm pump beam could not be emitted simultaneously with the NIR OPO beam. Simultaneous emission though would be of advantage for simultaneous multi-wavelength imaging in order to reveal various absorbers of different absorbing spectra at once. After all laser developments, the final pulse energy output curve (Fig. 4.6) was determined with the energy meter FieldMaxII-TOP and sensor head J-50MB-YAG (Coherent, Dieburg, Germany). The emission curve was measured after one hour, when the laser achieved steady state conditions, thus, not significantly changing for several hours.

For synchronization of the light pulse (hence, pressure wave), the Q-switch of the laser was coupled to a rectangle function trigger signal, which was transmitted to the acquisition card by a coaxial cable.

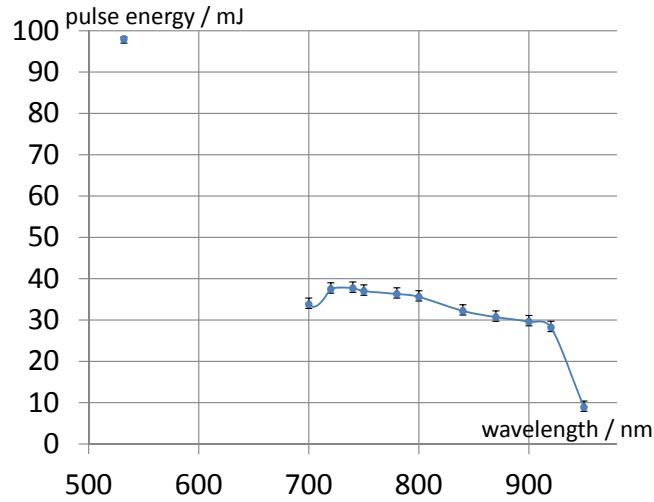


Figure 4.6: The wavelength dependent output energy (per pulse) of the OPOTEK Vibrant 532I laser system (error bars representing statistical fluctuations of laser).

4.3 System configurations and their characteristics

The main components of each optoacoustic scan design are the optics for pre-defined illumination of the sample, and the transducer for pre-defined detection of the emitted pressure wave. Those can be arranged in a variety of ways, of which I present particularly advantageous approaches in the following. Most of them are based on backward detection, i.e., the propagation direction of the light beam is opposite to the propagation direction of the sound wave [32]. I.a., this approach is advantageous because artifacts caused by optoacoustic signals from outside the region of interest are reduced. In tomography, this means that the illumination is generally oriented radially inwards with respect to the transducer's rotation axis.

The plainest tomographic scan design is set up of a fixed illumination, a fixed sample, and a transducer, which is moved by the scanner (cf. section 4.3). Such scan design has already been employed by multiple research groups (e.g. [55] [56]), but the imaging results have been restricted to 2D images, and still have left potential for increasing resolutions at distinct penetration depths. One of the main reasons for the limitations was that illumination had to be aligned either from the top along the rotation axis, or that projections would get lost if in imaging plane illumination was blocked by the moving transducer. One step towards backward detection was the system designed by Ma et al. [31]. Therein, the mesoscopic imaging of adult zebrafish, particularly the localization of fluorochrome in the zebrafish, was investigated. Due to temporarily varying initial pressure distributions (cf. chapter 2) though, artifacts showed up

in the images. Also, such system design was not applicable for mouse tumor imaging, since the sample had to be rotated. The approach of focusing the light to a sheet was useful for imaging of rather transparent samples, but in highly scattering tissue, such as solid tumors investigated herein, light focusing was not an option, because the high scattering would impede the effect of thinner imaging plane and additionally cause problems with the irradiation exposure limits. In this work, the strategy is, therefore, to use the whole power of the laser and adapt the size of the illuminated area in order not to cause tissue damage. Even if illumination is set to the maximum permissible exposure, for example $20\text{mJ}/\text{cm}^2$ for 532nm [57], it is considered that MPE values are defined for tissue-air interface. In aqueous environment, though, the heat is conducted ca. 22 times better than on air, so thermal damage effects, such as coagulation or carbidization, require higher exposures under water.

One goal was, thus, to essentially invert the experimental design, i.e., to fix the sample and to rotate the transducer, under the condition of still maintaining a constant initial pressure distribution. Except of fixed beam illumination (which comes with loss of projections) the alternative is a quasi-static illumination, i.e., an illumination which provides time-independent light distribution in the sample, although the light guiding optics are moved. Ideally, the light path is not interrupted by the scanned transducer. Before describing these arrangements, I will discuss the necessary components.

4.3.1 Components

Transducers

The choice of the transducer is made according to the subject of interest. The detectable frequency bandwidth is generally adapted to the structure sizes, i.e. the smallest detectable wavelength shall be smaller than the smallest structure of interest. In this work, only transducers without acoustic lenses are considered, avoiding attenuation losses by the acoustic lens material. The focusing is then provided by the curvature of the active element itself. For optoacoustic experimentation, the transducers listed in table 4.1 were used.

Based on the theoretical considerations of chapter 3, the sensitivity fields of the applied transducer are estimated from the diagrams in Fig. 4.7. Since only the sensitivity distribution in

proximity of the focus is relevant for the performed experiments, the Gaussian fit is sufficiently precise (cf. [31]). In case of focusing in only one dimension, i.e. to a focal line, the sensitivities of the transducers used herein are independent of the lateral position, and the widths of the focal zones equal the widths of the detector elements. Such a lateral position independence of the sensitivity field is a necessary condition for tomographic reconstructions.

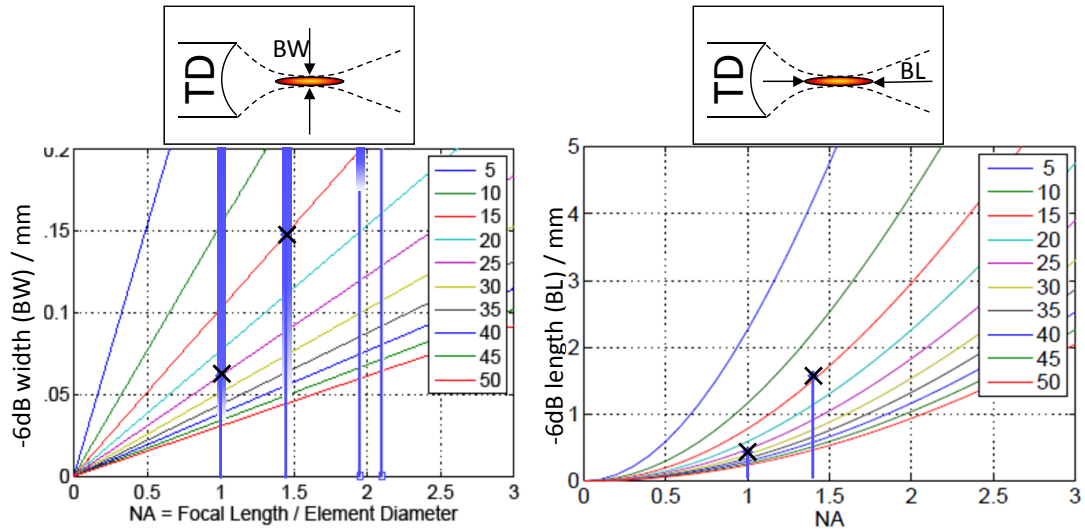


Figure 4.7: Sensitivity fields in Gaussian approximation. Left: Graph of the -6dB beam width in dependency of the numeric aperture evaluated for various frequencies in MHz. Right: Graph of the -6dB beam length in dependency of the numeric aperture evaluated for various frequencies in MHz. Cross markers represent central frequencies of exemplary transducers. Fading bars are indicating the experimentally detectable frequencies of the optoacoustic signal.

The following transducers were applied for detection of the ultrasonic waves These

Transducer	focus	ED [mm]	FL [mm]	fc [MHz]	-6dB bdw. [MHz]	-6dB BW [μ m]	-6dB BL [mm]
PNDT V320	CF	13	25.4	7.5	5.8	400	5.8
PNDT V319	CF	13	19.1	15.28	7.3	150	1.7
IS TF30	CF	12	12	30		50	0.4
PNDT V311	SF	13	25.4	10	7.3	300	4.4
PNDT V312S	SF	6	12.7	20		160	2.6
IS TF25	SF	12	12	25		60	0.5

Table 4.1: PNDT: Panametrics NDT, IS TF: Insensor Thick-Film, CF: cylindrically focused, SF: spherically focused, ED: element diameter, FL: focal length, fc: central frequency, BW: -6dB beam width (at fc), BL: -6dB beam length (at fc)

transducers cover the whole mesoscopic imaging range. Tight focusing, as for the IS transducers, leads to comparably small beam widths, but at the same time very short beam lengths, i.e., depths of fields. Less tight focusing, on the other hand, allows for larger depths of fields, but also comes with larger beam widths. For raster scanning, the larger beam widths directly

translate to lower lateral resolutions, while for tomography they translate to the transversal resolution, i.e., the thickness of the imaging slice. Virtual detector / synthetic aperture focusing techniques have shown to be applicable for longitudinally extending the depth of focus under certain circumstances (cf. section 3.2.2).

It is, therefore, necessary to designate the developed scanning tools presented in this section to the envisioned applications defined by desired resolution, imaging depth and the sample's acoustic and optical parameters. Particularly for raster scanning, the highest resolutions are achieved with the IS TF25. However, its depth of focus is only 0.5mm. It is, therefore, best-applicable for imaging very thin layers that are located at most 10mm from the sample surface in axial direction. If the imaging plane is located deeper within a sample, the transducers PNDT V312S or PNDT V311 are applied. With the latter, the region of interest can be located up to 25mm deep in tissue while allowing for lateral resolutions of 0.4mm. Whole body mouse imaging would be a relevant application. This device requires a different illumination approach, which takes into account the light scattering and absorption.

For tomography, the PNDT V319 provides the thinnest imaging planes. This is advantageous for three-dimensional stacking of image slices. The down-side of the transducer's tight focusing though, is the steep increase of image slice thickness with increasing distance from the center of rotation. The ways to compensate for this effect are described in the following subsection. This effect is weaker for the PNDT V320, since its beam length is more than three times as large. If the transversal (elevation) resolution is not crucial, for instance because three-dimensional stacking is not intended or the transversal side of the imaged structures is sufficiently large, the described effect can be avoided by applying the PNDT V320.

Optical components

In addition to using off-the-shelf optical components such as lenses, mirrors, and light guides for adaptation of the illumination, I designed optical components and systems which are incorporated in the scanning devices described in section 4.3.2. The lenses were optimized for high transmission depending on the envisioned transmission spectrum. The glass material was BK7 ($n=1.51..1.52$ for NIR and 532nm) for spherical and cylindrical lenses and as substrate for mirrors, and UV fused silica ($n=1.46$ for NIR and 532nm) for axicons and custom-made optics.

In both cases, the absorption within the glass is negligible for 532nm and NIR. Since the laser beam was mostly aligned to propagate along the same path for 532nm and 700-950nm, standard high-transmission coatings $T \geq 99.5\%$ (Thorlabs components) were not suitable, hence, uncoated optics were used in those cases. For beam splitting of such a large band, two methods are applicable. The technically difficult way is custom engineering of a special metal-oxide dichroic layer which reflects a certain amount of the light intensity and transmits the rest. This comes with unreasonably high costs. More cost-effective are polka dot beam splitters which are composed of a raster of metal dots (1mm in diameter) on a glass substrate. Commercially available are only Aluminum polka dot beam splitters, which, however, absorb approximately 20% of the pulse energies. To avoid this, protected silver polka dot beam splitters that absorb less than 2% of the light intensity were designed. They were manufactured by Altechna (Vilnius, Lithuania). The reflection to transmission ratios were 1:1 (spot center distance $a=1.347\text{mm}$) and 1:2 ($a=1.65\text{mm}$), allowing to implement two-, three-, and four-side free-beam illumination. Since only a fraction of the beam illuminates the silver, the absorption losses are reduced by the respective fraction, for example for 50% transmission, only 1% of the pulse energy is absorbed.

Another option for combining illumination at 532nm and in the NIR, such as to propagate along the same path, and allow constant illumination geometry at site of the sample, is provided by fibers or fiber bundles. For the laser light used herein, with high pulse energies and peak laser powers of several megawatts, pure silica (quartz) fibers are suitable for flexible, wavelength-independent transmission. For the spectral range of NIR, low OH-content is of advantage to reduce absorption within the fiber. The fibers used herein are of 0.22 numeric aperture, and have a core diameter of 800 μm and 940 μm (HCL-M0800T and HCL-M0940T, Laser Components, Olching, Germany). Their absorption in the NIR is below 8dB/m and 10dB/m, respectively, thus, less than 0.2% of the pulse energy are absorbed for all envisioned wavelengths. At each transition at the uncoated fiber ends, 4% of the pulse energy is reflected if both ends are on air (see equation 2.6). If one of the fiber ends is under water, the total theoretical reflectance will be reduced to 4.4%. The true reflectance will be higher for non-ideal conditions, like non-ideal coupling into the fiber, etc.

The fibers have a specified damage threshold of 10MW/mm².² In the optoacoustic experiments, pulse energies of approximately 30mJ were delivered through the fiber. For the

²manufacturer specification for spectral range used in this work

pulse length of the Vibrant (8ns), the peak power (approximated as twice the average power, Gaussian pulse) was about 7.5MW, hence, well below the damage threshold. The fibers were assembled with high-power SMA connectors (SMA-B930, Laser Components), which were designed to leave the fiber end freely standing. The light was coupled to the fiber by focusing the free beam with a biconvex lens to a spot of the size of the fiber core. The low quality of the OPO beam, thus, permitted applying experimentally determined focal lengths of 3mm for the 800 μ m core diameter fiber and 6mm for the 940 μ m core diameter fiber. Small focal spots will potentially damage the fiber by ablation due to high light fluence, hence, caution needs to be paid to avoid damage at the fiber surface. Also damage sometimes occurs after the first internal reflection or at the output / end face of the fiber due to contamination. For these reasons, coupling of the 532nm direct SHG beam is performed with lenses of 20cm to 30cm focal length. The maximal acceptance angle is not exceeded in any of the coupling geometries.

The light transmission via fiber bundle has a number of advantages over single fiber illumination. For the developments discussed herein, I designed two four arm fiber bundles - one prototype and an adapted final design. The main advantage of fiber bundles over single fibers is the larger frontal surface, i.e., the glass surface at the input, which has 3.6mm diameter for the bundles. A single fiber of 3.6mm core diameter would have a long-term bending radius of more than 40cm, making it inapplicable for illumination of the sample in the optoacoustic tomography and raster scanning designs described in the following sections 4.3.2 and 4.3.3. The intrinsic bending radius of the fiber bundle is instead only 2cm. A stiff PTFE protection tube prevents mechanical damage, increasing the bending radius of the prototype to 5cm. The prototype fiber bundle consists of 260 single fibers of 200/220 μ m core/cladding diameter, initially 1.8m long, which are molten at the input side. The design is shown in Fig. 4.8. In the final design, the protection tube material is a flexible PVC-Kevlar compound, and the output ferrule is reduced to a minimal size to be adapted for tumor imaging with the fiber-bundle-based ring illuminator described in the following. Both, the prototype and the final design are separating the 260 fibers into four arms of 65 fibers per arm. To illuminate in a sheet of light, the fibers are positioned next to each other on a plane in the output ferrule.

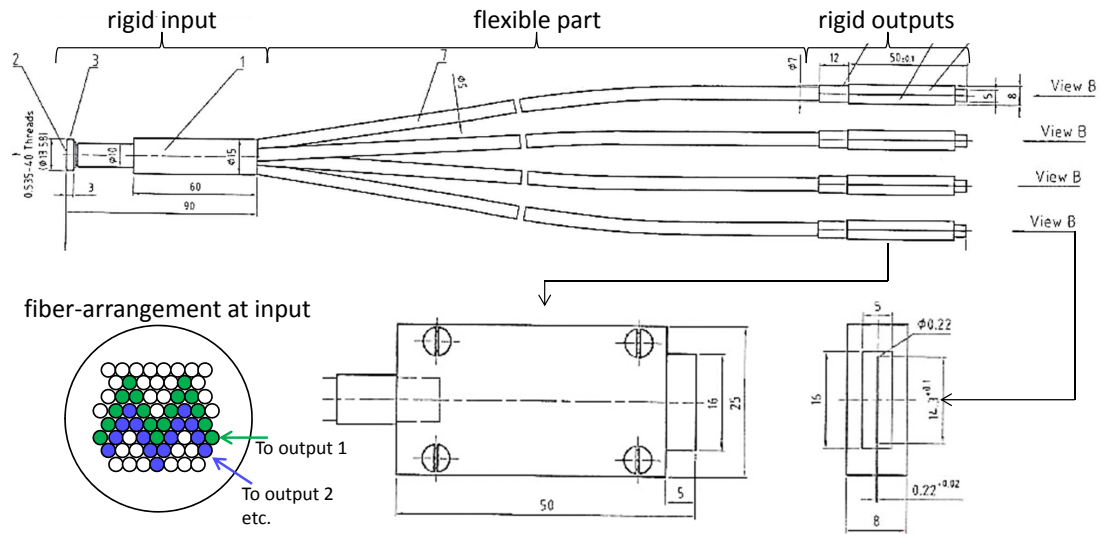


Figure 4.8: Design of the (prototype) fiber bundle. The randomized ("zig-zag") arrangement of the fibers at the input is shown at the lower left.

Mouse holders

I developed three mouse holders, of which two were applied for *in vivo* small animal experiments and will be described in this section. They are shown in Fig. 4.9, and each of them is specifically designated for one of the scanners. Most elaborate is the mouse holder for tomography of tumors, because the mouse may not be entirely immersed in water, but the tumor and the transducer have to be immersed. Former optoacoustic systems for imaging mouse tumors used basins with membranes at their bottom, into which the tumor-bearing mouse was lifted from below. Such design allowed superficial tissue two-dimensional imaging, but the hydrostatic water pressure flattened the back of the mouse and pushed the tumor into the mouse's torso, thus, hindering the scan along the elevational z-axis (see e.g. [56]). By inverting the mouse orientation, i.e., laying it on its back, the tumor may hang into the water, which prevents from squeezing the tumor into the mouse. Other main advantages of the mouse laying on the back are the easy access to the mouse, incl. visual contact throughout an experiment, and the upward orientation of the breathing motion, away from tumor and imaging plane, along the path of least resistance, to consequently reduce the motion artifacts in the image. The implementation uses a cone with cut off tip at 45 degrees base-angle to provide sufficient space for the transducer to be displaced around the tumor.

For raster scanning, the above mentioned state-of-the-art mouse holder is translated to

the tank system developed herein. A mouse holder concept formerly known from fluorescence molecular tomography (mouse compressedly fixed between two plates of glass) was, therefore, adapted to be a water proof box. The unique advantage of placing the mouse in a box is that the Isoflurane concentration in the inhalation narcosis gas can be controlled precisely. On the other hand, access to the animal is limited and water-proofness is difficult to maintain. In order to provide emergency access to the animal, the membrane is not glued on the cover, but it is fixed by an O-ring mechanism as shown in Fig. 4.9. In a developmental stage, this box is employed for tomography. Then, a silicone half cylinder (height: 15mm) is placed perpendicularly to the mouse axis under the belly of the mouse to essentially allow the transducer to rotate around the tumor. The lid of the box is equipped with a polystyrol cone (basis angle 25°) with cut off tip, on top of which is glued a latex membrane with a stretchable hole, through which the tumor is protruding into the water. To further prevent from leakage, a second (PE) membrane covers the tumor and lid, as described above.

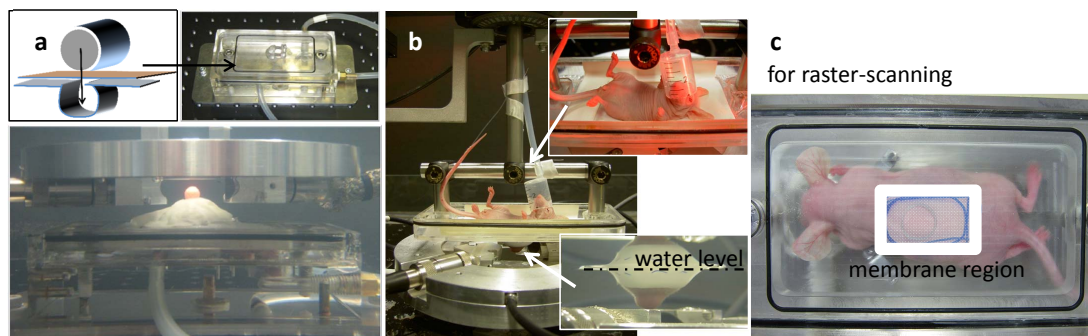


Figure 4.9: The mouse holders. a: Design I for *post mortem* tomographic imaging. b: Design II for *in vivo* tomographic imaging. Insets illustrate position of the mouse and submerged tumor. c: Design III (hermetic box) for *in vivo* and *post mortem* raster scan imaging.

4.3.2 Configuration designs for tomography

Free-beam illumination

The most flexible illumination design is (free-space) direct beam illumination. The laser beam is therein shaped by spherical and cylindrical lenses to irradiate the sample in a manner adapted to the detection geometry. For mouse head vasculature imaging, illumination from the top, as shown in Fig. 7.1, has been applied successfully [58] [59]. However, if the aspect ratio of sample (height to width) becomes larger, such as in the case of subcutaneous tumors, mouse legs, zebrafish or the like, illumination is advantageously directed along the imaging plane

to avoid strong out-of-imaging-plane signals. In the case of three-dimensional tomography, for example by scanning with unfocused transducers and reconstructing by three-dimensional backprojection, the condition of constant and homogeneous illumination refers to the whole sample instead of a two dimensional imaging plane. With multiple beams, the illumination can be adapted to the (expected or predetermined) sample's optical parameters. In a tumor, for instance, the entire tumor surface can, hence, be illuminated uniformly.

In one implementation, the sample is illuminated from four sides, as illustrated in Fig. 4.10. The 532nm beam and the NIR beam are widened by a Galilean beam expander (BE02M-A and -B respectively, Thorlabs) to a diameter of 12mm (measured via spot on photosensitive paper, threshold approx $1\text{mJ}/\text{cm}^2$) to reduce the fluence to below the damage threshold of silver mirrors. The pure 532nm beam is deflected by highly reflective (T1%, HR532) dichroic mirrors (NB1-K12, Thorlabs). The NIR and 532nm beams are each lifted above the level of the tank, and combined through a longpass dichroic mirror (DMLP567, Thorlabs), before being guided to the four-way illumination setup. Subsequently, the light is twice split into two beams by the 1:1 silver polka dot beam splitters, giving a total of four beams. The second beam splitters are positioned at an angle with respect to the first one to result in 25% of the initial light fluence at each beam. In a final step, the spot size can be reduced by concave mirrors to fit to the sample. Taking into account all optical components along the beam path, 91% at 532nm and 88% in the NIR of the initial pulse energy are transmitted to the sample site.

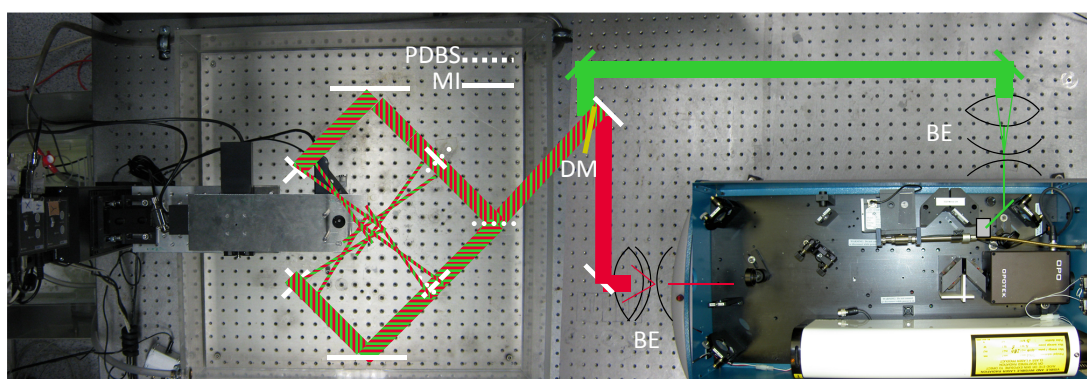


Figure 4.10: Exemplary implementation of the setup for free-beam four-side orthogonal in-imaging-plane illumination of the sample. MI: mirror, PDBS: polka-dot beam splitter, BE: beam expander, DM: dichroic mirror HR 532.

Free-beam ring illuminator

If two-dimensional tomographic images are acquired, a particularly advantageous illumination is a sheet of light with the focal line of the transducer being located within the sheet. In a predecessor setup [31], this has been implemented for bidirectional illumination, i.e., from two sides only. Also in that setup, the sample had to be rotated, making it inapplicable for (*in vivo*) mouse tumor imaging. Furthermore, significant reflection losses had to be accepted at the basin wall, as the light was not directed into the water by the air-water interface directly. Another disadvantage of that design was that a compromise had to be made between space for the sample and propagation path length of the beam, because of high absorption of NIR light by water.

To overcome the above-mentioned disadvantages, a different scanner based on rotating ring illumination was developed, in which the sample is not moved. It is built upon the free-beam illumination described in section 4.3.2 (see Fig. 4.2d). The combined 532nm and NIR beam is lifted above the highest level of the scanner device. It is aligned to finally propagate coaxially to the scanner tomographic rotation axis. To split the beam to a ring shape, it is passed through a plano-convex conical lens (axicon) with 140° apex angle. With equation 2.7, the width of the ring is estimated to be 5.82mm herein. The beam size is further reduced by passing through a biconvex lens, typically of 400mm or 500mm focal length, to essentially increase the transversal resolution of the resulting images. After the ring passes through the hole in the center of the rotation stage, it propagates to the level of the imaging plane, where it is deflected by 81.8° to the sample to illuminate in the imaging plane (see Fig. 4.2d). The deflection is provided by a protected silver coated aluminum ring with a recess for fixation of the transducer, so that the focal line is located in the (illuminated) imaging plane. This scanning design can be used to compensate the effect of image slice thicknesses that increases with the distance from the center of rotation, as described in section 4.3.1. The compensation effect is particularly strong when the scattering coefficient of the tissue is low. The total path length through water is reduced herein to about 5cm. The variance of the light distribution at the sample surface is negligible, herein referred to as quasi-static.

Fiber-bundle-based ring illuminator

The same principle of quasi-static light distribution is exploited for the fiber-bundle-based ring illuminator. When illuminating the sample by means of the above described fiber bundle, the output ferrules need to be positioned in a way not to interfere with the rotating transducer. The output ferrules are, however, too thick for the transducer to pass above / below them, if the ferrules are stationary. Therefore, the ferrules need to be rotated with the transducer during a tomographic scan. In order to provide the same initial pressure distribution for each laser pulse, the output ferrules of the fiber bundle need to be arranged such that the light distribution is the same for each projection, i.e., again quasi-static.

If the sample is highly scattering, keeping the light sheet thin is not helpful for increasing elevational resolution. To the contrary, a thicker light sheet (depending on the sample size and its optical parameters) is advantageous, since it allows increasing the irradiance in the imaging plane. Due to the orientation of the illumination (along the imaging plane), the out-of-plane artifacts are reduced even for thick light sheets. In the case of scattering samples, small differences in the thickness of the light sheet de facto do not change the irradiance distribution deeper than a few hundreds of micrometers from the sample (e.g. tumor) surface. The optimal thickness of the light sheet is, therefore, determined according to the limitation given by the maximum permissible exposure (e.g. $20\text{mJ}/\text{cm}^2$ at 532nm). [57]. In this illumination design, it is neither necessary, nor possible, to control the beam shape as precisely as done in section 4.3.2. Under the requirement of quasi-static illumination, i.e., light distribution within the sample is temporally constant to not over- or underweigh projections. The biggest advantage of the fiber-bundle-based ring illuminator is the flexibility provided by the fiber bundles, especially in the final version (without stiff protection tube), allowing for fast and easy experimentation. The scanner device is shown in Fig. 4.11.

The fiber-bundle-based ring illuminator consists of two rings, the base ring and the output ferrule fixation ring, which are screwed on top each other. The base ring is suspended upon the rotation stage. It is equipped with retaining threads that place the transducer (holding devices) in the predetermined position (taking into account the center of rotation and the focal length of the transducer). The four-arm fiber bundle is fixed onto the base ring by pressing the output ferrules between the base ring and the fixation ring, the fixation ring containing notches for the outlet ferrules. The device is built such that the positioning of transducer and fiber

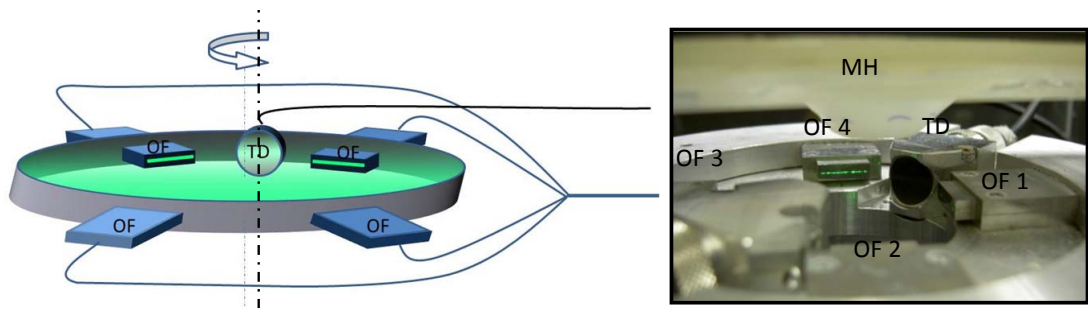


Figure 4.11: The fiber-bundle-based ring illuminator. The fiber bundle output ferrules are fixed on the same plate as the transducer(s) and scanned simultaneously. OF: output ferrules, TD: transducer, MH: mouse holder.

bundles is precisely reproducible.

The ends of the fibers (output ferrule) are fixed 30mm away from the center of rotation, after which the beam has a height (in elevation) of 4mm, determined with the above mentioned burn paper. The laser light is coupled into the fiber bundle by focusing onto the input ferrule surface by respectively coated biconvex lenses (Thorlabs).

4.3.3 Configuration designs for raster scanning

Single fiber coaxial microscanning device

The 'ideal' optoacoustic raster scanner would illuminate the sample along a line. To implement such axial illumination, the transducer IS TF25 is employed. It was specifically designed for illumination along the propagation direction of the sound wave towards the detector. The IS TF25 is equipped with a hole of 0.9mm diameter, which is oriented coaxially to the sound propagation path, and through which a light guide, such as the pure silica fiber with 0.8mm core diameter mentioned in section 4.3.1, is passed. During an experiment, the output end of the fiber may neither protrude into the sound field to disturb the sound field, nor end within the transducer to damage the transducer. The scanning device is shown in Fig. 4.15.

Coupling a low quality laser beam, like the NIR one used herein, into a fiber with 0.8mm core diameter is peculiar, because the minimal focal spot (after focusing by a biconvex lens with 30mm focal length) is only about 0.6mm in diameter. By narrowing the beam by an iris (placed before the focusing lens), a maximum of 7mJ at the output side of the fiber was achieved when both ends were on air. Coupling the 532nm beam required very weak focusing (long focal

length, here 500mm) to keep the maximal fluence inside the fiber below the damage threshold. There, a maximum of 4mJ was transmitted through the fiber on air.

For the given numeric aperture of the fiber ($NA=0.22$), the diameter of the light spot at a distance of 12mm (focal length of transducer) from the fiber end is 2.8mm, if the output end is under water. In order to stay below the maximum permissible exposure (see above), and if the tissue surface is located at 12mm from the fiber end, the pulse energy incident on the tissue may by MPE not exceed 1.2mJ at 532nm. However, these MPE values are not applicable to under-water conditions, because heat is much better transmitted from tissue to water than from tissue to air. In consequence, the field of application of the single fiber coaxial microscanning device is for 532nm illumination superficial tissue imaging (up to 1mm penetration depth). For NIR illumination, the MPE is higher, the scattering coefficients are lower, and, thus, the imaging depth in tissue can be increased. Section 4.4.2 showcases such increase of imaging depth in a phantom experiment.

Confocal microscanning device

The single fiber coaxial scanning device is designed for mesoscopic imaging depths of up to 10mm. This is already implied by the focal length of the transducer. To be able to extend the imaging depth in tissue, I developed a different scanner geometry, which is derived from dark field photoacoustic microscopy, like introduced by Zhang et al. [32]. It is built in a flexible way, allowing to use, for example, the transducers PNDT V311 and V312S. The irradiance limitation witnessed by the coaxial microscanning device is overcome herein by illuminating the sample with a ring, and exploiting the strong scattering of biological tissue to create optoacoustic signal in the focal zone of the transducer. The geometry is similar to the one demonstrated in [32], but it is not limited to microscopy. Other advantages are that the cable of the transducer does not interrupt the laser beam, and that the illuminating beam is point-focused instead of being collimated in itself [32].

The device is illustrated in Fig. 4.12. The laser pulses are therein coupled into the 940 μ m core diameter pure silica fiber. After exiting the fiber, the light propagates through a bi-convex conical lens (BK7, apex angle: 100°, focal length on air: 20mm) to be narrowed and reshaped to a thin ring. Another biconvex lens (BK7, $F=60$ mm on air) subsequently collimates the ring

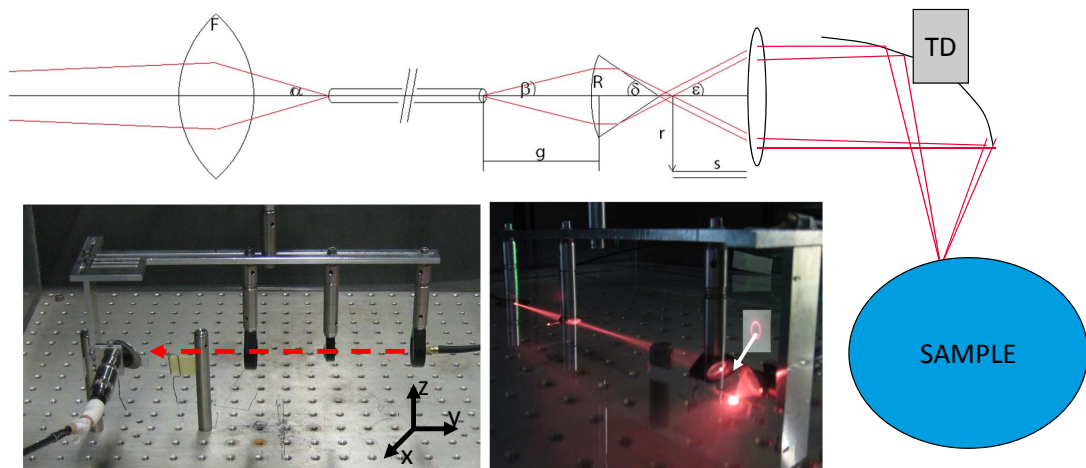


Figure 4.12: The confocal microscanning device. Top: Geometric optics of the light propagation towards the sample showing (from left to right) the coupling lens, the silica fiber, the bi-convex axicon, the refocusing lens and the off-axis paraboloidal mirror. Lower left: Side view on the systematic implementation. Lower middle: Scanning device in operation.

before it is deflected and focused by an off-axis paraboloidal (protected silver) mirror (custom protected silver coating, 02POA011/038, CVI Melles Griot, Bensheim, Germany). The off-axis paraboloidal mirror used in these experiments has a focal length of 10.2mm to be confocal with the transducer PNDT V311, but the design can be readily translated to other combinations of mirror and transducer focal lengths, for example, for larger imaging depths. The mirror has a round hole in the center to position the transducer confocally. The illuminated tissue surface is, thus, $\pi(R^2 - r^2)$, the width of the ring being $R - r$. For an exemplary maximal ring diameter of $R=10\text{mm}$ at a ring width of 2mm, the illuminated surface is 1.13cm^2 . Thus, without exceeding the MPE, 22.6mJ of pulse energy may be delivered onto the tissue at 700nm, and at 800nm 31.7mJ. Proof of concept experiments with this device will be discussed in section 4.4.2.

4.4 Characterization by proof of concept experiments with phantoms

4.4.1 Tomography

To evaluate the image resolution experimentally in addition to the theoretical evaluations (see section 4.3 and chapter 3), I imaged agar phantoms. The agar phantoms were comparable

to those used in the experiments by Ma et al. in [31], in order to provide means for direct comparison of imaging performance and assess the improvements.

Experimental procedure. A schematic of the experimental arrangement is illustrated in Fig. 4.13. The agar gel was prepared as described in section 4.4.2. Herein though, the agar mimicked the scattering and absorption coefficients of tissue, with a highly absorbing insertion in the shape of a hexagon. Hence, at first the background part of the phantom was made with an Allen key as place holder, and cooled to 4°C. Then the Allen key was removed, leaving a hexagonally shaped void with smooth walls near the center axis of the cylindric phantom. Finally, the agar liquid for the insertion, already cooled to well below its boiling point but still fluid, was injected into the void by a syringe, caring to leave no air bubbles in the phantom. The reduced scattering coefficient was set to $\mu_{s'}=10/\text{cm}$ by adding 6% of intralipid, and a background absorption coefficient of $\mu_a=0.23/\text{cm}$ was set by adding india ink to the agar solution before boiling. The cylindrically shaped agar phantom had a diameter of 16mm and a height of 5cm. It was, furthermore, equipped with a five times more absorbing insertion (insertion: $\mu_a=1.15/\text{cm}$) of hexagonal shape aligned along its cylindrical axis. The hexagon was 3mm wide (3mm allen key).

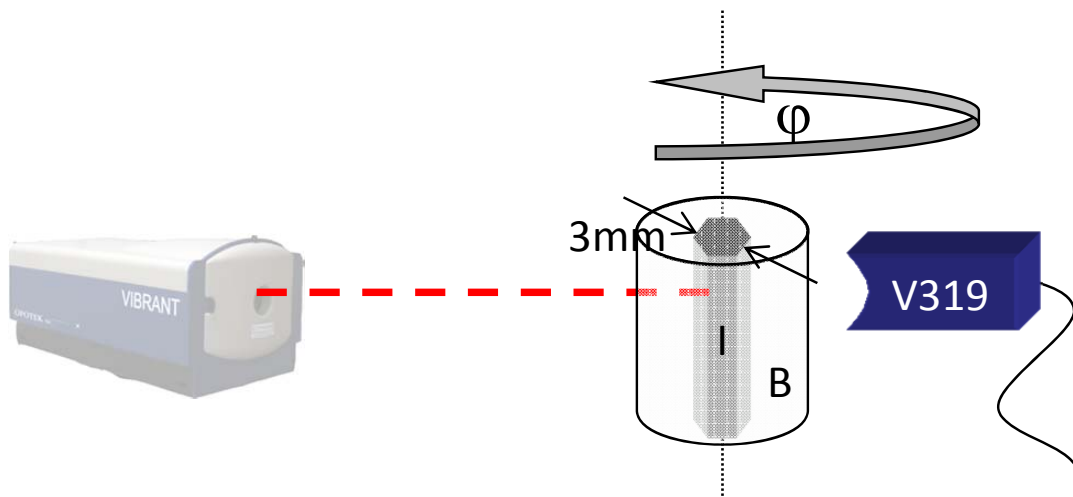


Figure 4.13: Experimental arrangement for imaging the agar phantom with insertion in shape of a hexagon. V319: Cylindrically focused transducer PNDT V319, I: Insertion, B: Background.

The phantom was scanned with the PNDT V319 transducer, which was expected to provide highest tomography resolutions, and was to be employed for tumor imaging. Illumination was in this case provided by one direct, expanded free beam of 12mm diameter oriented along

the imaging plane. The light wavelength was 750nm. Despite this configuration of illumination and detection, similar results are expectable for similar experimental arrangements, as, for example, described in sections 4.3.2 and 4.3.2, as long as the initial pressure distribution is equivalent. The scan covered 360 degrees with one projection per three degrees. Per projection, 110 averages were recorded. The therein used transducer's in-plane resolution was evaluated to be at least 32 μ m in [31].

Results. The imaging results are illustrated in Fig. 4.14 as a comparison between the sum-and-delay direct reconstruction part (top row), and the derivative part (cf. equation 3.7). The pixels are 10 μ m x 10 μ m, thus, significantly smaller than the maximum resolution that the acquisition card provides, and significantly smaller than the tomographic in-plane resolution defined by the transducer frequency band (cf. section 3.1.2). In images 4.14a and d, the insertion I within the agar phantom with background B in the water W is visualized. All sum-and-delay images show the phantom features described above: The agar phantom is evaluated to have 16.0mm diameter (circular cross-section). The size of the hexagonal insertion is measured directly in the image, and by plotting a line profile perpendicular to two parallel edges (see Fig. 4.14). Its width is by both methods determined to be 3.02mm, considering the base points of the insertion in case of determining via the line profile. Beyond the prepared features, structural heterogeneities of the phantom appear in the sum-and-delay images. One of those heterogeneities is the gap-like space in the insertion. Another one takes the shape of a highly absorbing grain. By plotting a line profile through the grain, its cross-sectional full width half maximum (FWHM) was evaluated to be 55 μ m. Furthermore, a gradient in the intensities, decreasing from right to left, is observed in the sum-and-delay images. Therefore, also the right edges appear sharper and in better contrast.

Although the derivative images also show fine structures (see the gap in the center of the insertion or the grain mentioned above) they lack information about the exterior phantom boundary. Also, the wide (low frequency) heterogeneities in the background and in the insertion of the phantom as well as the mentioned light fluence gradient are not revealed in the derivative images. The line plot depicted in Fig. 4.14f points out that the image appears much noisier than in case of direct sum-and-delay.

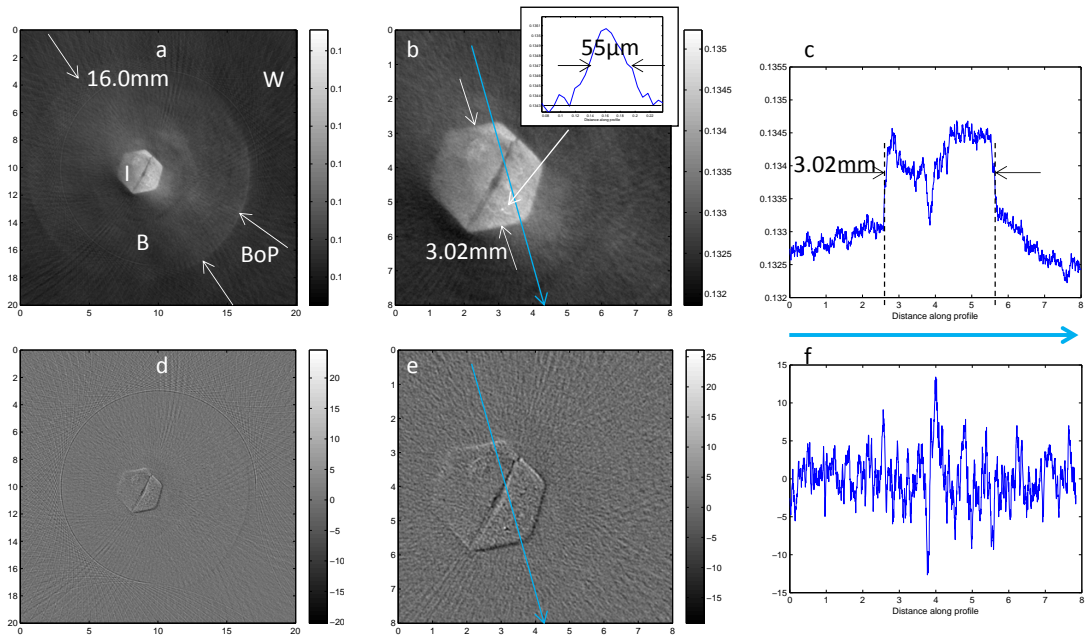


Figure 4.14: Imaging results of the phantom with hexagonal insertion. a-c: Direct sum-and-delay reconstruction performed with unfiltered signal. d-f: Derivative images (reconstruction by sum-and-delay of the time derivative of the signal). I: Insertion, B: Background, BoP: Border of phantom, W: Water. Diameter of the phantom accurately reconstructed to 16.0mm. Width of insertion: 3.02mm. Profile in b: Line plot of a heterogeneity of the insertion appearing with FWHM=55µm in the optoacoustic image. c: Line plot along arrow depicted in b used for determining the width of the insertion.

Discussion. All herein obtained results illustrate the high imaging performance of the developed system for optoacoustic tomography. In particular, the results demonstrate the achieved improvements over conventional optoacoustic tomography system designs. The high precision of the imaging system is, for example, mirrored in the reconstruction of the total phantom diameter, and the width of the hexagonal insertion. Structures smaller than the above discussed grain of 55µm FWHM were resolved. Considering the true in-plane resolution of the system, the respective structure is expected to be 23µm wide. The gradient in pixel intensity decreasing from right to left is clearly attributed to the light attenuation (scattering, absorption), which stands in accordance to the initial orientation of the laser beam.

Unlike the direct sum-and-delay algorithm, the algorithm based on the time-derivative of the signal is not potent enough to extract all information of the digitalized signal. Details that are crucial for complete visualization of the phantom are missing. This effect is typical for an edge filter. Therefore, its applicability to optoacoustic (biomedical) imaging is strongly restricted - namely to those cases where only the edges are of interest. This is never the case in the experiments presented in this work, which is why the derivative backprojection reconstruction will not be further regarded. It shall be noted, that even when only the edges are of

interest, a plain edge filter can be applied to the images.

4.4.2 Raster scanning

Microscanning through tissue

In this phantom experiment, a cross printed on paper and a 5mm x 5mm field of a business card were C-scanned with the single fiber coaxial microscanning device at several experimental parameters.

Experimental procedure. The experimental arrangement is shown in Fig. 4.15. Both samples were wrapped with transparent scotch tape to avoid soaking of the paper. At first, the business card was investigated. Therefore, it was fixed in horizontal position. The scanner device described in section 4.3.3) was positioned above the business card in (z-)distance equal to the focal length of the transducer³, and the basin was flooded with water. The irradiance was low enough to avoid bleaching of the ink. The x-axis and the y-axis were scanned in 50 μm steps. The z-position was constant. For each projection, the signal was averaged 5 times, in order to reduce the effect of pulse energy fluctuations.

In the first experimental configuration, scans were performed with 532nm illumination. Then, slabs of turkey breast of various thicknesses were placed onto the business card to image the business card through the tissue. The experimental parameters for scanning the business card through up to 7.0mm of tissue were determined. To confirm the resolution calculations of the imaging device, and further assess applicability for biomedical imaging applications, the cross printed on paper was scanned in-focus and 1.5mm out-of-focus. The illumination wavelength was 750nm. Validation was performed by optical transmission microscopy. The optoacoustic signal was filtered between 12 and 24MHz. All images were reconstructed by maximum amplitude projection (C-scans) of the bandpass filtered signal curves for various sets of high-pass and low-pass frequencies, out of which the best-suited filter was identified with regard of the image resolution and integrity for the business card scans.

³accomplished by moving the transducer to a position (distance from the business card) where the optoacoustic signal amplitude was maximal

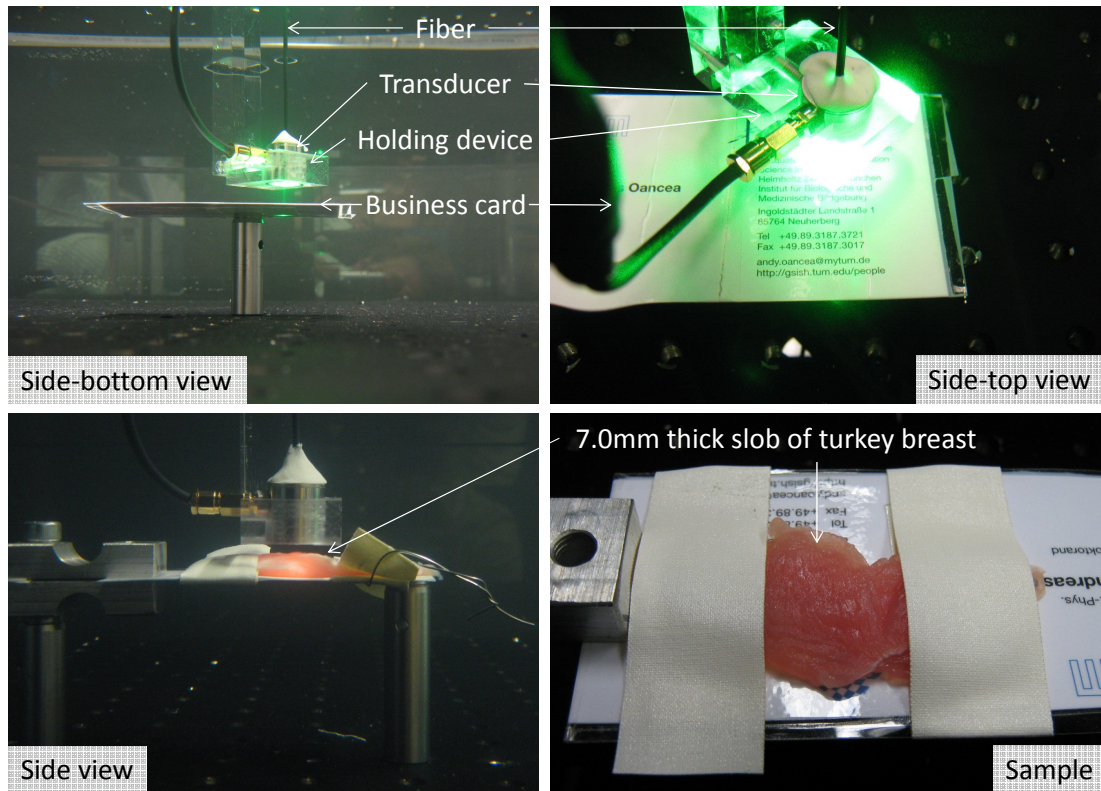


Figure 4.15: Experimental arrangement for microscanning through a 7mm thick slab of turkey breast. Top row: arrangement without tissue. Bottom row: arrangement after placing the tissue on top of the business card.

Results. The C-scan images are shown in Fig. 4.16 as comparison to business card images scanned by a flat-bed scanner at 600dpi scanning resolution. For 532nm illumination without the tissue, the optoacoustic image is resolution- / sharpness-wise comparable to the image of the flatbed scanner, performed at 600dpi, which was the highest possible resolution setting of the flatbed scanner. The zooms demonstrate that the variances in the pixel intensities do not only occur in the optoacoustic images, but also in the flatbed scan images. The resolution-wise best-suited high-pass and low-pass frequencies were 8 and 48 MHz. After a 1mm thick slab of turkey breast was placed onto the business card, the optoacoustic signal was so low, that more than 20 averages were necessary to reduce the noise threshold to below the signal level. Therefore, the illumination was switched to 750nm for all further experiments with tissue. The resulting image for 7.0mm tissue thickness reveals that structures in focus can be clearly resolved, as if there was no tissue (see, e.g., the "76" in the image). However, if the sample is moved slightly out of focus, artifacts, such as shown nearby the letters "go", appear in the image. In the example shown here, they take the shape of shadows around the true structures. Remarkably, a misspelling was found only after scanning the card optoacoustically:

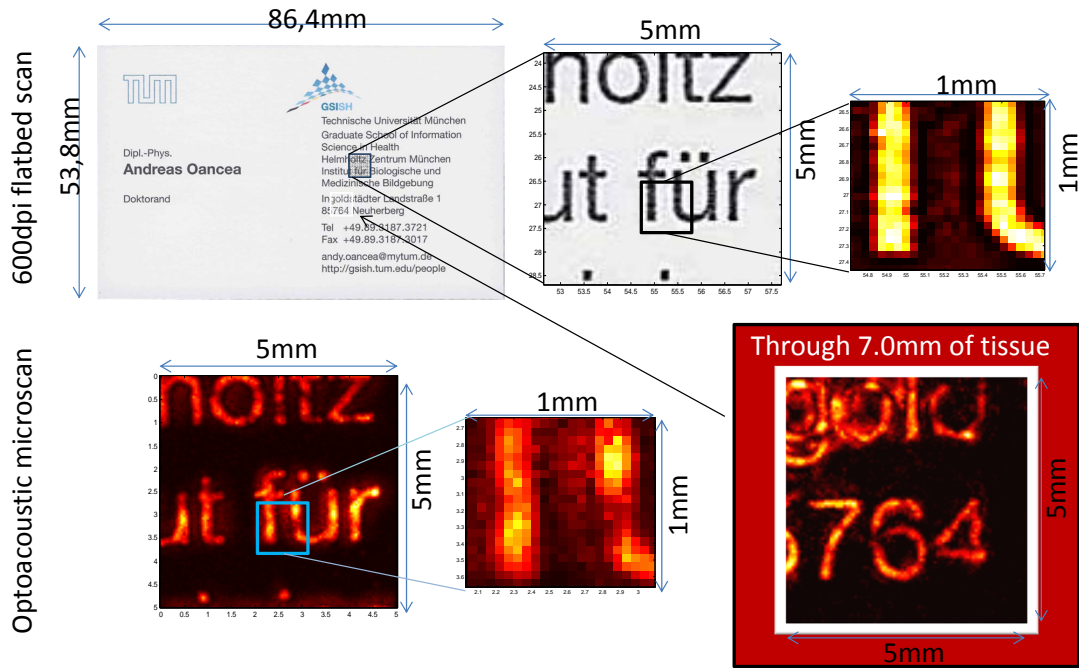


Figure 4.16: Results for microscanning through a 7mm thick slab of turkey breast. Top row: business card scanned by a flatbed scanner, zoomed and analyzed on a pixel-by-pixel level. Bottom row: Optoacoustic microscan without tissue and through 7mm of turkey breast of the regions indicated by the arrows.

"IngOLSDtätter" is written on the card, when in fact "IngOLStätter" is correct. For imaging through tissue, the high-pass and low-pass frequencies were again set to 8MHz and 48MHz, however, the signal intensity was very low for high frequencies.

The resulting cross images are shown in Fig. 4.17. The true width of the lines is $50\mu\text{m}$. The central region is $150\mu\text{m}$ wide. In the optoacoustic images in focus, the lines are approximately $170\mu\text{m}$ wide (full width half maximum, FWHM), equaling the beam width at 12MHz plus the true width of the lines. However, in proximity of the intersection, the two lines can only be resolved (FWHM criterion), if their centers are separated by at least $220\mu\text{m}$. If the transducer is positioned 1.5mm higher, thus, out of focus, the lines become already more than $680\mu\text{m}$ wide.

Discussion. The results show that the imaging precision obtained from the optoacoustic scans is comparable to the flatbed scanner images. With NIR illumination, the scan can be performed through several millimeters of tissue, herein shown for 7.0mm of turkey breast. However, by illuminating at 532nm, imaging cannot even be conducted through 1mm of tissue during reasonable experimental times. Strong scattering of the tissue causes the signal intensity to be

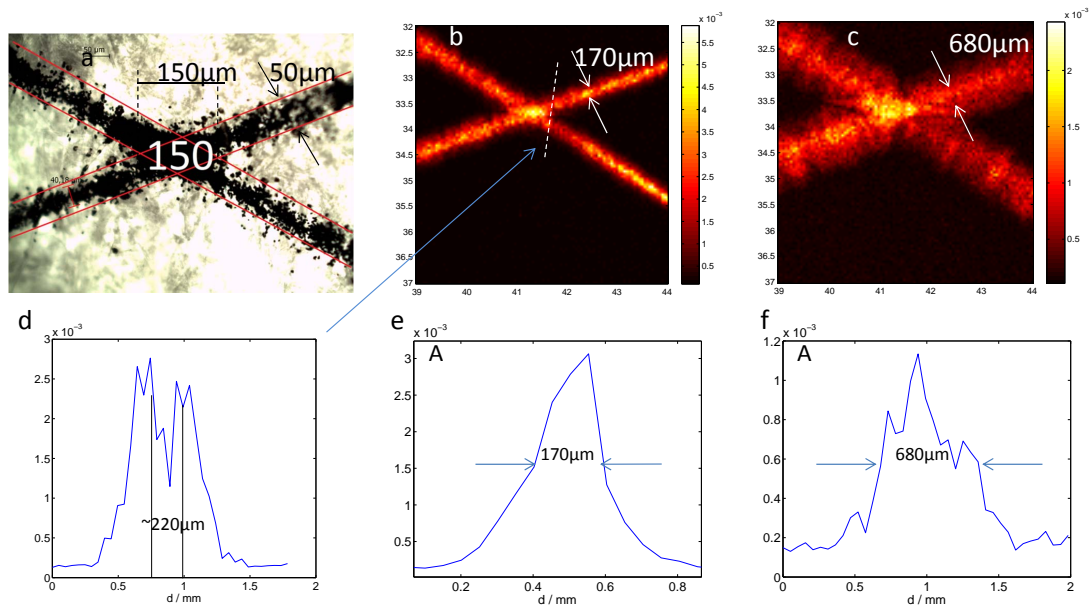


Figure 4.17: Results for microscanning the cross printed on paper. a: Light microscopy of the cross printed by the laser printer onto standard white paper showing the true width of the cross ($150\mu\text{m}$) and lines ($50\mu\text{m}$). b: Optoacoustic microscans of cross / lines when scanned in focus. c: Optoacoustic microscans of cross / lines when scanned 1.5mm out of focus. d and e: Line profiles along lines indicated in (b). f: Line profile along line indicated in (c).

too low in that case. The shadow structures appearing when imaging through the tissue slab indicate a strong influence of parasitic signal. This signal might be caused by scattering effects. The more probable reason is, however, that the business card was not fixed perfectly parallel to the imaging plane, so that certain regions of the sample were out-of-focus. How low the resolution becomes in that case, is demonstrated in the cross images. Already a displacement of 1.5mm out of focus causes a $50\mu\text{m}$ line to appear more than twelve times as wide. Even though the results point out that the calculated beam widths are reflected in the experiment, they also reveal that two of these lines cannot be separated when approximately in focus, if they are closer than $220\mu\text{m}$ apart and the signal is high-passed at 12MHz . The lateral uncertainty is thereby approximately one pixel, thus, $\pm 50\mu\text{m}$. Higher high-pass frequencies may optionally be applied to further increase the resolution, which, however, would reduce the SNR to essentially reveal grainier images. Translated to vasculature imaging, this implies that, for example, subcutaneous vasculature of mice and humans would be well imageable, as long as the vessels are far enough apart. For the scanner configuration shown here, this means that the vessels shall be at least $220\mu\text{m}$ apart. This is, however, not the case in tumor microvasculature.

Confocal point raster scanning

In this phantom experiment, a raster of graphite fibers, as well as an agar phantom with a randomly shaped hair inside, were scanned with the confocal microscanning device described in section 4.3.3 with the PNDT V311 transducer. The goal was to assess the imaging performance of the system and identify suitable applications.

Experimental procedure. The experimental arrangement is illustrated in Fig. 4.12 and the samples are shown in Fig. 4.18. The graphite fibers were $70\mu\text{m}$ thick, and they were taped between two stripes of scotch tape to remain in a fix position. The distances between the fibers were 5mm, 2.7mm and 1.3mm horizontally and vertically, as shown in Fig. 4.18. For experimentation, the tape with the graphite fibers was stretched between two mounting rods, so that the imaging plane was of y-z-orientation. The fibers were scanned in focus. Herein, the acoustic focus coincided with the optical focus.

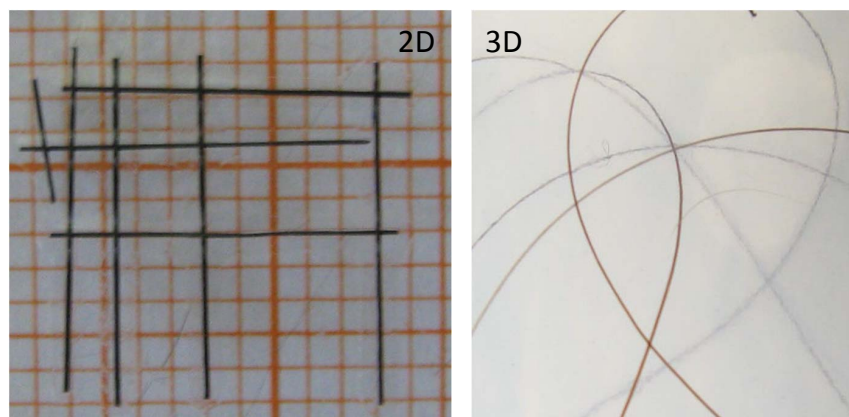


Figure 4.18: Photographs of the samples for confocal point raster scanning. Left: 2D sample raster of graphite rods. Millimeter paper in background. Right: 3D sample of dark brown human hair randomly inserted in transparent agar.

The agar phantom was built as follows. A 1.3 m-% agar gel matrix was prepared by heating an aqueous solution of 1.3g agar powder (Sigma-Aldrich) in 100ml of distilled water to its boiling point. The agar was poured into a 3cm x 2cm x 1cm (WxHxD) PVC form, after which a $70\mu\text{m}$ thick long dark brown human hair was brought into the liquid in a random shape to provide a three-dimensional structure. For hardening, the phantom was cooled in a fridge to 6°C . Only the central 1cm x 1cm x 1cm were scanned, but in this case also in x-direction, such as to essentially raster the focal point through the phantom. The step size in x-, y- and z-direction was $100\mu\text{m}$.

For the two-dimensional graphite fiber grid, maximum amplitude projection (C-scan) is applied to reconstruct the images. In the case of the agar-hair-phantom, reconstruction was at first performed by point-by-point assignment of the pixel values to a three-dimensional grid of corresponding size. Then, the virtual detector technique was applied to extract three-dimensional information from only two-dimensional scans (here y-z). Before all reconstructions, the signal was high-pass filtered at 10 MHz, i.e., at the nominal central frequency of the transducer.

Results. The results are shown in Fig. 4.19. The graphite fibers appear to have a width of approximately $400\mu\text{m}$ in the optoacoustic images, which roughly corresponds to the true width of the graphite fibers plus the -6dB beam width of the transducer at the central frequency ($300\mu\text{m}$ at 10MHz) plus a tolerance (sub $100\mu\text{m}$) that arises from the confocal illumination due to the localization tolerance of the light focal spot. Such focal spot tolerance is irrelevant for optoacoustic imaging of scattering samples. Although the entire graphite fiber grid is shown in the figure, the right half of the grid is not as clearly visible as, for example, the vertical graphite fiber at the left.

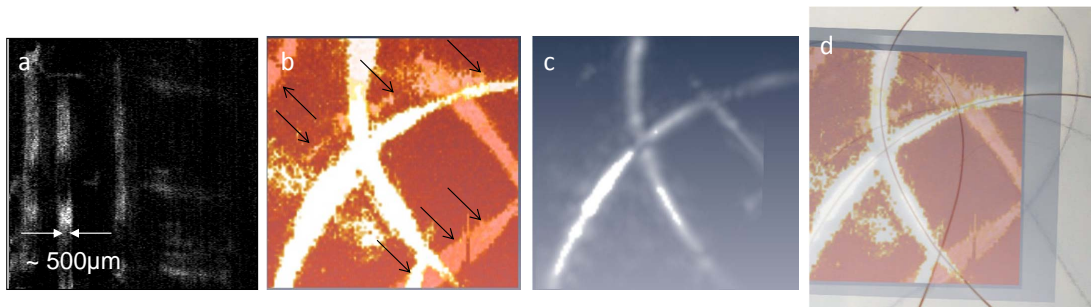


Figure 4.19: Results of confocal point raster scanning. a: Result of 2D scanned raster of graphite rods. b: Three-dimensionally scanned hair-in-agar phantom reproducing the shape of the hair insertion. c: Two-dimensionally scanned virtual detector corrected hair-in-agar phantom showing to better resolve the hair width, but missing structures marked with arrows in (b). d: Overlay of (b),(c) and the photograph of the sample.

In the three-dimensionally scanned hair phantom, the hair appears significantly thicker than it really is. Its thickness in the optoacoustic images is depending on the depth position, as shown in Fig. 4.19b. However, comparison with the true shape of the hair shows that de facto all parts of the hair are detected. An overlay of the optoacoustic image with a photograph of the phantom shows how well the true geometry is reproduced, despite the low resolution. Herein, only one section of the hair does not appear in the optoacoustic image, because it

had protruded out of the scan range (closer to the transducer). In case of virtual detector reconstruction, a significant amount of parts are missing in the optoacoustic images, but the image hair thickness is constant and reduced as compared to the three-dimensional scan.

Discussion. By confocal microscanning, a free-standing fiber grid as well as a three-dimensionally shaped hair in agar were imaged. For validation, the fiber grid as well as the hair were inspected visually and compared to the optoacoustic images. The graphite fiber grid showed imaging deficiencies on the right side of the images, which part of the phantom deviated from the focal plane. However, the PNDT V311 has a long depth of focus (more than 4mm), which is why the effect is due to the light focusing. Similar to confocal optical microscopy, this effect can be very advantageous when a short depth of focus is wanted and the scattering of the medium is low. In consequence, the confocal microscanning device is expected to have its key applications in the whole mesoscopic imaging range: For superficial (biomedical) imaging, the optical focusing provides lateral resolution superior to the transducer beam width. The larger the imaging depth becomes, the more diffuse becomes the irradiance, and the more the focusing becomes of acoustic type. Conventional optical resolution or acoustic resolution photoacoustic microscopy systems cannot provide this discussed combination, since they employ a simply converging (not point-confocal) ring illumination [21] [60]. In optical resolution mode, the laser power is reduced according to the exposure limits. The acoustic beam width is then not relevant for the image lateral resolution (cf. [61]). However, the transducer shall still be focused to provide high acoustic sensitivity in the optical focal spot.

When imaging the hair phantom in pure agar gel, the fully three-dimensional scan allowed to optoacoustically reproduce the shape of the hair. Purely two-dimensional reconstruction with the virtual detector (VD) method was not sufficient to reproduce the entire shape, pointing out a key limitation of the method. Although the VD method is powerful to axially extend the focal zone⁴, it requires sufficient signal from the structures that are placed out of focus, which is not necessarily given, considering the true sensitivity field of the transducer. In consequence, this is one of the reasons why its applicability has so far been limited to the imaging field dimensions of photoacoustic microscopy.

⁴Note: The diffraction-limited minimum width of the beam is not affected by this method.

4.5 Conclusion for tumor imaging experiments

Before proceeding to biological experiments with tumor-bearing mice, it is herein concluded which of the described system designs is best-suited for the envisioned mouse tumor imaging, and why. The tumors of interest are subcutaneous tumors, thus, located in and below the densely vascularized subcutis. They protrude from the back of a (herein nude) mouse by a few, typically by about 4, millimeters, whereas the tumor whole shape is essentially paraboloidal, thus, also protruding into the mouse torso. Such a tumor is shown in Fig. 5.1.

Already the geometry of the tumor hints towards tomographic scanning. In addition, some major systematic characteristics of optoacoustic imaging indicate that tomography is indeed suited better than raster scanning for investigating the entire tumor. These systematic characteristics are based on the potential to resolve the microvasculature and heterogeneities deep within the tumor. The literature, for example [28], shows that tumor microvessels have diameters of well below $50\mu\text{m}$, often even below $30\mu\text{m}$. Moreover, they are randomly oriented. Assuming resolutions of $30\mu\text{m}$ have to be achieved, which are given for tomography with the PNDT V319, in the case of raster scanning detection bands above 50MHz are necessary even in the case of numeric apertures as low as $NA=1$ (cf. Fig. 4.7). At a frequency of 50 MHz however, under the (in best approximation) valid assumption that tumor tissue damps the ultrasound approximately like fat, only 5.6% of the optoacoustic signal amplitude is left over after passing through 5mm of such tissue [39]. At 25MHz, i.e., at a frequency allowing $30\mu\text{m}$ in-plane resolution in the tomographic approach, the damping through tissue of the same thickness is 4.2 times less.

Furthermore, a transducer with $NA=1$, detecting signals of 50MHz frequency has a focal zone that is only about $300\mu\text{m}$ long (-6dB beam length), requiring the application of algorithms to extend the focal zone. This problem is showcased in the business card experiments discussed in section 4.3.3. In systematic experiments for investigating the applicability of virtual detector focusing, however, the method showed to hide parts of the phantom in the images (cf. section 4.4.2). Further experiments not discussed herein, proved that the beam length is not sufficiently extendable, which would cause low imaging resolutions and artifacts in the images (cf. section 4.3.3). One possible reason for this is the non-flat, typically even non-spherical shape of the tumor at the interface between tissue and water. Uncertainties may arise from the acoustic impedance mismatch at the tissue-water boundary and the speed of sound difference between

water and tissue.

In conclusion, the arguments for using optoacoustic tomography to scan tumor vasculature, based on characterizations presented in this chapter, outweigh those for raster scanning. Particularly, high depth-independent in-plane resolution of tomography promises precise views on the tumor vasculature not only superficially, but at all depths below the top of the tumor. All these considerations equally apply to other samples of interest which require similar imaging performance, like zebrafish in the early developmental stage (cf. section 7.1.3).

Chapter 5

Optoacoustic tomography of tumor vasculature *post mortem*

The work presented in this chapter aims at comparing different tumor cell lines, tomographic system designs, and validation methods. The purpose is deducing a benchmark experimental configuration that appears best-suited for *in vivo* optoacoustic tumor investigations, comprising the ideal placement of the animal, the optimal illumination and detection for imaging the tumor at different depths and resolutions, and respectively applicable contrast agents like fluorescent probes or nanoparticles. Therefore, three sets of major optoacoustic experiments were performed, successively extending the imaging depth from superficial to profound by adapting the system design.

The employed hardware has been described in section 4.3. In **section 5.1** of this chapter, I extend the materials characterization to the specimens (i.e., mouse tumors) of interest and to the applied contrast agents. In **section 5.2**, optoacoustic imaging as well as validation methods are discussed in detail, including the performed set of optoacoustic experiments. It describes each of the experimental arrangements and experimental procedures. The imaging results and findings regarding system integration are discussed, and conclusions with respect to advantages and disadvantages of the experimental procedures are made, in order to point out how the optimized *in vivo* experiment can be performed.

5.1 Materials for experimental cancer imaging

5.1.1 Animals and tumors

Animal models were developed and imaged according to procedures approved by the government of Bavaria. The animals used in all experiments presented in this work were female CD1 nude mice (Charles River Laboratories, Sulzfeld, Germany) weighing 25g (± 3 g). Since the mice were nude, light and sound were not scattered by hair. Furthermore, light absorbing spots due to skin irritation eventually arising from hair removal did not cause unwanted optoacoustic signals. Before the actual optoacoustic experiment, a predetermined amount of cancer cells was injected into the subcutis of the mouse to grow a tumor like shown in Fig. 5.1. The employed tumor cell lines were 4T1 mouse mammary carcinoma (ATCC CRL-2539, ATCC Manassas, VA, USA), HT29 human adenocarcinoma (ATCC-HTB-38, ATCC Manassas, VA, USA), and A2780 human ovarian carcinoma (Sigma-Aldrich, St. Louis, MO, USA) (cf. section 5.2.1).

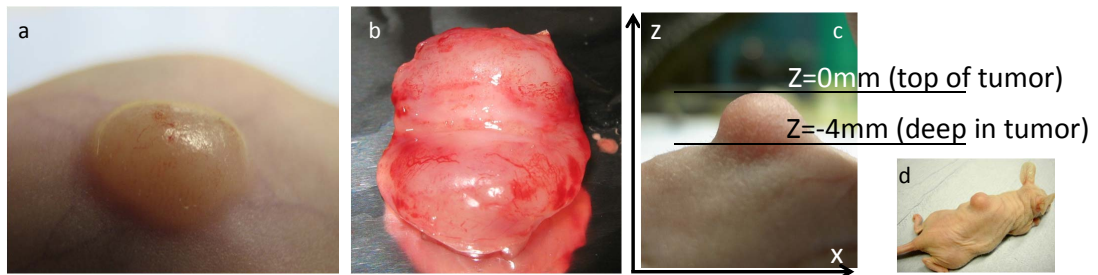


Figure 5.1: Photographs of solid subcutaneous tumors, i.e., subjects of interest. a: Subcutaneous 4T1 tumor in the center of the back of a mouse. Major subcutaneous supply vessels can be seen visually to approach the tumor from substantially four sides. b: Macroscopic photograph of excised tumor showing how blood vessels clasp around the tumor. c,d: HT29 tumor in the center of the back of a mouse. The scanning coordinate system and orientation of the tumor during scans are depicted.

The composition, consistence and optical appearance of the different solid tumors are dependent on the cell line. For example, HT29 tumors are typically softer than the comparably stiff 4T1 tumors. To obtain more quantitative information of the physical properties of the tumors, a set of experiments was performed, and will be discussed in the following. By taking into account the determined physical properties for the reconstructions of the optoacoustic images, the reconstructions become more accurate. Furthermore, characterizing the physical properties of the tumor is helpful for choosing a tumor model for further investigations, such as *in vivo* tumor imaging presented in chapter 6, and it helps for avoiding experimental errors.

Speed of sound in the tumor

In an ideal optoacoustic tomography experiment, the speed of sound in the sample (herein: tumor) equals the speed of sound in the coupling medium (cf. section 3.2).¹ The more the speed of sound in the sample differs from the speed of sound in the coupling medium, the more relevant signal distortions will become for the reconstruction of the optoacoustic images. From this perspective, it is advantageous to choose a tumor, whose speed of sound deviates the least from the speed of sound in water. The speed of sound in tumor tissue was evaluated for HT29 and 4T1 tumors in (one projection) optoacoustic experiments, by determining the runtime difference that an ultrasound wave package witnesses when propagating through a tumor (water to tumor to water) compared to the direct propagation (only through water). Fig. 5.2a illustrates the experimental arrangement for determining the speed of sound in tumor tissue.

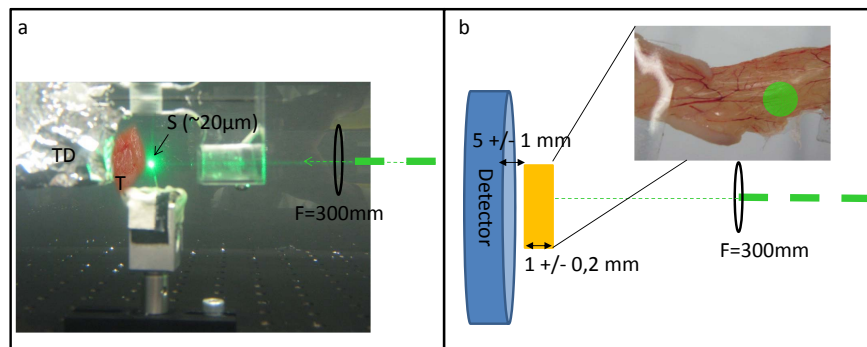


Figure 5.2: Experimental arrangements for determining the speed of sound in tumor tissue optoacoustically and qualitative wavelength dependence of attenuation in mouse skin. a: Photograph of the setup with overlaid tumor (T) and lens (F=300mm). The graphite hair sample (S) acted as sound source. The transducer (TD) was covered in aluminum foil to avoid damage and parasitic signals. b: Schematic of the experimental configuration for qualitative assessment of the wavelength-dependency of light attenuation by mouse dorsal skin.

Therein, a 532nm laser beam was focused onto the tip of an approximately 20 μ m thin graphite hair to create a spherically expanding optoacoustic pressure wave. The transducer PNDT V319 was aligned so that the sound source was located in the focal spot of the transducer (maximized signal, bipolar). The signal was recorded once with a tumor placed in proximity of the sound source between sound source and the transducer, and once without the tumor.

The result of this experiment was that the speed of sound in tumor tissue showed to be 2% (HT29) and 5% (4T1) higher than in water. As the speed of sound difference between tumor tissue and water is negligibly small, a model with a uniform speed of sound is acceptable

¹The same applies to the acoustic impedance, cf. section 2.4

for performing the reconstructions.

Light attenuation in the tumor

Since optoacoustics visualizes optical contrast, the optical properties of the optically inhomogeneous tumor tissue are typically more influential for the appearance of the image than the acoustic properties.² Although determining the exact optical coefficient values was not necessary for the experiments presented herein, a rough estimation of light damping (scattering and absorption) was helpful. In order to assess which imaging depths may be expected at which illumination wavelengths, an experiment was performed. The corresponding setup is illustrated in Fig. 5.2. Therein, light was focused to a spot of approximately 3mm diameter onto the specimen, and the irradiance transmitted into the semi-infinite space ($1.8 \pi \text{sr}$) behind the specimen was measured to determine the total transmittance. The specimens were a 4T1 tumor of 3mm diameter and a 1mm thick slab of skin from the back of a mouse.

The results showed for 700nm illumination wavelength 49% transmittance through the tumor, and 45% transmittance through the skin. In case of 532nm illumination, these values decreased to only 17% and 15%, respectively. The transmittance herein summarizes a series of physical processes: the initial reflection at the air-tissue boundary, the absorption and scattering throughout the tissue, the reflection at the tissue-air boundary, and theoretically percent internal reflections between the two boundaries (which are expected to play a minor role, though). The reflectance at the first boundary in propagation direction (air to mouse skin) was directly evaluated to be $R=2.8\%$ by the fresnel equation 2.6 under consideration of the refractive index of mouse skin valuing 1.4 (456nm-1064nm) [62]. In water (refractive index $n=1.33$, see section 2.2), as is the case in optoacoustic experiments presented in this work, the reflectance at the water-tissue boundary is much lower. In both cases (air-tissue and water-tissue), however, the main contribution to light attenuation is the attenuation within the tissue. Reflectance on the other side of the skin may slightly differ due to the layered structure of the skin. However, the refractive indexes of those other layers, like cutis and subcutis, as well as the tumor are expected to not deviate significantly from that of skin, since they are still mouse tissue (cf. [23]). Altogether, the contribution of reflectivity at the air-tissue (or water-tissue) boundaries is, therefore, (well) below 6%.

²assuming acoustically homogeneous tissue

In conclusion, this means that all the remaining attenuation (over 45% at 700nm and over 77% at 532nm) is attributed to the scattering and absorption within the tissue. Hence, the light attenuation in skin is much higher than in the tumor. It is also derived from the findings that the true in-imaging-plane irradiance needs to be lower than the herein discussed transmitted irradiance (assuming the imaging plane is thinner than the diameter of the photo-detector). This essentially means that within the imaging plane, at 532nm (significantly) direct illumination, less than 15% of the pulse energy reach the tumor tissue at all, implying that light fluence correction algorithms and sample-adapted illumination designs need to be applied, as discussed in chapter 4. In conclusion, for whole tumor imaging, NIR illumination will be indispensable.

Optical contrast in mouse tissue (including tumor tissue) is strongly wavelength-dependent. Therein, the optical contrast intrinsically arises from oxygenated and deoxygenated hemoglobin (chromophore of blood) and other intrinsic absorbers, such as (skin) pigmentation, or even the water content for illumination wavelengths above 800nm (cf. appendix A.1). For imaging depths above 1mm, illumination wavelengths in the therapeutic window, i.e., above 600nm (reducing absorption by hemoglobin) and below 1300nm (increasing absorption of water) are preferred [23]. However, for superficial imaging of subcutaneous tumor vasculature, illumination wavelengths below 600nm provide high intrinsic contrast of blood vessels. This will be discussed in the following section.

Blood vessel contrast

Above, the advantages of NIR illumination for profound imaging are discussed. However, one major disadvantage of optoacoustic imaging with NIR illumination is the inherently reduced blood vessel contrast compared to 532nm illumination. From the mere fact that blood has a higher absorption coefficient in the visible than in the NIR, predicting the difference in blood vessel contrast of optoacoustic images acquired with 532nm illumination and especially 700nm (or NIR) illumination is difficult. The following experiment helps to estimate the contrast and morphology of blood vessels in optoacoustic images at 532nm vs. 700nm (NIR) illumination wavelengths. Therein, reflection images (photographs) of the above mentioned tumor and slab of skin were acquired. The reflection images are shown in Fig. 5.3 as RGB color images and decompositions into the red, green, and blue component.

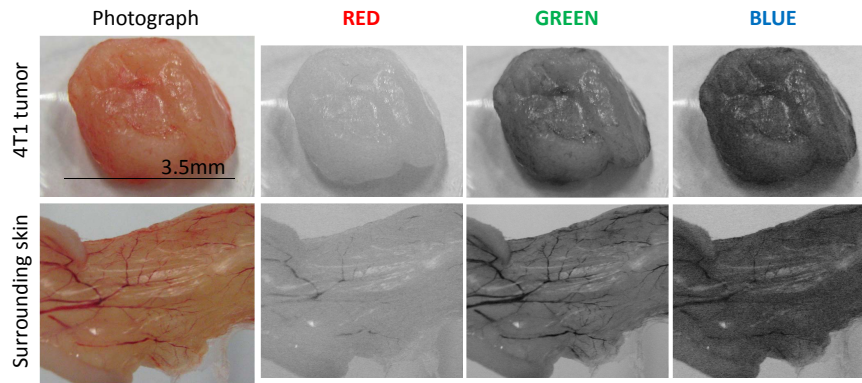


Figure 5.3: RGB decomposition of photograph (reflection image) of a tumor and surrounding skin under white light illumination on a white table.

Physically regarded, the brighter a pixel appears in a reflection image, the more of the (incoherent) incident light is reflected in the respective wavelength (color) range.³ For simplicity, it is, furthermore, assumed that the tissue sample is infinitely thin and the sample or the table do not transmit light ($T=0$). The background of the image was clear white (table), thus, equally reflecting all wavelengths. In the red component image, the blood vessels appeared in low contrast to the background tissue and table, because of the low absorption of red light by hemoglobin (cf. absorption spectra of oxygenated and deoxygenated hemoglobin in appendix A.2). In the green component image, however, the blood vessel contrast was high, since hemoglobin absorbed the respective green light.

In conclusion, it is expected that in the optoacoustic images acquired with green (532nm) illumination will provide high blood vessel contrast comparable to the contrast shown in Fig. 5.3, but it will be limited in penetration depth, whereas NIR illumination will be the key for increasing the imaging depths, on the expense of blood vessel contrast. To combine high blood vessel contrast with high imaging depths, exogenous contrast agents that specifically accumulate in the structures of interest (e.g., blood vessels) are applied for optoacoustic imaging.

5.1.2 Contrast agents for MSOT

In the optoacoustic imaging experiments presented in this and the next chapter, various types of exogenous contrast agents were injected before or during the experiments into the tail vein of

³Since the spectrum of the laser covers green and red (and NIR), the blue image is irrelevant for the considerations.

the mouse, in order to increase the NIR imaging contrast of blood vessels versus the surrounding (tumor) tissue. As described above, optoacoustic images show absorption contrast. Therefore, only contrast agents absorbing in the NIR spectral range covered by the laser, i.e. 700nm to 950nm, are relevant. The investigated contrast agents were the fluorochromes indocyanine green (ICG, Pulsion Medical Systems) and Alexa Fluor, on which the blood pool contrast agent Angiosense 750 is based (VisEn Medical, Inc., Bedford, MA, USA), as well as polymer-coated gold nanorods (AuNR, OD 50, Ntracker 30-PM-808, Nanopartz Inc., Loveland, CO). In case of the fluorochromes, absorption of the reemitted light, theoretically also contributing to the (optoacoustic) initial pressure distribution, may be neglected because the quantum yield, i.e., the amount of photons reemitted per amount of incident photons, is sufficiently low (order of 10%).

ICG has the advantage of being approved as diagnostic agent for medical use in countries like Germany or the US (approved by the US Food and Drug Administration, FDA). Being typically applied for liver function diagnostics, however, it has a half-life time of only three minutes [63]. Thus, its application for optoacoustic imaging is restricted to real-time imaging. Since experimental durations in this work are significantly longer than the clearance (half-life) time of ICG, this contrast agent is not suited for *in vivo* tumor vasculature imaging. It is, therefore, only investigated marginally for comparative purposes. Angiosense 750, which is based on the herein investigated Alexa Fluor 750, is a blood pool agent, residing in the blood vessels for sufficiently long time. Similar applies to gold nanorods, which only after several hours to days leak out of the blood vasculature to accumulate (cf. Enhanced Permeability and Retention effect EPR) much slower than the duration of the experiment [64]. However, the high laser pulse energies applied herein may cause photobleaching of the fluorochromes and nanoparticles, which I assessed by the following experiment.

A cuvette with diluted contrast agent (initial optical density below OD 3) was positioned in the NIR laser beam of about 4mm spot size (diameter) tuned to the wavelength of the absorption maximum of the respective contrast agent. The volume of diluted contrast agent was 2ml (± 0.5 ml) for ICG and Alexa Fluor and 0.2ml (± 0.05 ml) for AuNR.⁴ For experimental reasons, the nanorods were irradiated at double the pulse energy (32mJ) as compared to Alexa Fluor and ICG (16mJ), which, in case of a non-linear dependence of photobleaching from irradiance, may have an effect. Direct comparison between ICG or Alexa Fluor (Angiosense),

⁴The volumes differed in order to obtain measurable effects within a reasonable amount of time.

and AuNR is, therefore, limitedly valid. The prevailing optical density was measured with a spectrometer (VIS-NIR spectrometer, Ocean Optics) at various time points after the start of the irradiation, and the correspondingly deposited light energy was evaluated. The results are shown in Fig. 5.4.

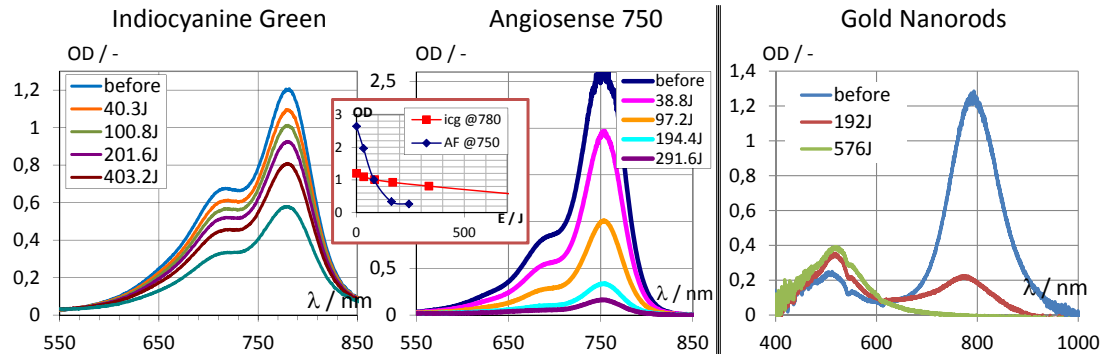


Figure 5.4: Spectra of ICG, AF750, and Gold Nanorods after illumination at peak wavelength in dependence of deposited energy (photobleaching).

The results showed three major effects that needed to be taken into account for optoacoustic imaging experiments. First, neither ICG, not Alexa Fluor were photo-resistant, so that photobleaching is in general not negligible in *ex vivo* or *post mortem* optoacoustic experiments. Second, in view of the sampled volume of the gold nanorods valuing a tenth of the volume of the two dyes, the gold nanorods showed significantly better photo-stability. Nevertheless, the gold nanorods did show significant bleaching in the performed experiment. As the nanorods were bleached, their absorption maximum shifted to smaller wavelengths. Third, ICG showed to be much more photo-stable than Alexa Fluor (Angiosense) 750.

In summary, this experiment points out that for non-real-time optoacoustic imaging, constant renewal of the contrast agents, like provided during *in vivo* experiments, is required. In *post mortem* experiments, Angiosense is used because it generally offers the possibility to visualize the vasculature by inspecting the fluorescence, despite the fact that the dye may bleach. Furthermore, it is noted that herein applied irradiance may be significantly higher than in the tumor tissue during optoacoustic imaging experiments.

5.2 The optoacoustic imaging experiments

Aiming at determining an ideal experimental configuration for *in vivo* optoacoustic whole tumor imaging, I performed three sets of optoacoustic imaging experiments, successively increasing the imaging depth from superficial to profound. The final goal was to provide an experimental arrangement with which the heterogeneous structure of tumors could be resolved with precisions in the range of 30 μ m throughout the entire tumor. By overcoming the limitation of 1 millimeter imaging depth for high resolution imaging of optical contrast, novel biological investigations on cancer development will be enabled. The achieved improvements over the state of the art will be further discussed in chapter 6. Altogether, 9 imaging experiments including optical validation experiments (3 cell lines x 3 experimental arrangements) provide the basis for this section. The most significant experiments and major findings thereof are discussed in this section.

5.2.1 Experimental procedure

Determining the tumor model

A criterion that is important for identifying a suited tumor model is how heterogeneous the tumor structure appears in optoacoustic images, and especially in the validation images obtained by optical and fluorescence imaging methods. Also, the size of the tumor needs to be in a range that is advantageous for biological investigations of tumor vascularisation, and the size needs to be practical for optoacoustic experiments (imaging depths, field of view). Furthermore, the tumor may not be so large as to put unreasonable burden on the animal. Li et al. have shown that tumors like HT29 tumors need to have a diameter of a plurality of millimeters, in order to be well vascularized [25]. The developed optoacoustic systems are best-suited for mesoscopic imaging of tumors up to 10mm in diameter. A compromise that meets all requirements regarding the size of the tumor is about 7-8mm in diameter.

A heterogeneous tumor structure is the main link between optoacoustic images and validation images. Such heterogeneous appearance arises, for example, due to variances in the density of the blood vasculature. If a tumor is (optically) homogeneous, i.e not revealing light absorption variances, it would not be feasible to confirm optoacoustically acquired tumor im-

ages by optical imaging methods. User-influenceable parameters affecting such (optically) heterogeneous appearance are especially the respective tumor cell line, the initial dose of tumor cells, and the final size or the duration of the growth period. However, the variations between the hosts, i.e. the mice, including the implantation variations may have an effect on the growth process and the final heterogeneity. It may, therefore, not be assumed a-priori that same inoculation parameters lead to the same tumor structure. Still, a correlation between the combination of cell line and initial dose, and the heterogeneous appearance of the tumor tissue is expected. The experimental parameters constant for all herein presented optoacoustic imaging experiments are the host and the final size of the tumor, set to approximately 7-8mm in diameter and protruding up to 4mm from the mouse torso. All mice used herein were female CD1 nude mice, weighed 20 to 30 grams, and were approximately six weeks old. Similarity between the hosts by means of weight, age, gender, and race is, therefore, given. The investigated combinations of tumor cell lines and initial dose of tumor cells is summarized in table 5.1.

Cell line	few # cells	medium # cells	high # cells
4T1	10^4	10^5	10^6
Duration	21	12	18
HT29	0.5×10^6	10^6	5×10^6
Duration	28	21	17
A2780	0.5×10^6	10^6	5×10^6
Duration	no tumor	28	22

Table 5.1: Matrix of investigated tumors. Amount of cells inoculated per cell line, and growth duration in days.

The growth process of the A2780 tumor showed to be comparably unpredictable and the tumors spontaneously became necrotic during the growth. Respective trial optoacoustic experiments showed inaccurate results, which is why those tumors are not discussed in further detail herein. Instead, the respective tumors were ranged out for additional proof-of-principle experiments regarding validation methods such as for the development of a micro-CT validation method (cf. section 7.2).

Optoacoustic setup configurations

Two tomographic system configurations were investigated, wherein system configuration I (two sets of experiments, different spot sizes) applied the (state-of-the-art) illumination geometry, i.e. single beam from the top, but allowed for acquiring image stacks, whereas system config-

uration II applied the quasi-static in-plane illumination (see section 4.3.2). The system configurations are shown in Fig. 5.5.

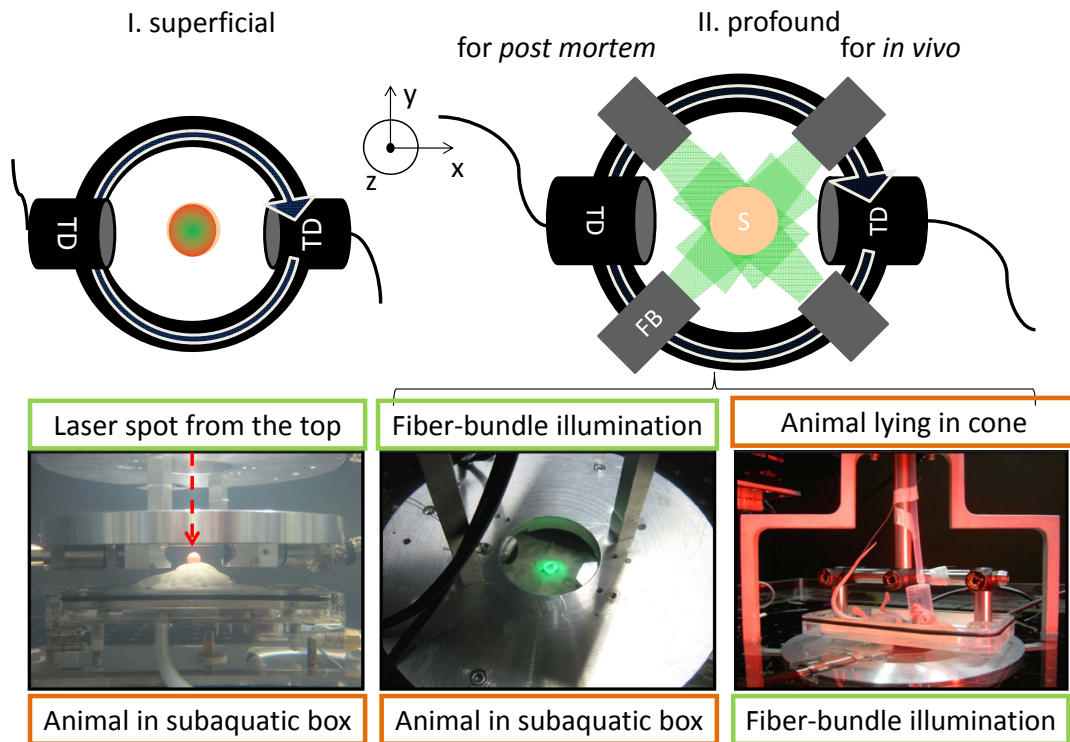


Figure 5.5: Configurations of the optoacoustic system (scanning device) for *post mortem* imaging of tumors. Left (I superficial): The tumor-bearing mouse is hermetically enclosed in a subaquatic box, and the light propagates along the rotation axis of the detection system (transducers (TD)) in negative z-direction. Right (II profound): The tumor-bearing mouse is lying on its back, fixing the tumor by its body weight, and the light propagates anti-radially from the output ferrules of the fiber bundle (FB) towards the tumor.

In the first configuration, the animal was lying on its belly in the under water animal box. Thereby, the tumor protruded into the water. Illumination was provided by a direct single spot from the top, implemented similarly to the description in section 4.3.2, but without the conical lens and such as that the (visible) spot size had the diameter of the tumor (vertically projected). The NIR and 532nm beams propagated along the same path and had the same spot size. The two (conceptually equal) second configurations aimed at maintaining high resolution at higher (mesoscopic) penetration depths. Therefore, the fiber-bundle-based ring illuminator, described in section 4.3.2, was employed, while the mouse fixation was two-fold. In a first experiment, the same mouse holder as for system configuration I was applied. In the second experiment the mouse was positioned on its back, as shown in Fig. 5.5. The tumor was, therein, hanging into the water basin. The animal holder designs are described in section 4.3.1. In system configuration I, the tumors of 10^5 and 10^6 4T1, 10^6 and $5 \cdot 10^6$ HT29, and 10^6 and $5 \cdot 10^6$ A2780

inoculated cells were investigated, and in system configuration II the tumors of 10^4 4T1 and $0.5 \cdot 10^6$ HT29 inoculated cells were investigated.

Optoacoustic imaging procedure

Before the imaging session, a dose of 2nmol Angiosense 750 was injected intravenously (i.v.) through a tail vein of the mouse, and the dose circulated for five minutes before the mouse was euthanized by i.v. injection of a 1:4 Xylazine-Ketamine-Mixture. The animal was then placed in the optoacoustic system with the tumor being oriented with its base (back of the mouse) perpendicular to the z-axis (cf. Fig. 5.1c). The irradiance in this and all other experiments with mice was kept below the respective maximal exposure limit of, for example, $20\text{mJ}/\text{cm}^2$ at 532nm [57]. Scans were performed in the NIR first at various illumination wavelengths, intending to determine the distribution of Angiosense 750. Subsequently, the tumor was imaged at 532nm at the same elevations (as for NIR), to visualize the intrinsic contrast of the blood vessels. Hence, the same vascular structure was viewed from two different perspectives. By imaging at first in the NIR, potential bleaching of the Angiosense during 532nm illumination was avoided. However, the above discussed short half-life times of Alexa Fluor 750 indicate that bleaching effects may still be relevant (see section 5.1.2).

A requirement for the precise localization of the visualized structures was the localization of the tip of the tumor hemisphere, which was performed in the following, redundant manner. First, as a rough estimation, the imaging plane and the tip of the tumor were colocalized with a precision of $\pm 0.5\text{mm}$ by the parallax method. Second, a steep increase in high-passed signal corresponding to the transducer's point spread function -6dB width of $150\mu\text{m}$ was monitored during a ventrally oriented vertical scan. Being significantly less than the precision of the vertical translation stage, this value corresponded to the absolute vertical localization precision. By comparing the optoacoustic images at given depths, we were then able to confirm the true depth below the tip of the tumor. Given the described coordinate system, optoacoustic scans were performed at least at the tip of the tumor, and 1mm, 2mm, 3mm, and 4mm below the tip for relevant wavelengths 532nm, 750nm, 775nm (or 780nm), and 800nm. In cases of special interest, e.g., at levels where the tumor vasculature showed interesting features, further images were acquired at intermediate levels between the mentioned slices. The applied reconstruction and image processing methods are described in chapter 3. The images shown in this chapter

were reconstructed by the backprojection algorithm. Corrections for wavelength-dependent illumination intensity and light-attenuation in the sample were applied.

Validation methods

Before the optoacoustic imaging session, the architecture of the vasculature was visually inspected and photographed, where instructive. After the optoacoustic imaging session, the animal was immediately frozen to -80°C in the same position as imaged optoacoustically. The tumor was then cut out of the mouse and embedded in black OCT-medium (blackened by acrylic paint, to reduce halos due to light scattering), while its orientation was continuously monitored. A graphite mine of 0.7mm diameter (useful for image scale) was positioned to indicate the anterior direction. The tumor was then cryosliced in a setup developed by Sarantopoulos et al. [65] into slices of $20\mu\text{m}$ thickness. Simultaneous color and fluorescence imaging every $100\mu\text{m}$ allowed to acquire optically visible structures and the fluorescence signal of the Angiosense agent. At levels corresponding to those of the optoacoustic images, the sections were picked up on glass plates for immunohistochemistry.

To optically confirm the tumor vasculature, CD31 staining was performed. Thereby, the mentioned relevant sections were processed immunohistologically with Anti-PECAM-1⁵ [CD31] (primary antibody) and Alexa Fluor 594 (secondary antibody) according to the following detailed protocol:

1. Preparing the sections for staining, and drying overnight.
2. Preparing the solutions for sera and antibodies.⁶
3. Fixing the sections in 4°C Acetone for 10min.
4. Placing the sections in 1xTBS for 5min.
5. Marking the regions of the sections with PAP-pen.
6. Blocking by placing the sections in 10GS-TBST at room temperature for 1h.

⁵PECAM-1: Platelet Endothelial Cell Adhesion Molecule 1

⁶TBST: TBS with 0.3% Triton X-100; xGS-TBST: x% Goat Serum in TBST; Primary antibody: CD31, Anti-PECAM-1 (Anti Platelet Endothelial Cell Adhesion Molecule 1) Rabbit Monoclonal. Diluted 1:50 with buffer 1GS-TBST; Secondary antibody: Goat Anti-Rabbit Alexa Fluor 594. Diluted 1:200 with buffer 1GS-TBST

7. Allowing the blocking solution to flow off.
8. Incubating the sections with **primary antibody**, 1GS-TBST for negative control at 4°C in moisture chamber overnight.
9. Placing the sections in TBS three times for 10min.
10. Incubating the sections with **secondary antibody** at room temperature in moisture chamber.
11. Placing the sections in TBS three times for 10min.
12. DAPI-Mounting (coverslip).

For further details regarding the staining method, the reader is referred to the literature [25], [66], [67], [68].

Negative controls were recorded of sections in proximity of said relevant sections. All stained sections of the optoacoustically imaged tumor regions were finally examined under a microscope (DM2500, Leica Microsystems, Wetzlar, Germany) in epifluorescence mode with filter cubes HQ Cherry for Alexa Fluor 594 and A4 for DAPI, and under a macroscope with corresponding filters for illumination and reemission (Z16, Leica Microsystems). Since the histological images represent slice thicknesses well below those of the optoacoustic images (20 μ m vs. >150 μ m), histology provides a microscopic perspective on the structure of the vasculature, which is generally complementary to the optoacoustic mesoscopic perspective. Nevertheless, histology provides information about the general structure and qualitative extent and density of tumor vascularisation, which aids for confirming the optoacoustic images. In order to establish a negative control for the bleaching of the Angiosense agent due to illumination of the tumor during optoacoustic experimentation, an additional HT29 tumor (initial dose 2 million cells) was not imaged optoacoustically, but directly frozen for the cryoslice imaging procedure.

5.2.2 Results

Growth of the tumors

The tumor growth curves (size over time) are illustrated in Fig. 5.6. The graphs show that the growth processes were not linear. Generally, the murine 4T1 tumors grew significantly faster than human cell line tumors. The larger the initial cell dose was, the faster the tumors grew. For comparable initial cell doses (e.g., few cells, see table 5.1), the herein investigated HT29 tumors took more than two to three times as long to grow to a diameter of about 8mm than the 4T1. From Fig. 5.6, it is also deduced that before the tumor appeared to start growing, i.e. protruding from the mouse, an unpredictable period of time had passed (cf. 2mil HT29 curves, of which the tumor cells were inoculated in parallel).

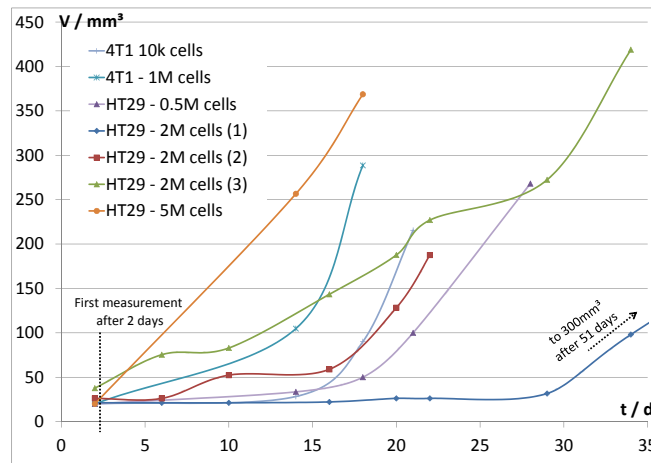


Figure 5.6: Temporal dependencies of tumor sizes during growth processes.

Comparison of the system configurations by means of optoacoustic imaging results

System configuration I. The optoacoustic imaging results obtained for scanning in the geometry referred to as 'I. superficial' in Fig. 5.5 for the tumors with 1 million HT29, 5 million HT29, 100000 4T1, and 1 million 4T1 initially inoculated cells are illustrated in Figs. 5.7, 5.9, 5.8, and 5.10, respectively. First, the results of the 1 million HT29 and the 100000 4T1 tumors will be described.

The reconstructed optoacoustic images point out the problem of imaging deep within the

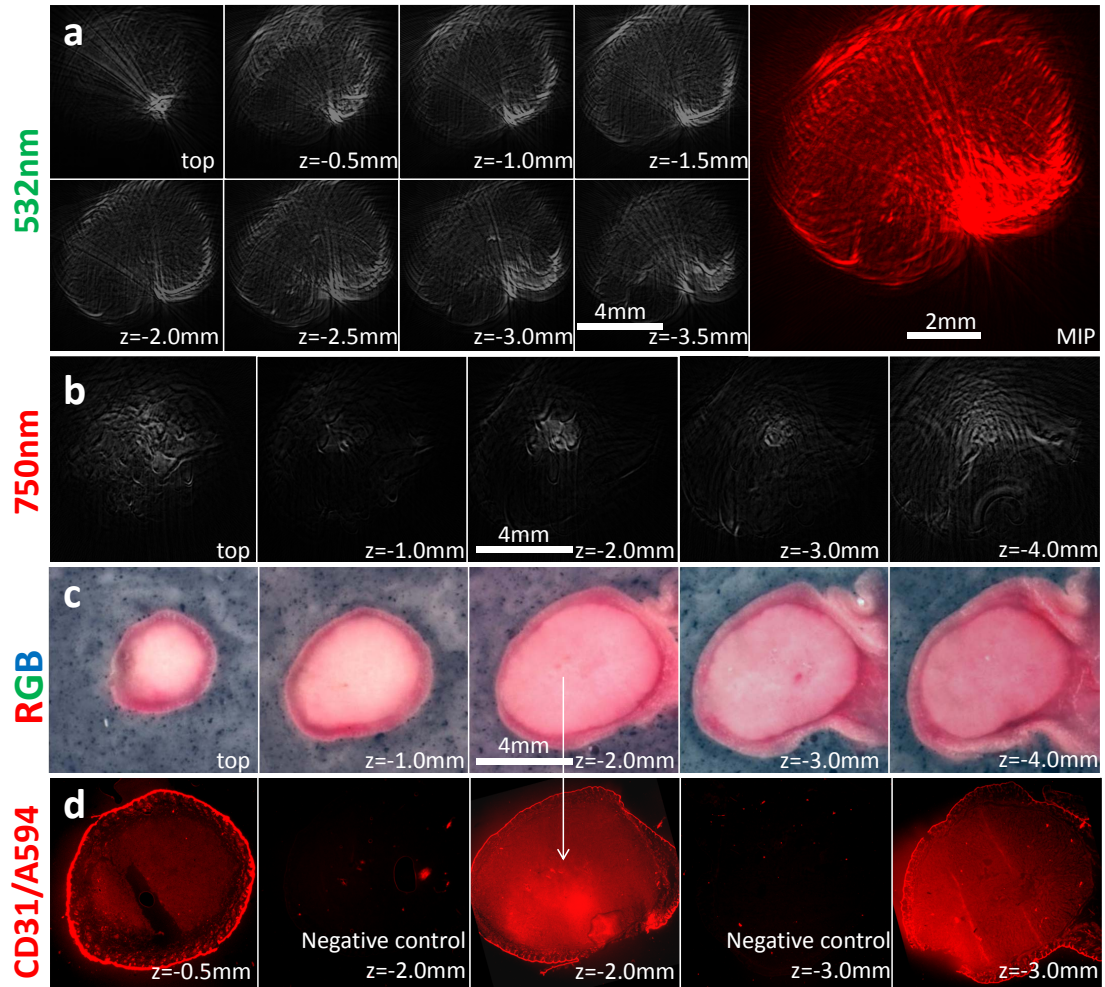


Figure 5.7: Optoacoustic imaging and validation results for HT29 tumor scanned in system configuration I. a: Optoacoustic imaging results for 532nm illumination. b: Optoacoustic imaging results for 750nm illumination. c: Cryoslice color images obtained at the same depths as optoacoustic images. d: Fluorescence macroscopy images of CD31 stained tumors at indicated depths, including negative controls.

tumor while illuminating from the top. The true optical contrast information is overlaid with an interfering pattern due to out-of-plane signal (out-of-plane artifacts). Such artifact patterns were observed similarly for both, HT29 and 4T1 tumors, if scanned in system configuration I (cf. Figs. 5.7a,b and 5.8a,b). Nevertheless, both for green and NIR illumination, basic features of the tumor, such as the outline of the tumor, were revealed by the optoacoustic tomograms. By comparing the optoacoustic images of Figs. 5.7a,b and 5.8a,b with the corresponding cryoslice images (Figs. 5.7c and Figs. 5.8c) and the corresponding CD31 fluorescence images (Figs. 5.7d and Figs. 5.8e), the shape of tumor cross-sections and optical absorption heterogeneities were confirmed. The highly light-absorbing areas in the periphery of the tumor (see Figs. 5.7a) were identified as areas of high blood concentration (well vascularized) in the cryoslice valida-

tion images. In the NIR, a region of high absorption appeared in the center of the tumor. This region equally appeared at 780nm and 800nm, and was, hence, not attributed to the absorbing dye.

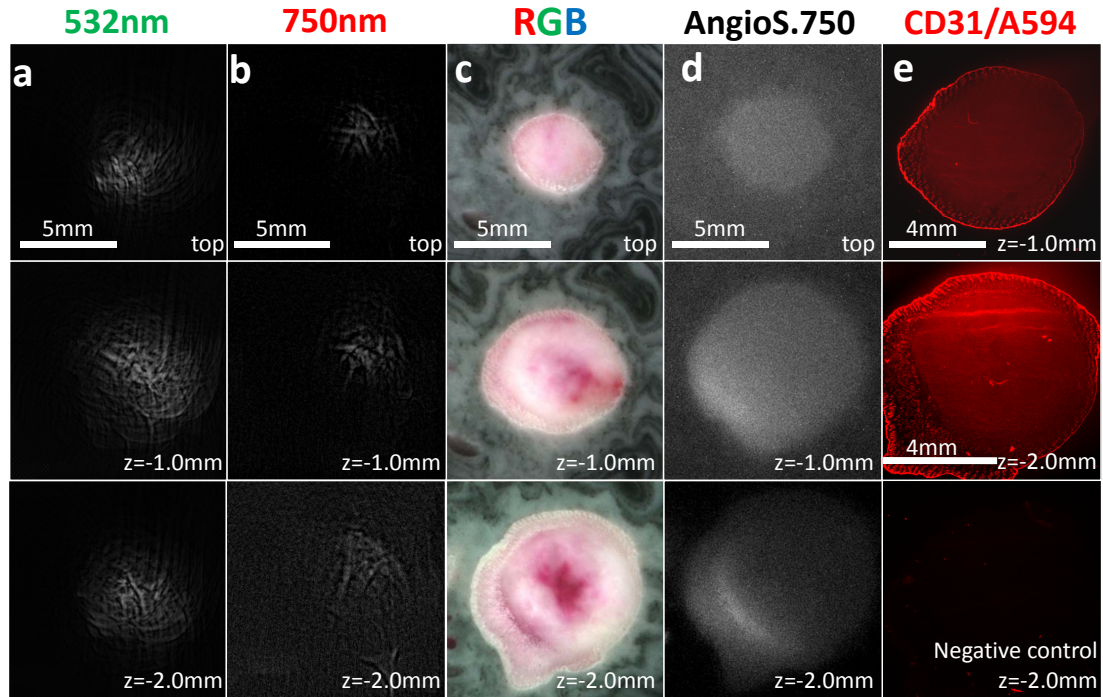


Figure 5.8: Optoacoustic imaging and validation results for 4T1 tumor scanned in system configuration I. a: Optoacoustic imaging results for 532nm illumination. b: Optoacoustic imaging results for 750nm illumination. c: Cryoslice color images obtained at the same depths as optoacoustic images. d: Cryoslice fluorescence images obtained at the same depths as optoacoustic images. e: Fluorescence macroscopy images of CD31 stained tumors at indicated depths, including negative control.

In case of the HT29 tumor, the cryoslice images revealed no (extrinsic) fluorescence, and in the 4T1 tumor not all red areas of the cryoslice color images showed fluorescence. Most probably, bleaching and insufficient or inhomogeneous penetration of the dye into the tumor vasculature was the reason for this (cf. section 5.2.2). The CD31/AF594 stain showed high specificity of the primary antibody, checked by the above described negative controls (see Figs. 5.7d and 5.8e). Further details about the tumor vasculature revealed by the stains will be discussed in the following.

For the 5 million HT29 and the 1 million 4T1 tumors, the illumination spot was unequally wider than the tumor diameter, so that the gradient in light intensity was decreased, providing a more isotropic illumination, and reducing the amount of out-of-plane artifacts in the images. For example, the NIR images of Fig. 5.9 illustrate this effect. At 532nm, however (Fig. 5.9a), out-of-plane artifacts still distorted the optoacoustic images, so that deep parts of

the tumor were not accurately visualized (compare Fig. 5.9a to Figs. 5.9b-d). Even though the cryoslice images did also not show significant fluorescence, distinct structures of high absorption in the optoacoustic images appeared in high contrast. At $z=-4.5\text{mm}$, a major blood vessel showed to split into three smaller vessels (Fig. 5.9b-d). This vascular structure was also revealed in the cryoslices, albeit with less structural details. Since this particular vascular structure did not only appear at 750nm illumination wavelength, but in similar manner also at 800nm, it could not be attributed to the Angiosense dye, exclusively. The continuation of this structure at the adjacently higher levels (e.g., $z=-3.5\text{mm}$ and -2.5mm , 8 o'clock position), however, revealed a contrast profile decreasing towards higher wavelengths, following the absorption profile of Angiosense. Such structure was, therefore, a major blood vessel including the blood pool contrast agent. On the 5 o'clock position, a similar structure showed the same wavelength dependency. Comparison with the respective 532nm image confirmed that strong signals from the top of the tumor outweighed the in-plane signals of the 532nm images. Therefore, the mentioned vessels were not appearing in the respective 532nm images. However, at 532nm, the tumor-superficial microvessels appeared in high contrast, whereas in the respective NIR images just basic larger structures along with some pigment spots, hair, or the like, were revealed.

The cryoslice images of Fig. 5.9 indicate that the optoacoustic images indeed showed structures that were part of the tumor. At 0.5mm below the top of the tumor, already, only a margin of the visualized tissue was skin - most of it was tumor tissue. About 3mm lower, a red patch in the center of the tumor pointed out higher blood concentration. Yet another millimeter lower, this red patch narrowed, before it disappeared at the bottom of the tumor. Due to the tumor fixation during the optoacoustic experiment, the shape of the skin portion shown in the optoacoustic images minimally differed from the one shown in the cryoslice images. However, the solid tumor itself was oriented similarly. The fluorescence cryoslice images in Figs. 5.9f showed no Angiosense fluorescence signal above $z=-3.5\text{mm}$. Deeper within the tumor, the Angiosense signal collocated with certain highly vascularized regions shown in the cryoslices, e.g., towards the 6 and 8 o'clock positions of the tumor, wherein these positions collocated with the positions of the dense vasculature in the optoacoustic images. Furthermore, also the structure at the central regions of the NIR images was revealed in the cryoslice color images, whereby the cryoslice images showed less structural details.

The respective CD31 stains (Fig. 5.9g) showed heterogenic structures, which, according

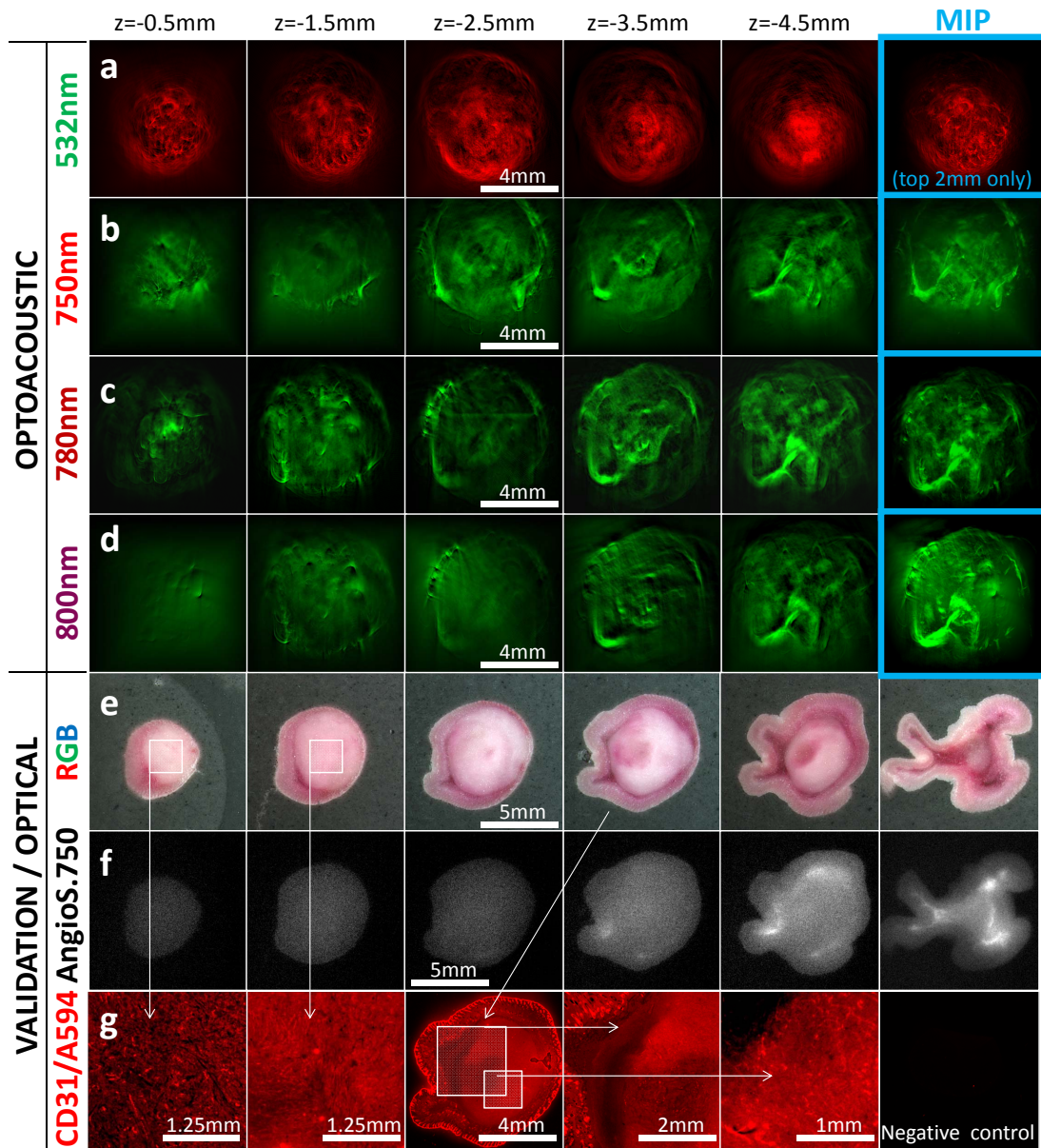


Figure 5.9: Optoacoustic imaging and validation results for HT29 tumor scanned in system configuration I with homogeneous unidirectional illumination. a: Optoacoustic imaging results for 532nm illumination. b-d: Optoacoustic imaging results for 750nm to 800nm illumination. e: Cryoslice color images obtained at the same depths as optoacoustic images. f: Cryoslice fluorescence images obtained at the same depths as optoacoustic images. g: Fluorescence macroscopy images of CD31 stained tumors, field of view as indicated by markers, including negative control.

to the specificity of PECAM-1, represented the tumor blood vasculature (walls). The negative control (NC) image showed that the NC fluorescence signal is negligible at identical image acquisition parameters. Only by acquiring the NC images with multiple orders of magnitude higher exposure times, structures were revealed in the images. However, the structures were generally not the same as those seen in the positive controls. The positive controls, e.g., the zoom tiles in Fig. 5.9g show the finesse of the microvasculature in detail.

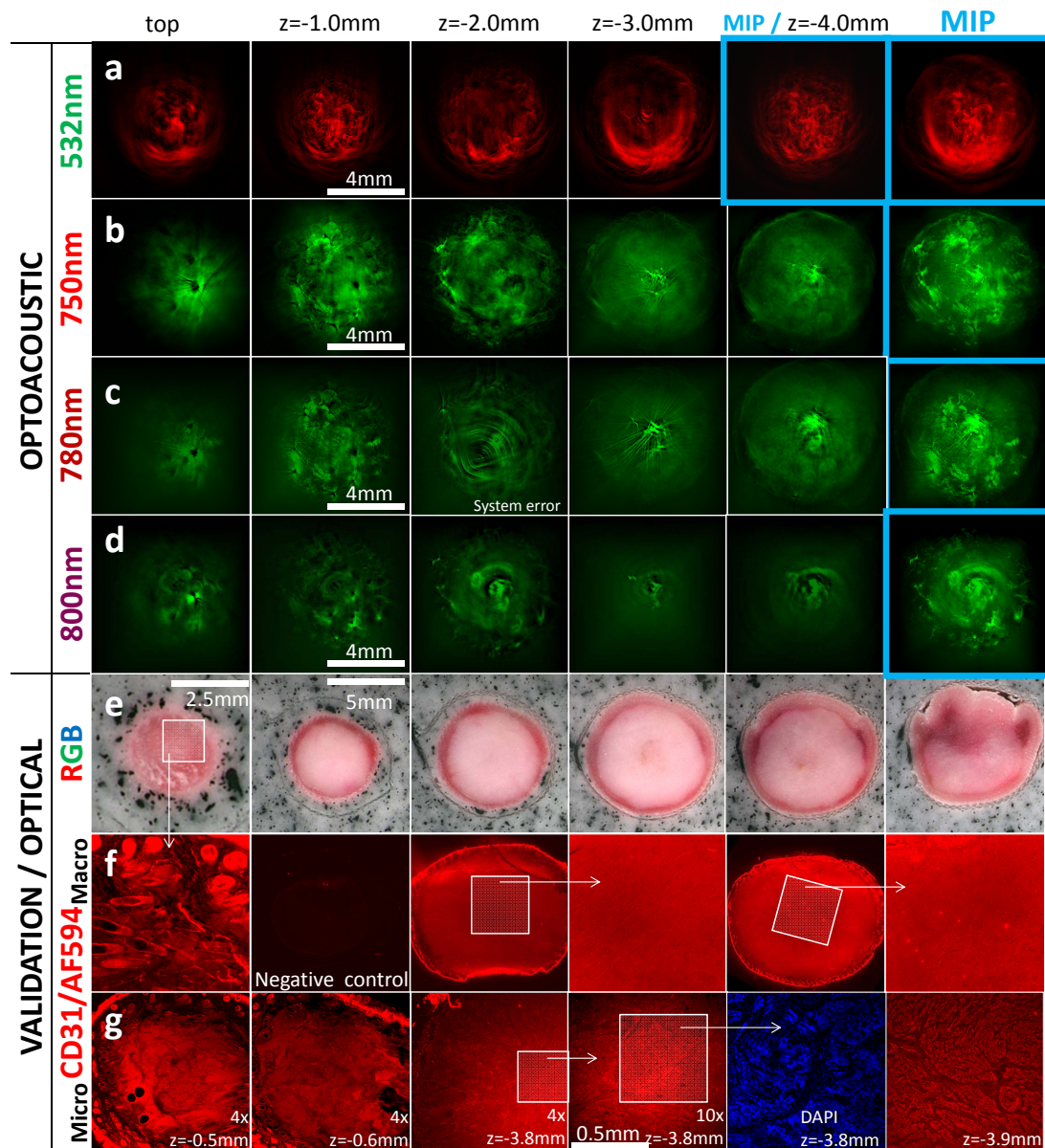


Figure 5.10: Optoacoustic imaging and validation results for 4T1 tumor scanned in system configuration I. a: Optoacoustic imaging results for 532nm illumination. b-d: Optoacoustic imaging results for 750nm to 800nm illumination. e: Cryoslice color images obtained at the same depths as optoacoustic images. f: Fluorescence macroscopy images of CD31 stained tumors, fields of views as indicated on images, including negative control. g: Fluorescence microscopy images of CD31 stained tumors, fields of views as indicated on images.

In contrast to the HT29 CD31 immunohistological images, the stains of the 4T1 tumor showed more homogeneous tumor vasculature architecture (see Figs. 5.10e,f). This corresponded well with the cryoslice images, which indicated dense tumor-surrounding vascularisation and sparse vascularisation within the tumor. Such sparse structures showed to be significantly smaller than 30 microns (cf. Fig. 5.10g, 10x, z=-3.8mm), so that optoacoustic imaging could only visualize the tumor-surrounding vasculature and eventual distribution

of exogenous contrast agents. Herein again, no Angiosense fluorescence signal was detected from the cryoslices. However, the optoacoustic images at $z=-3\text{mm}$ and -4mm , and in particular the central region therein, showed high absorption at 750nm , with decreasing tendency towards 780nm and 800nm . In the respective cryoslice color images, the corresponding images appeared in contrast to the tumor bulk as well, however, not in the same color tone. The 532nm images showed the predicted peripheric vasculature in high resolution. The images are illustrated additionally as a slice stack of the top 4mm of the tumor (Fig. 5.11), further indicating the ring artifacts due to strong out-of-plane signals as reason of the top illumination in combination with the strong absorbing vasculature at the tumor top.

Further describing the fine structure of the tumor as shown by the fluorescence microscopy images in Fig. 5.10g, the DAPI image points out that even though certain structures appeared as void between fluorescing edges (CD31 binding to endothelium of blood vessels, see above), they in fact were not void, but contained cell cores indicated by the blue dots in the image, and making them additionally eligible for being blood vessels.

System configurations II. To avoid the ring artifacts discussed above, especially for illumination at wavelengths in the visible range, quasi-static ring illumination was applied. As described in section 4.3.2, even though the fiber bundle outputs on the specimen side were rotated about the specimen, the in-plane initial pressure distribution was in best approximation projection-independent.

As illustrated in Figs. 5.12a-d and 5.13a-d, the occurrence of ring artifacts was well reduced compared to the case of top illumination, especially at 532nm illumination (cf. Fig. 5.11). Referring to Fig. 5.12, the general appearance of the cryoslice cross-sections (row e) allowed to confirm the structures shown in the optoacoustic images. One exemplary structure for this comparison was the strongly absorbing periphery of the tumor, showing as a highly vascularized ring, which, at lower levels, also revealed strong Angiosense fluorescence signal. Furthermore, the left image of Fig. 5.12e shows that a blood vessel bifurcated slightly deeper than 0.5mm , which is illustrated in detail in the NIR optoacoustic images. The NIR optoacoustic images further describe the three-dimensional architecture of these vessels. In particular, from the images at $z=-1.5\text{mm}$ and $z=-2.5\text{mm}$, the elevational orientation of the bifurcating blood vessel was determined. For example, from the lower left of the tumor, a major blood vessel partly encircled the tumor clockwise upwards. Vascular structures that were oriented

anti-radially, i.e., towards the tumor center, were clearly distinguishable, e.g., in the NIR images at lower levels. Similar vasculature architectures have been demonstrated in the literature, albeit using invasive and/or radiologic imaging methods [28], [25], [69].

Overall, the CD31 images pointed out that the blood vessels in the HT29 tumors were more heterogeneously distributed than those of the 4T1 tumors (cf. Figs. 5.7 to 5.13). Zooming in on the CD31 fluorescence images with magnifications of 10x and more, randomly oriented tumor vasculature was revealed. The structure of the shown blood vessels stood in accordance with the structure presented in the literature (cf. [69]).

The optoacoustic images acquired in system configuration II (Figs. 5.12 and in particular Figs. 5.13) illustrated the high accuracy of the imaging method as compared to the ground truth images obtained by cryoslice imaging. The cryoslice fluorescence images (Figs. 5.13f) showed no fluorescence signal of Angiosense, which corresponded well to the information obtained by the NIR optoacoustic images (no wavelength dependency). In particular, the highly vascularized peripheric left half circle half-way surrounding the tumor (Figs. 5.13b), as well as the internal structures, were represented in the cryoslice images (Figs. 5.13e) in similar manner. Also, the correspondence between the NIR and 532nm imaging results was higher than in the other experiments. Imaging with 532nm illumination, in particular, showed the microvasculature of the top 1mm to 2mm with higher accuracy than common optoacoustic state-of-the-art systems (see MIP in row a).

Fluorescence Cryoslice Imaging - Bleaching of Angiosense

Further enforcing the discussion of section 5.1.2, herein a comparison of fluorescence cryoslice images is made to further investigate why the absorption-characteristics of Angiosense were not observable in the optoacoustic and cryoslice imaging results. Therefore, a control HT29 tumor that was not exposed to laser light was cryosliced by the same procedure as described above (Fig. 5.14c). This tile c is to be compared to tile b, which corresponds to a fluorescence cryoslice image of the tumor of Fig. 5.12, wherein both were acquired with the same systematic acquisition parameters (gain, exposure time). The fluorescence cryoslice images of tiles a and b were acquired after optoacoustic imaging, hence, illuminated for more than three hours at various wavelengths, including the peak absorption wavelength of Angiosense750. Tile

a shows the tumor of tile b but acquired with five times longer exposure time, essentially revealing just intrinsic fluorescence of the tumor tissue, but no Angiosense fluorescence signal.

5.2.3 Discussion and conclusion

System configuration for *in vivo* imaging. Optoacoustic tomography with illumination from the top had shown in planar, 2D imaging experiments to have the potential for visualization of tumor-superficial, subcutaneous vasculature [34]. Therein, investigating the tumor in three dimensions had not been possible, as the tumor had been flattened by the hydrostatic water pressure acting upon it. However, in the experiments presented herein, the tumor was not flattened, but remained sphere-like during the imaging procedure. When imaging such unflattened tumor in the experimental configuration described above, i.e. with a transducer tightly focused in elevation (PNDT V319) and illumination directed vertically onto the tumor, the large initial pressure distribution gradient in z-direction showed to cause strong out-of-imaging-plane signals distorting the optoacoustic tomograms. The distortions took the shape of rings and bows, i.a., in the results illustrated in Fig. 5.7.⁷

By increasing the beam diameter, hence, reducing the initial pressure distribution gradient in z- (and x- and y-) direction, the amount of out-of-plane artifacts was significantly reduced for NIR illumination, but insufficiently reduced for 532nm illumination (see Figs. 5.9, 5.9, and 5.11). Accurate optoacoustic images of the tumor heterogeneity were finally obtained in system configuration II, which was based on in-plane quasi-static illumination of the sample. Thereby, superficial / subcutaneous microvasculature as well as profound microvasculature within the tumor was revealed, and confirmed by cryoslice imaging and immunohistological methods. In summary, optoacoustic tomography with NIR illumination provided insights on intra-tumoral features, such as bifurcating blood vessels in the center of the tumor (see Fig. 5.12), which were not equally obtained by any of the other applied invasive imaging methods. On the other hand, optoacoustic tomography with 532nm illumination indicated to be advantageous for intrinsic contrast superficial imaging, which will be further evaluated and discussed in chapter 6.

⁷Out-of-plane artifacts appear as circular structures, because true distance between a structure and the transducer is for every projection larger than it would be, if it was located within the imaging plane.

In conclusion, system configuration II is expected to be better suited for *in vivo* imaging of tumor vasculature than system configuration I. Even though NIR illumination from the top of the tumor showed reasonable imaging results, if the laser beam was sufficiently expanded to well exceed the tumor diameter, the vasculature could not be accurately visualized with intrinsic contrast at 532nm illumination. To receive a quick impression of the peripheral tumor vasculature, however, such intrinsic contrast imaging is valuable. The fiber-bundle-based ring illuminator colocates the planes of maximal light intensity and of maximal detection sensitivity, allowing to acquire such intrinsic contrast images without the described out-of-plane artifacts. Constant in-plane illumination is generally difficult to implement, as the transducer shall rotate about the specimen, inherently blocking a portion of the illumination. The fiber-bundle-based ring illuminator avoids this problem by delivering the light through fiber bundles whose output ferrules also rotate about the sample. By placing the output ferrules up to 25mm close to the sample, the light absorption along the (short) water path is reduced synergistically.

Tumor model for *in vivo* imaging. Different tumors showed different appearances in the cryoslice color and fluorescence images, as well as in the immunohistological images. The differences in tumor blood vessel structures between the different cell lines, as described in the CD31 immunohistochemical investigations, may correlate to the growth process of the different tumor types. One probable cause for this, which, however, would require further biological confirmation, is that the slower growth process allows the vasculature to grow slower, evolve better and become larger. In summary, the HT29 showed larger heterogeneous structures (cf. Fig. 5.9), which, consequently, are expected to be more accurately resolvable by optoacoustics. In particular, the larger, rougher architecture of the vasculature of HT29 tumors would be better imageable by optoacoustic tomography than the vasculature of 4T1 tumors. Therefore, HT29 is regarded as the best-suited tumor model for (*in vivo*) investigations presented in the next chapter.

All amounts of initial cell doses led to well vascularized HT29 tumors, whereby tumors of larger initial doses (1-5 mil. HT29 tumor cells) showed also the macroscopic heterogeneity of interest. From an animal health point of view, those tumors showed to sufficiently little influence the animal's physical parameters, such as weight. 2 million cells are, therefore, regarded to be a suitable initial dose for the further *in vivo* investigations.

Contrast agents and validation methods for *in vivo* imaging. The validation by above described optical macro-/microscopy methods revealed the fine structure of the tumor vascularisation, in particular, the differences between the HT29 and 4T1 tumors. Thereby, the employed validation methods visualized up to 20 microns thin tissue slices microscopically. In optoacoustic tomography, however, much thicker slices (herein: more than 150 microns at high resolution (fine structure), more than 500 microns at low-resolution (rough structure)) were illustrated in the images. Therefore, optoacoustics provided a mesoscopic view on the microvasculature. Nevertheless, the general distribution and density of blood vessels in tumors were determinable by both, optoacoustics and optical macro-/microscopy. Yet, as the employed optical macro-/microscopy methods rather provided a view on the tumor vasculature that was complementary to optoacoustics, another validation method for investigating the whole tumor mesoscopically would be highly advantageous. In section 7.2, an approach for lifting such a validation gap is discussed.

As to the immunohistological investigations, the negative controls indicated high specificity of the stains for both tumor types, so that it was certain that all CD31 images show the vascular structures. For *post mortem* experimentation, such immunohistological approach for validating the presence and density of the vasculature was indispensable. The major disadvantage of immunohistology, however, was that each tissue section needed to be processed separately, requiring a very large amount of extra work and high costs. If the animal was still alive after the optoacoustic imaging session, as it would be the case for *in vivo* imaging, it would be, hence, preferable to inject a fluorescent dye into the vasculature of the mouse for the dye to distribute throughout the tumor vasculature. Such approach is further discussed in the next chapter.

As described, e.g., in section 5.2.2, the high irradiance by the laser bleached the Alexa Fluor-based Angiosense dye in the tumor vasculature. In *post mortem* experiments, where the dye within the tumor is not renewed by blood circulation, the optoacoustic signal from the dye is not only wavelength-dependent, but also (typically exponentially) decreasing with time. In consequence, multi-spectral decomposition could not be performed reliably. In *in vivo* experimentation, however, it is assumed that the resubstitution of the dye into the tumor occurs on a much shorter time scale than the bleaching and that the blood volume in the mouse is much larger than the amount of blood that is exposed to the laser light, so that the effect of bleaching would be minimized. Furthermore, gold nanorods showed to be more photo-

stable than the blood-pool contrast agent Angiosense, and to have sufficiently long clearance times from the vascular system of the mouse (compared to ICG). Therefore, gold nanorods are chosen for enhancing the signal and contrast of the (tumor) blood vessels over the background in case of NIR illumination. Another potential disadvantage of *post mortem* imaging over *in vivo* imaging, is based on the process of vasoconstriction, whereby the lumen of the blood vessels is significantly reduced, leading to the pale appearance of tissue after death. Although fixation of the tumor by a latex membrane helped to reduce this effect in the described *post mortem* experiments, placing the mouse with the tumor hanging down and / or imaging *in vivo* is expected to result in images with higher vessel contrast.

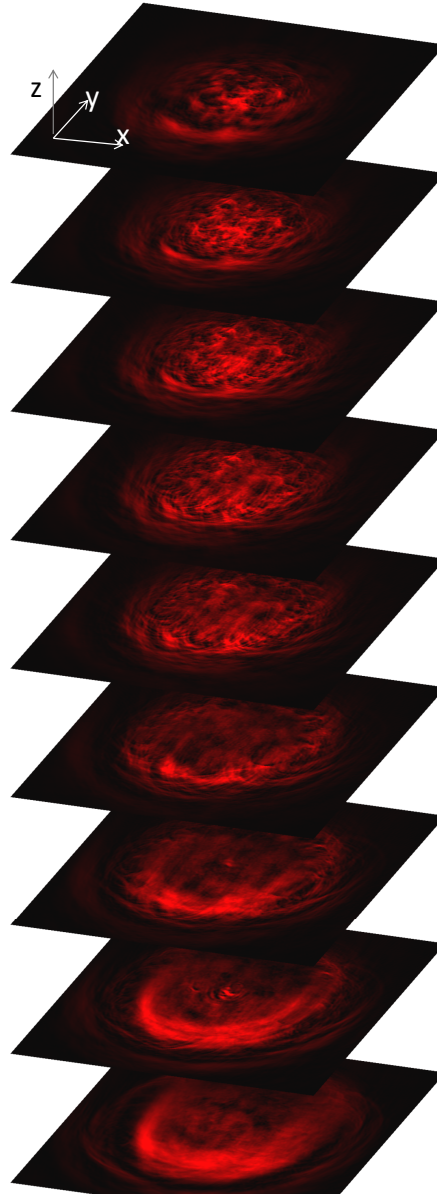


Figure 5.11: Optoacoustic tomography stack of the entire 4T1 tumor (up to 4mm below the top of the tumor) scanned in system configuration I with 532nm illumination.

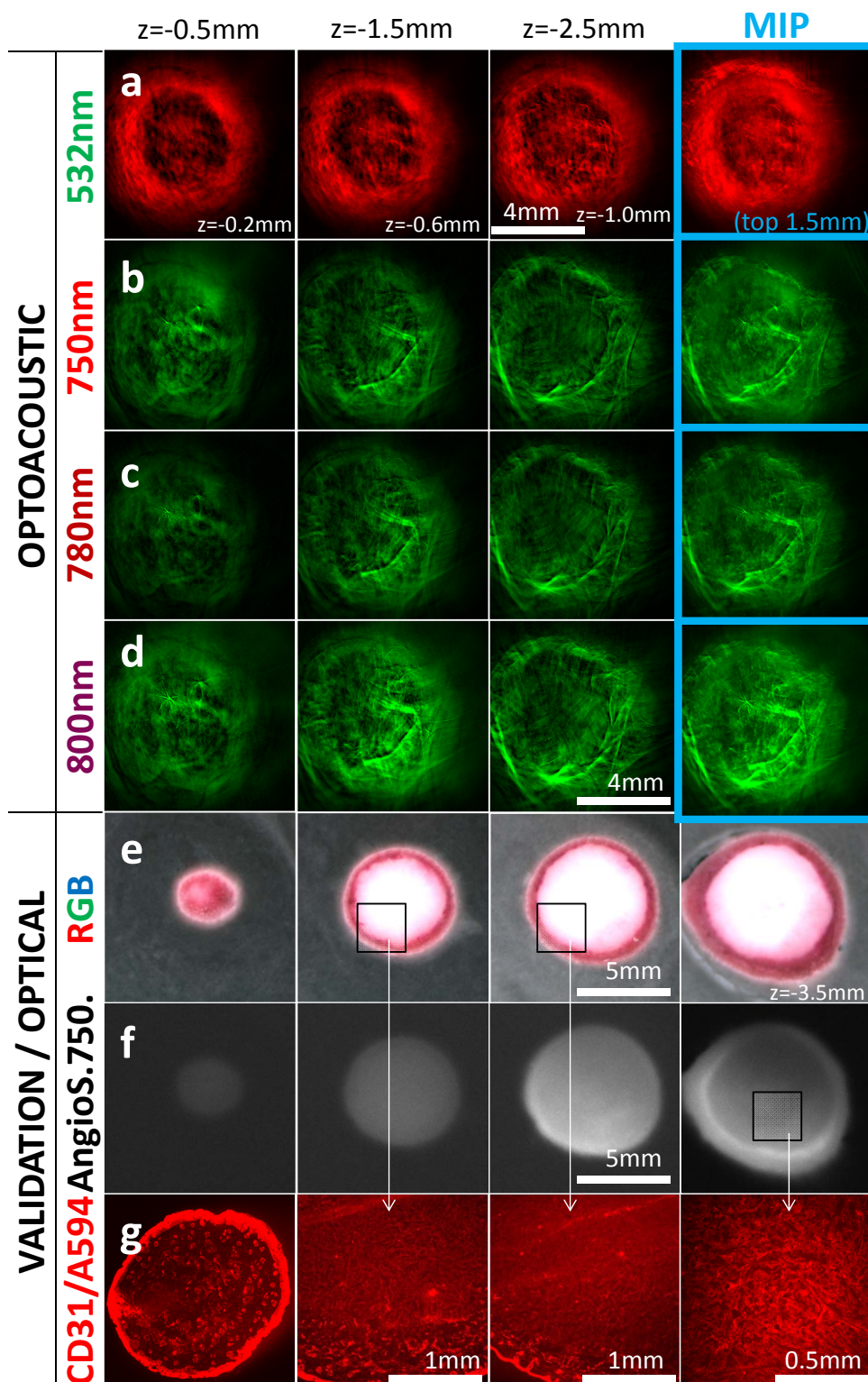


Figure 5.12: Optoacoustic imaging and validation results for HT29 tumor scanned in system configuration II. a: Optoacoustic imaging results for 532nm illumination. b-d: Optoacoustic imaging results for 750nm to 800nm illumination. e: Cryoslice color images obtained at the same depths as optoacoustic images. f: Cryoslice fluorescence images obtained at the same depths as optoacoustic images. g: Fluorescence microscopy images of CD31 stained tumors.

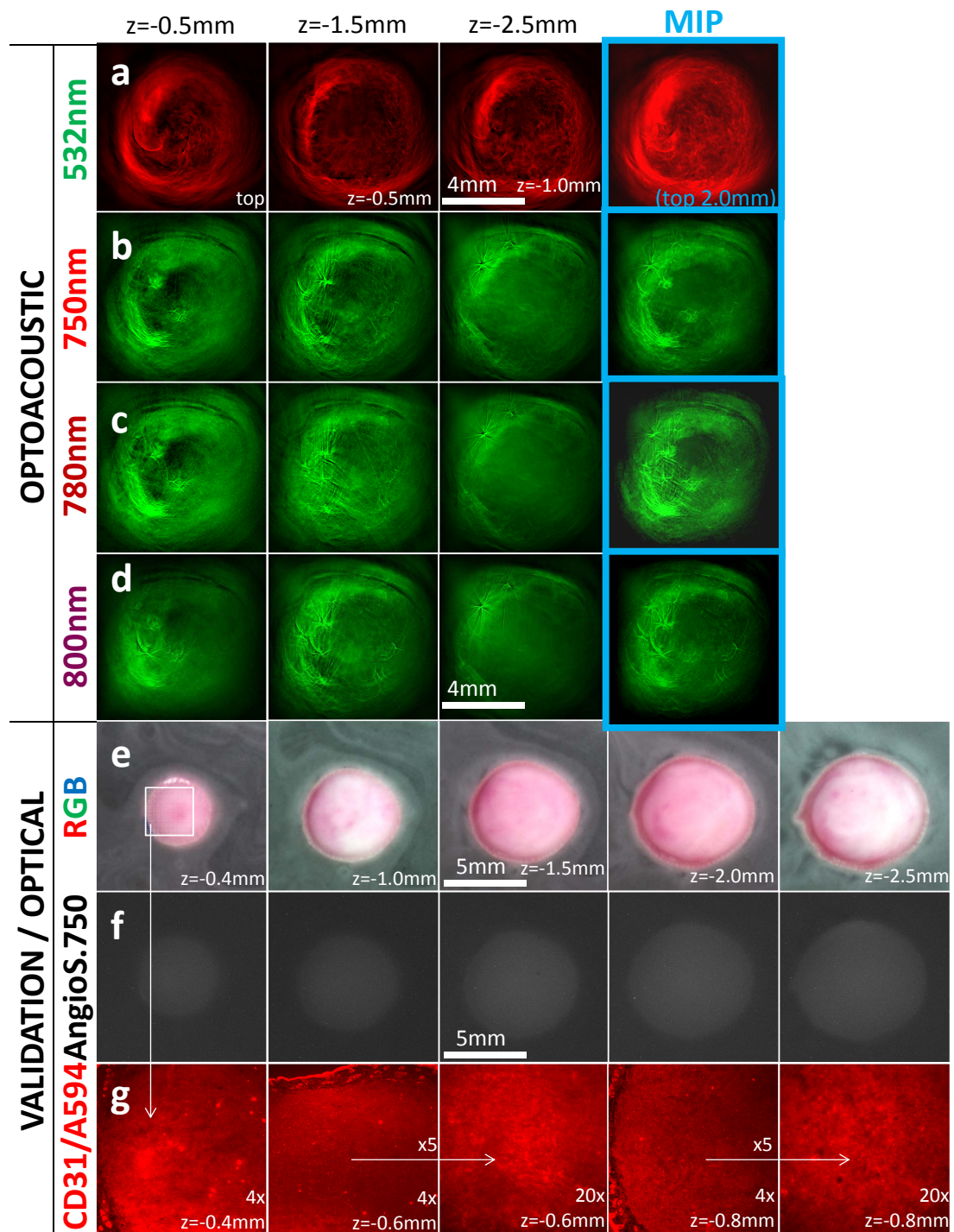


Figure 5.13: Optoacoustic imaging and validation results for 4T1 tumor scanned in system configuration II. a: Optoacoustic imaging results for 532nm illumination. b-d: Optoacoustic imaging results for 750nm to 800nm illumination. e: Cryoslice color images obtained at the same depths as optoacoustic images. f: Cryoslice fluorescence images obtained at the same depths as optoacoustic images. g: Fluorescence microscopy images of CD31 stained tumors, fields of views as indicated on images.

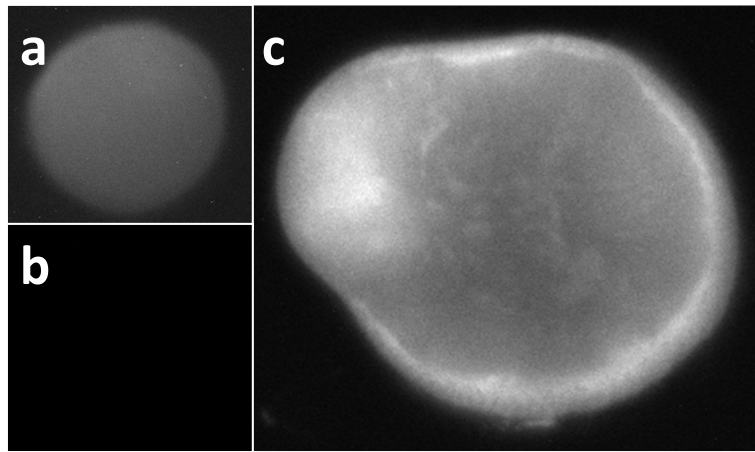


Figure 5.14: Fluorescence cryoslice images showing the photobleaching of the contrast agent Angiosense750 in the tumor. a: HT29 tumor after optoacoustic imaging session. b: The tumor of (a) acquired with five times shorter exposure time. c: Control HT29 tumor not exposed to laser light, acquired with the same parameters as (b).

Chapter 6

Optoacoustic imaging of tumor vasculature with natural and exogenous contrast agents, *in vivo*

This chapter discusses *in vivo* imaging of subcutaneous mouse tumors, which represents the major target subject of this thesis. The findings of the previous chapters provide the basis for the experiments presented herein, and for the interpretation of the results.

For centuries, cancer research has been shaped around the technical limitations of optical imaging [24]. Tumors have been sliced to 10 micron thin slices in order to be visualized. Alternatively, glass windows have been added to them *in vivo* to get intra-vital insights from their first few tens of microns [70] [28] [29]. To improve upon the challenges of optical microscopy, several radiological methods have been also employed for experimental cancer imaging. X-ray imaging has been employed to image tumor anatomy and vascularisation [71] MRI typically reveals many anatomical and functional features [72] [73] [74] [75], whereby nuclear imaging customarily reveals the distribution of a selected molecule, albeit with low resolution [76]. Yet, the attractiveness and versatility of optical contrast continues to drive the development of optical imaging for cancer research. Macroscopic fluorescence and bioluminescence imaging became popular in the last decade, as they can dynamically reveal information on cellular and subcellular disease characteristics [77]. Despite the popularity, macroscopic optical imaging

lacks the resolution to offer a detailed view of experimental tumors [24].

Optoacoustic imaging brings significant new performance in the imaging sciences. It comes with the advantages of spectrally visualizing optical contrast, allowing imaging of various intrinsic and extrinsic photo-absorbing molecules at ultrasonic resolution. By breaking through the fundamental limitation of macroscopic optical imaging, i.e., the resolution drop due to photon scattering, multispectral optoacoustic tomography (MSOT) in particular has been shown capable of visualizing blood vessels, tissue oxygenation and different photo-absorbing molecules and nanoparticles *in vivo*. Based on a tomographic setting with a fixed detector array, fast multispectral imaging has enabled the visualization of kinetic processes *in vivo* using optically labeled agents [78], underlining another important strength of this emerging modality.

High resolution optical imaging throughout experimental tumors could enable better understanding of the heterogeneous patterns of tumor growth and the spatial dependencies of tissue biomarkers or drugs. Optoacoustic imaging of cancer has been performed using optoacoustic microscopy [79] [56] employing raster scanning approaches. When a focused laser beam is scanned, optical-resolution optoacoustic imaging can be achieved, albeit at penetration depths that are similar to optical microscopy. Similarly, raster scanning of focused ultrasonic transducers has been considered for achieving higher penetration ability than the optical focusing approach. However, despite the superior penetration depth, acoustic focusing has not allowed accurate imaging of cancer at penetrations larger than 1-2 millimeters [56], which limited imaging to very thin, early stage carcinomas. Optoacoustic tomography on the other hand has been applied to two-dimensionally image progression of subcutaneous vasculature in the early stage of tumor growth, but no depth information about the heterogeneity in the tumor mass could yet be demonstrated. Instead, the vasculature lying 400 μm below the skin surface was investigated, a depth commonly attributed to the subcutis instead of the tumor mass [34]. Tomographic implementations of multi-spectral optoacoustic tomography in the mesoscopic regime, i.e. the 0.5 - 10 mm range, have recently shown the ability to image gene expression patterns through entire zebrafish and the drosophila pupa [80]. Optoacoustic mesoscopy could also offer new insights into cancer investigations.

Using interferometric optoacoustic scanning, tumor vasculature was recently imaged at 600nm, achieving lateral spatial resolutions in the range of 70 to 100 microns when imaging through up to 10mm of tissue. Most biological processes of angiogenesis, though, occur

on a smaller scale in the range of 30 microns and below. For this reason, we investigated herein volumetric optoacoustic tomography for three dimensional mesoscopy of optical contrast throughout entire solid experimental tumors at higher resolution. We examined whether structural and functional tumor features could be visualized through entire tumors, including studying the biodistribution of externally administered gold nanoparticles. We showcase spectral cancer imaging with features that reveal never before seen functional optical signals from within tumors, pointing to mesoscopic MSOT as a potent method for biological imaging in cancer research and potentially clinical applications.

6.1 Experimental procedure

The components of the experimental setup developed for *in vivo* mesoscopic imaging are described in detail in chapter 4, and further details regarding the relevant scanning and image reconstruction methods are provided in chapter 3. The setup is configured as described in section 5.2.1 as system configuration II, illustrated in Figs. 5.5 (bottom right) and 4.11.

6.1.1 Experimental arrangement

In summary, nanosecond-pulsed illumination was provided at 532nm and in the 700 to 900nm range using a tunable Optical Parametric Oscillator (OPO) laser. Light delivery to the specimen was provided via a quartz fiber bundle (CeramOptic Industries, Inc., East Longmeadow, MA, USA) consisting of 260 fibers bundled to 4 arms, where fiber positions in the bundle were randomized to reduce light flux variations. The arms were aligned around the object separated by an angle of 90 degrees and terminated by output ferrules (OF) in a way that the sample is homogeneously illuminated. The cylindrically focused PZT transducer (V319, Panametrics-NDT, Waltham, MA, USA) was positioned with its focal line at the same level as the illumination plane as shown in Fig. 4.11. Its element diameter, focal length, nominal central frequency and bandwidth are 13mm, 19mm, 15.28 MHz and 47.85% respectively. Acoustic signals were recorded at a sampling frequency of 100MHz with 14-bit resolution using a Labview controlled digital acquisition card (Octopus, GaGe Applied Technologies, Lockport, IL, USA). The illumination and detection system was mounted on an aluminum ring (tomographic scan ring) which could be rotated with respect to its cylindrical axis by a rotation stage (PRM1-Z7, Thor-

labs GmbH, Dachau, Germany) to enable a tomographic view of the sample at quasi-static illumination, hence, initial pressure distribution. In order to scan at different elevations, the described tomographic scan ring (i.e., fiber-bundle-based ring illuminator) was translated in elevation by a linear stage (NRT 100/M, Thorlabs GmbH, Dachau, Germany). To allow for good acoustic coupling, the scan ring was submerged in a water tank, where a constant temperature of 36°C was maintained. The animal holder was a self-made polystyrol cone (basis angle 25°) pointing downwards (Fig. 4.11).

6.1.2 Image reconstruction

Tomographic image reconstruction was performed for an area of 10 by 10 millimeters using a conventional backprojection algorithm and a pixel size of 13.3 microns. After the reconstruction, images were corrected for light attenuation by multiplication with a two-dimensional modified Bessel function of the first kind [42]. In order to evaluate the spatial distribution of absorber molecules such as oxygenated hemoglobin (HbO₂) and deoxygenated hemoglobin (Hb), various spectral decomposition algorithms were applied [46]. Assuming that the absorption spectrum of the biomolecules of interest is a-priori known in the imaged sample, images acquired at multiple excitation wavelengths were decomposed by guided independent component analysis (ICA). Guided ICA separates absorbers in multi-spectral data by identifying statistically independent absorption properties, using the a-priori expected absorption spectra as an initial guess [46]. In order to obtain a quality measure of the reconstructed images, we calculated the two-dimensional standard deviation σ as a measure of contrast achieved in the images, i.e.,

$$\sigma = \sqrt{Var} = \sqrt{\frac{1}{n \cdot m} \sum_{i=1}^{n \cdot m} (x_i - \bar{x})^2}. \quad (6.1)$$

Herein, Var is the Variance, n and m are the number of pixels along the two image dimensions and x_i the pixel intensities. In our experiments, the noise level is a wavelength independent scaling factor, given by the acquisition hardware. We could, thus, directly compare the contrast of the resulting images using σ instead of explicitly calculating the contrast to noise ratios.

6.1.3 Animals and imaging

2 million HT29 human colorectal cancer cells (ATCC-HTB-38, ATCC Manassas, VA, USA) were subcutaneously inoculated into the back of 25g female CD1 nude mouse (Charles River Laboratories, Sulzfeld, Germany). The tumor was allowed to grow to approximately 8mm in diameter. For imaging, animals were anesthetized with a 1.5 vol-% isoflurane-oxygen gas mix. A 20cm long intravenous catheter (PE-10/100, Warner Instruments, Hamden, CT) was subsequently positioned in the lateral tail vein. The animal was then placed in the optoacoustic setup with the tumor surrounded by the optoacoustic setup and surrounded by water. The transducers and light sources were then rotated by 360° around the object. Imaging was performed at 532nm illumination to exploit the high intrinsic contrast from the blood vessels for evaluation of the general orientation and internal anatomy of superficial tumor features. To penetrate the entire tumor, illumination was then switched to the NIR. All images acquired with NIR illumination required corrections for the depth-dependent and wavelength-dependent variations in light fluence within the tumor. To track the distribution of nanoparticles into the tumor microvasculature, different tumor slices were acquired at four distances from the top of the tumor (i.e. 0.4mm, 1.5mm, 2.3mm and 3.8mm) at 750nm, 800nm, and 850nm. Subsequently, a dose of 50 μ l total volume (molar concentration: 49 nM) of long-circulating polymer coated gold nanorods (AuNR) (OD 50, Ntracker 30-PM-808, Nanopartz Inc., Loveland, CO, absorption maximum at 800nm, 80% line width 75nm) was slowly injected (duration: 20 seconds) through the catheter, and the catheter was rinsed with isotonic sodium chloride solution. The effect of the contrast agent perfusion was monitored continuously at 800nm illumination wavelength in an imaging plane that was located approximately 1.5mm below the top of the tumor hemisphere. Thirty minutes past the injection, when the circulation of gold nanorods (AuNR) was expected to have reached steady state, the acquisitions at the four slice positions were repeated at the following wavelengths: 800nm, 850nm and 900nm. At all times, the illumination intensity was kept below the respective wavelength dependent maximum permissible exposure values, which was, for example, 20mJ/cm² at 532nm [57]. Under the assumption that contrast-affecting biological processes were much slower than the dynamics of gold nanorod circulation, the gold nanorod distribution within the tumor region could be determined by two independent methods. The simplest approach was to visualize the difference in pixel intensities before and after the injection. Therefore, differential images at 800nm were obtained. Alternatively, spectral matching of the absorption spectrum of the nanorods at 800, 850 and 900nm

allowed differentiation of the rods without considering background (baseline) measurements.

6.1.4 Validation studies

The animal and tumor were photographed *in vivo*. After imaging and right before the administration of a lethal injection of anesthetic, a dose of 100 μ l of tomato-lectin (TEXAS RED® LYCOPERSICON ESCULENTUM, Vector Laboratories, Burlingame, CA, USA) was injected intravenously through the catheter into the tail vein of the mouse in order to highlight vasculature in the tumor area in validation *ex vivo* studies. Immediately after euthanasia, the mouse was frozen at -80°C, caring to preserve the position that the animal assumed during *in vivo* imaging. Frozen mice were imaged by color and fluorescence cryoslice imaging in the imaging cryoslicer system described in Ref. [65] to reveal the signal of the injected agent. The procedure consisted of automatically slicing through the mouse using a cryoslicing unit (CM 1950, Leica Microsystems GmbH, Wetzlar, Germany) retrofitted with a multi-spectral camera that collects color and fluorescence images from each consecutive slice, thus, reconstructing the anatomy and the distribution of fluorescent agents in three dimensions throughout the tissue cryosliced. For lectin measurements, white light was passed through a single-band bandpass filter at 562/40 nm (FF01-562/40-25, Semrock, Inc., Rochester, NY, USA), and images were obtained every 100 microns. 20 μ m thick slices were also collected on glass slides and examined under a microscope (DM2500, Leica Microsystems, Wetzlar, Germany) in epifluorescence mode with filter cube HQ Cherry. Selected slices were stained with Hematoxylin and Eosin and inspected in the same microscope in white light transmission mode.

6.2 Results

6.2.1 Intrinsic contrast imaging of superficial microvasculature

Images acquired with illumination at 523nm reveal high intrinsic contrast of the superficial vasculature in the tumor region, as shown in Fig. 6.1 by maximum intensity projections (Figs. 6.1a-c) and by a tomographic slice stack (Fig. 6.1g). The images reveal a vascular network much deeper than the one shown by previous planar optoacoustic implementations, owing to

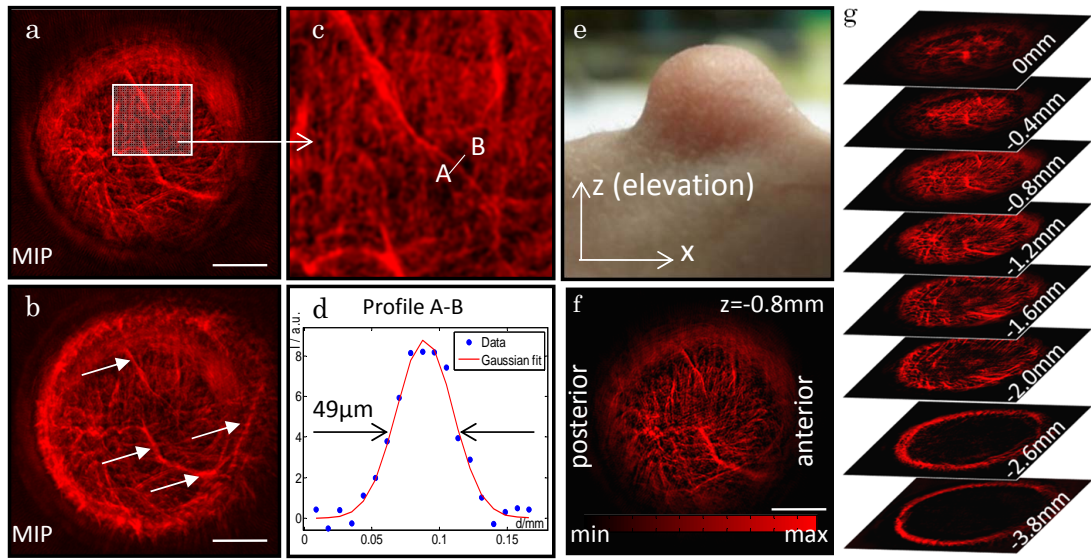


Figure 6.1: Intrinsic contrast optoacoustic imaging of tumor vascularisation. a: Maximum intensity projection of the topmost 1mm of the tumor vasculature pseudo-colored in red. b: Maximum intensity projection of the topmost 2mm of the tumor vasculature pseudo-colored in red. c: Zoom on the region marked in (a). d: The cross-sectional intensity profile of a vessel (marked in (d) as A-B), shown as experimental data and a Gaussian fit. e: Photograph of the tumor, acquired from the right side of the mouse. The orientation of the coordinate system is also shown. f: Exemplary optoacoustic tomography slice of the tumor, acquired 0.8mm below the top of the tumor. g: Optoacoustic tomography image stack of the topmost 3.8mm of the tumor, with slices every 0.4mm up to 2mm below the top of the tumor. Corresponding maximum intensity projections are shown in (a) and (b). All images acquired at 532nm illumination wavelength, size of optoacoustic images: 10mm x 10mm. Scalebars 2mm

the use of the particular illumination geometry and depth correcting inversion algorithms. With $32\mu\text{m}$ in-plane resolution, determined by imaging a microsphere of $10\mu\text{m}$ true diameter that appeared with FWHM (full width half maximum) of $42\mu\text{m}$ in the respective optoacoustic image (Ma et al. in [31]), the technique visualizes vasculature that surrounds the tumor and allows observation of individual vessels. Large tumor supplying blood vessels show to protrude into the tumor mass (indicated by arrows on Fig. 6.1b), and higher order branches of the tumor vasculature are also visible. Similar patterns are observed in consecutive slides obtained from different tumor cross-sections. As illustrated in Figs. 6.1c and 6.1d, we tracked one such vessel to an appearance width (full width half maximum of Gaussian line profile) of $49\mu\text{m}$, i.e., appearing $7\mu\text{m}$ wider than the afore-mentioned $10\mu\text{m}$ -microsphere. The vessel, therefore, has a true diameter of $17\mu\text{m}$. Due to high light absorption at visible wavelengths, the light does not penetrate into the center of the tumor, which shows particularly in the lowest two slices of Fig. 6.1g).

6.2.2 Imaging in the near-infrared

Imaging deeper in the tissue was achieved by illumination in the NIR. Results of respective NIR imaging with and without contrast enhancement are shown in Fig. 6.2. Fig. 6.2a reveals the tumor microvasculature 1.5mm below the top of the tumor at 800nm illumination wavelength. Fine blood vessels encircling the tumor are visible. Blood vessels that were visible using the 532nm illumination are also seen on the NIR illumination as shown in Fig. 6.2a. However, since the blood absorption at 532nm is much higher than at 800nm, the blood vessels at 532nm appear with higher contrast. To achieve, therefore, tumor visualization deeper into tumors, we observed instead images after gold nanorod enhancement. Fig. 6.2b shows the signal increase after injection of the gold nanorods at an elevation of 1.5mm below the top of the tumor. Already 5 minutes after injection we observed strong signal enhancement from the tumor blood vessels. Figs. 6.2c and 6.2d illustrate the effect of the contrast agent by taking intensity profiles along the arrows depicted on Figs. 6.2a and 6.2b. The signals collected before and after contrast enhancement along the long arrow profile, intersecting major blood vessels perpendicularly, are shown on Fig. 6.2c, whereby Fig. 6.2d shows the signals along the profile indicated by the short arrow, which intersects major blood vessels at a flat angle. The intensity increase is accurately co-located with the original peaks. Common intensity minima of before and after contrast enhancement show that the contrast increase is specific to the blood vessels. Post contrast enhancement intensities corresponding to blood vessels increase by a factor of at least two.

We analyzed the image contrast of optoacoustic images acquired at 800nm and 850nm and different levels below the top of the tumor before and after intravenous injection of the contrast agent. The result is illustrated in Fig. 6.2e as a bar diagram. As described in methods, the image contrast is represented by the standard deviation of the image pixel intensities. For illumination at the peak wavelength of the gold nanorod absorption spectrum (800nm), we found that application of the contrast agent caused the image contrast to increase by a factor of two at all z-positions. At 850nm, where the absorption coefficient of the gold nanorods values only 50% of its maximum, the contrast increased only by ca. 50%.

Fig. 6.2f illustrates the biodistribution of the contrast agent as a maximum amplitude projection (MIP) of a difference image stack. Each difference image of the stack was calculated by subtracting the optoacoustic image acquired at 800nm before injection of the contrast

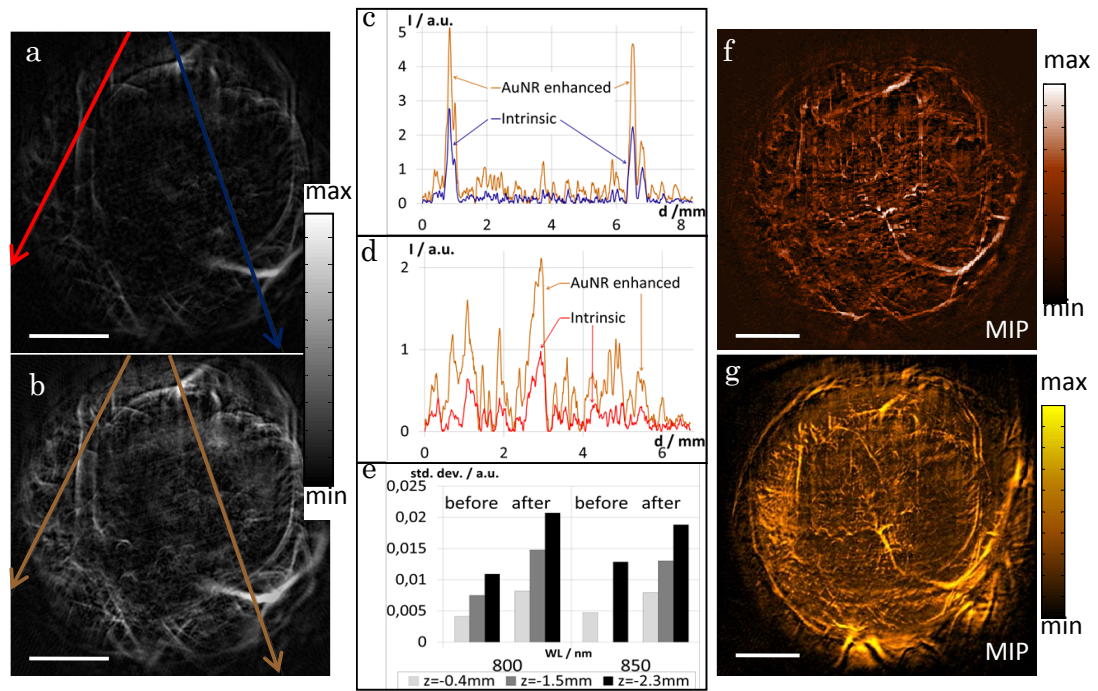


Figure 6.2: Signal and contrast increase by injection of gold nanorods. a: Optoacoustic image acquired at 800nm illumination wavelength, 1.5mm below the top of the tumor before injection of gold nanorods. b: Optoacoustic image acquired at 800nm illumination wavelength, 1.5mm below the top of the tumor after injection of gold nanorods (a and b have a common colorbar). c and d: intensity profiles along axes depicted in a and b, pointing out the absorption increase at site of the blood vessels. e: Bar diagram of whole image contrast (standard deviations) of optoacoustic images acquired at different illumination wavelengths and levels below the top of the tumor for comparison of image contrast before and after injection. f: Optoacoustic maximum intensity projection of the gold nanorod distribution (top 2.5mm of the tumor) calculated by subtraction of baseline images from gold nanorod contrast enhanced images. g: Optoacoustic maximum intensity projection of the gold nanorod distribution (top 4mm of the tumor) calculated by independent component analysis of the gold nanorod contrast enhanced images.

agent (baseline image) from the respective optoacoustic image acquired at 800nm after injection of the contrast agent. Corrections for light attenuation were applied as described in methods. Fig. 6.2f shows that the nanorods are not only distributed throughout the major blood vessels (e.g., at the lower right), but also penetrate into the randomly oriented tumor microvasculature. Fig. 6.2g shows also an image (MIP) of gold nanoparticle biodistribution, which was, however, calculated using guided independent component analysis (guided ICA) to resolve the distribution of gold nanoparticles. The image analyzed images at 800nm, 850nm, and 900nm, using the spectra of oxygenated hemoglobin, deoxygenated hemoglobin, and the gold nanorods as an initial guess for the ICA. The resulting ICA component with the spectral characteristics corresponding to the gold nanorods was selected. The MIP covers the top 4mm of the tumor, i.e. the entire part of the tumor protruding out of the mouse body, revealing the microvasculature inside the tumor, as well as the tumor-encircling blood vessels at lower levels. The contrast agent again appears to distribute throughout the major supply vessels and into the

diffuse tumor vasculature, hence, confirming Fig. 6.2f.

6.2.3 Validation studies

Photography of the tumor imaged revealed a major blood vessel that approached the tumor from the right flank and bifurcating, ultimately encircling the tumor as shown in the respective optoacoustic image stack (Fig. 6.3a). Deeper seated vessels were not visible as expected. To validate the presence of deeper seated vessels, we relied on the cryoslice color and fluorescence imaging of the top 4mm of the tumor (cf. Fig. 6.3).

To validate the optoacoustic images obtained *in vivo*, we performed cryoslice color and fluorescence imaging of the top 4mm of the tumor. Fig. 6.3a shows optoacoustic images from different positions perpendicular to the z-direction (height) through the tumor and Fig. 6.3b demonstrates corresponding cryoslicer images obtained from approximately the same tumor height. The optoacoustic images acquired at 0.4mm and 1.5mm below the top of the tumor (Figs. 6.3a1 and 6.3a2) demonstrate high contrast from blood vessels congruent with diffusive red patches of tissue seen on the corresponding color slices (Figs. 6.3b1, 6.3b2). The red patches are characteristic of higher vessel density. As expected, the optoacoustic images offer higher resolution and contrast from blood vessels, since the photographs of Fig. 6.3b suffer from photon scattering.

Fig. 6.3c zooms in Fig. 6.3b1, obtained 0.4mm below the top of the tumor, offering a more detailed view of the vasculature distribution. The in-plane width of the skin was less than 0.5mm, with the strongly vascularized subcutis (SC) beginning at about 0.2mm as shown in Fig. 6.3d [81]. Therefore, only vessels deeper than 0.5mm are attributed to infiltrating cancerous tissue.

Slicing lower into the tumor revealed dark-red patches in the center of the tumor. An exemplary corresponding fluorescence cryoslice image shows accumulation of the Texas Red labeled lectins in the areas appearing dark red in the color images (cf. Fig. 6.3e).

Figs. 6.3f-h show the architecture of the tumor microvasculature at levels corresponding to those of the optoacoustic images in Figs. 6.3a1, 6.3a2 and 6.3a4, respectively, obtained by fluorescence microscopy of the Texas Red labeled lectin. These figures ultimately prove

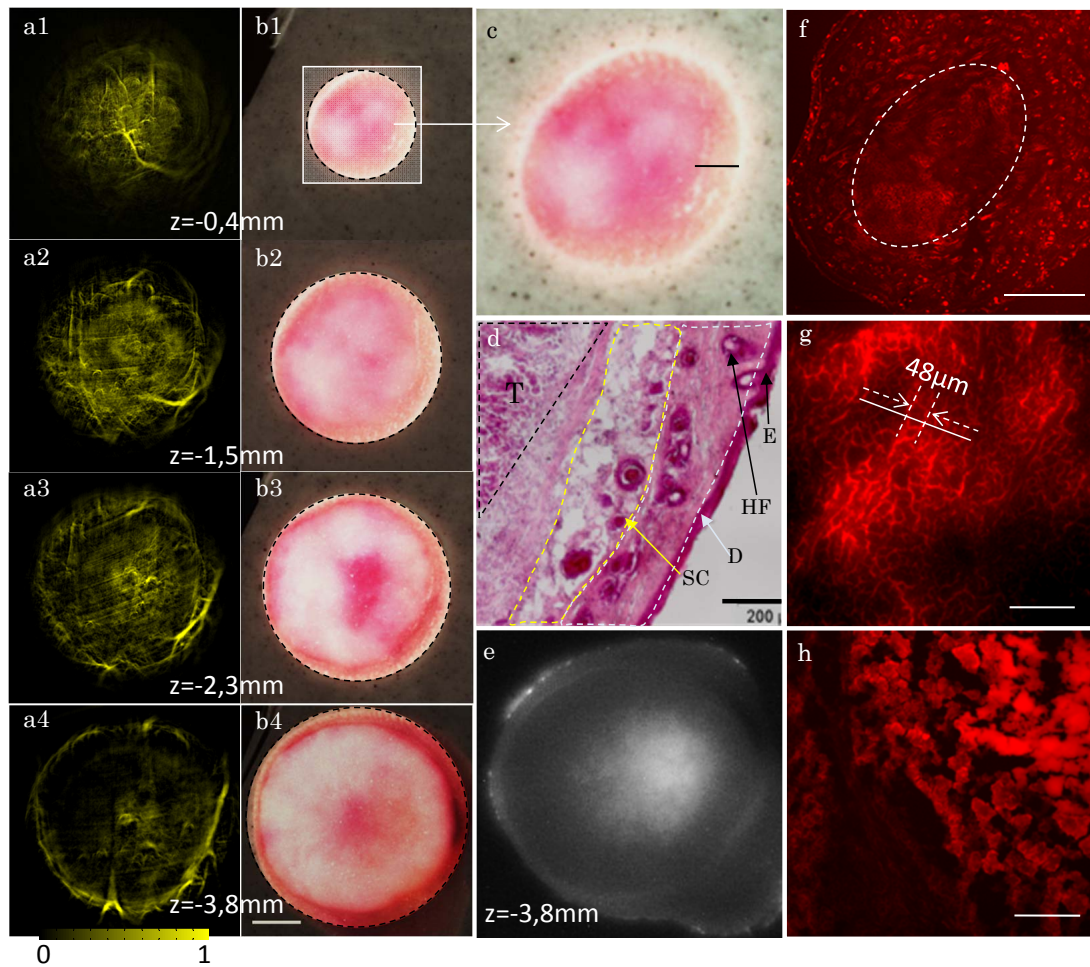


Figure 6.3: Profound imaging of tumor vasculature. a1-a4: Stack of optoacoustic images after injection of AuNR at 800nm illumination showing vasculature of the top 4mm of the tumor. b1-b4: Cryoslice color images at z-positions corresponding to optoacoustic images. Tumor region masked. Scalebar 2mm. c Enlarged cryoslice color image at 0.4mm depth, pointing out the maximal width of the skin in the optoacoustic images, as well as tumor heterogeneities. Scalebar: 0.5mm d: HE immunostained cryosection 1.5mm below the top of the tumor (E epidermis, D dermis, SC subcutis, HF hair follicle, T tumor). Tumor tissue begins already 0.5mm below the skin surface. Scalebar: 200 μ m. e: Fluorescence cryoslice image of distribution of lectins inside the tumor corresponding to Fig. b4 (z=-3.8mm). f-h: Fluorescence microscopy images of Texas Red labeled lectin distribution in the tumor recorded at levels below the top of the tumor corresponding to Fig. a1 (f), Fig. a2 (g), and Fig. a4 (h). First appearance of the tumor vasculature at 0.4mm depth (f, encircled). Scalebars 400 μ m (f), 200 μ m (g,h).

that the tumor was vascularized throughout its entity. The transition between the subcutaneous tumor-surrounding vasculature and the tumor microvasculature is illustrated in Fig. 6.3f. In particular, this image shows that the randomly oriented tumor microvasculature already appeared at the very top of the cancerous tissue, and that the transition between tumor surrounding vasculature and vasculature infiltrating cancerous tissue is gradual on a microscopic level.

The architecture of the tumor microvasculature prevailing throughout the major part of the tumor tissue is shown in Fig. 6.3g. This image was exemplarily obtained from the cen-

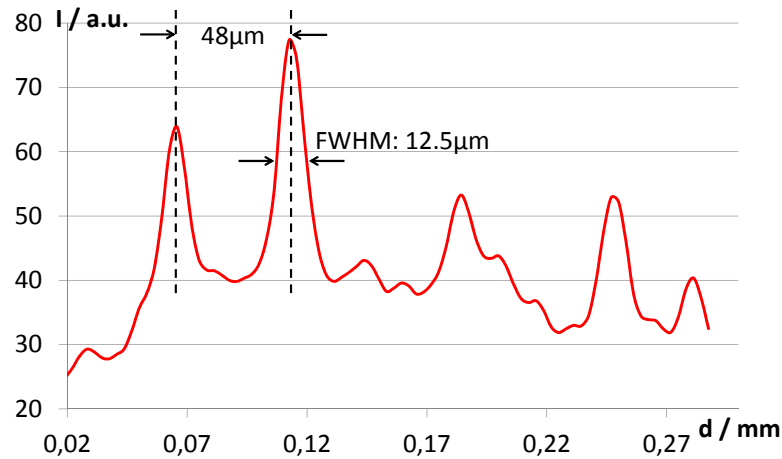


Figure 6.4: Intensity profile obtained along the line in Fig. 6.3g indicating exemplary widths of microvessels and the spacings between microvessels.

ter of the tumor at $z=-1.5\text{mm}$. In addition to revealing the random orientation of the tumor microvasculature, this image points out the importance of imaging such tumor at resolutions better than $40\mu\text{m}$. The shown microvessels are typically spaced apart by less than $50\mu\text{m}$ (see mark in Fig. 6.3g), whereby their diameter / thickness is on the order of $10\mu\text{m}$ to $15\mu\text{m}$ (cf. intensity profile in Fig. 6.4 obtained along the line in Fig. 6.3g). If the optoacoustic system would not provide imaging resolutions significantly better than $50\mu\text{m}$, such microvasculature could not even theoretically be resolved by the optoacoustic system.

Fig. 6.3h illustrated the shape of the tumor vasculature in the left border region of the dark-red patch located in the center of the tumor at $z=-3.8\text{mm}$ (cf. Figs. 6.3a4, 6.3b4, 6.3e). Compared to the microvasculature in the surrounding of the dark-red patch, this vasculature shows to be much thicker and more heterogeneous and agglomerated. Fig. 6.3h, furthermore, shows that the fluorescence appears to originate not only from the vasculature, but also from the interstice in proximity of the microvessels.

6.2.4 Three-dimensional rendering

The above described imaging results built the basis for three-dimensionally rendered accurate images of the tumor vasculature up to 4mm below the top of the tumor (Fig. 6.5). Figs. 6.5a and b illustrate that at 532nm illumination, the outermost 1.5mm of the tumor appeared with high intrinsic contrast and large amount of structural details. Figs. 6.5c and d on the other

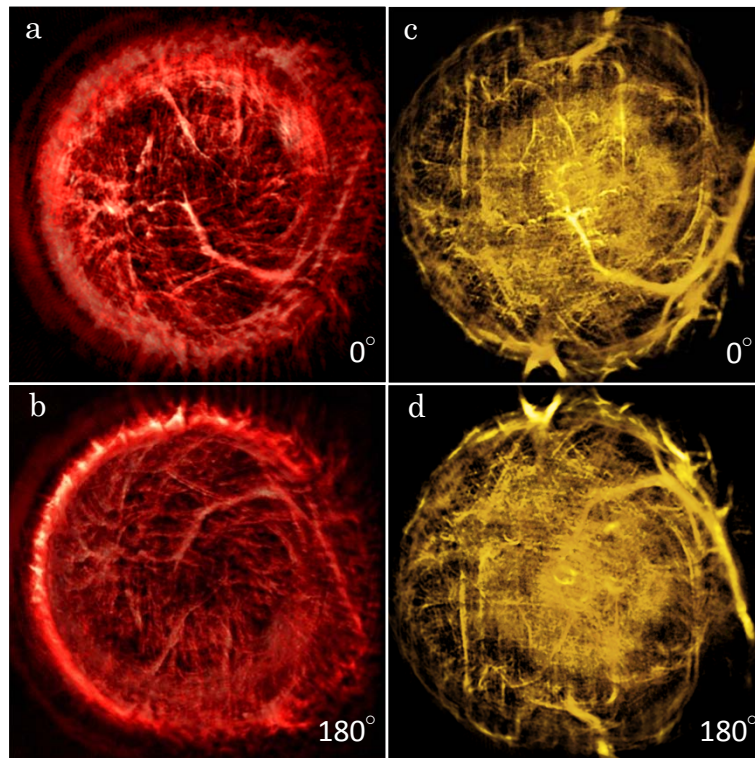


Figure 6.5: Three-dimensionally rendered shape of the tumor blood vasculature. a: The tumor microvasculature rendered with the optoacoustic tomography stack data acquired at 532nm (a subset of the image stack is shown in Fig. 6.1g). b: Rendered vasculature of (a) turned by 180 degrees, i.e., viewed from the inside of the tumor. c: The tumor microvasculature rendered with the optoacoustic tomography stack data acquired at 800nm after contrast enhancement by intravenous injection of gold nanorods (a subset of the image stack is shown in Fig. 6.3a). d: Shows the rendered vasculature of (c) turned by 180 degrees, i.e., viewed from the inside of the tumor.

hand reveal also fine vascular structures at larger depths of the tumor, as they were acquired with NIR illumination in combination with blood-pool contrast enhancement by gold nanorods. The visualized vascular structures ranged in size from major peripheral vessels to profoundly situated microvessels, as indicated especially by comparison of Figs. 6.5b and d. While in Fig. 6.5b no structures in the center of the tumor hinder viewing the subcutaneous vasculature, in Fig. 6.5d the dense tumor microvasculature almost entirely blocks the view of the large blood vessel in the image center.

6.3 Discussion

In this study we investigated experimental mouse tumors with high resolution by volumetric optoacoustic tomography, showing structural and functional tumoral features throughout entire tumors. Imaging with 532nm illumination allowed us to obtain high-contrast images of tumor

vasculature up to a penetration depth of 2 millimeters. We attribute the high contrast of the vessels over the background to the high absorption coefficient of hemoglobin in combination with large hemoglobin concentration differences between the blood vessels and the background tumor tissue. We tracked the shape of blood vessels and exemplarily determined the true size of a blood vessel that penetrated into the tumor by comparing its appearance in the optoacoustic image (FWHM) with a microsphere imaged optoacoustically with the same transducer. The vessel had a diameter of 17 microns - a diameter comparable to that of microvessels within the tumor. Images of the tumor at elevations (z-axis) of 2 and more millimeters below the top of the tumor showed a highly absorbing ring of subcutaneous vasculature. At 532nm, no absorbers at the inside of this ring could be identified in the optoacoustic images, where in fact absorption heterogeneities were expected, as validated in section 6.2.3. It is, therefore, concluded that the 532nm illumination, penetrating the tumor radially inwards (cf. Fig. 4.11), was attenuated by the subcutaneous vasculature too strongly for the absorbers in the center of the tumor to create optoacoustic signal exceeding the noise level. To penetrate through the dense subcutaneous vasculature, illumination needed to be changed to a wavelength at which the absorption of hemoglobin was substantially lower, i.e. to the NIR.

Illumination in the NIR (800-900nm) allowed us to image the whole tumor, albeit requiring vessel-specific contrast enhancement, as the absorption coefficient of hemoglobin is ca. 50 times lower at 800-900nm than at 532nm. We achieved such contrast enhancement by intravenous application of gold nanorods. The fact that the line profiles of before and after injection, shown in Fig. 6.2c,d, have common minima and maxima indicates that the contrast increase is indeed strictly vessel-specific, or respectively that the gold nanorods do not diffuse out of the vessels during the experiment. The nanorods had an absorption maximum at 800nm, doubling the image contrast at 800nm, whereas at 850nm the image contrast was increased by 50% as also the absorption of the nanorods valued only half the maximum absorption. The doubling, or respectively 50% increase, was independent of the depth below the top of the tumor, showing that the nanorods perfused the whole tumor. Taking the intrinsic absorption of hemoglobin at 800nm into account ($\mu_a(\text{HbO}_2)=1.9/\text{cm}$, $\mu_a(\text{Hb})=1.8/\text{cm}$, see appendix A.1), we deduced that the extrinsic absorption increase by the 50 μl gold nanorod suspension (OD 50) valued 1.9/cm assuming physiological oxygen saturation in blood of more than 80%. Respectively, the extrinsic absorption contribution of the nanorods at 850nm ($\mu_a(\text{HbO}_2)=2.5/\text{cm}$, $\mu_a(\text{Hb})=1.6/\text{cm}$) valued (again assuming 80% oxygen saturation) $0.5 \cdot \mu_a(\text{blood}) \approx 1.2$.

We tracked the distribution of the gold nanorods within the tumor in two ways: by subtracting optoacoustic images acquired before contrast enhancement by nanorods injection from optoacoustic images acquired after contrast enhancement by nanorods injection, and by multispectral analysis of optoacoustic images acquired at multiple wavelengths after nanorods injection. Both approaches showed self-consistently the same distribution of contrast agents, penetrating from major tumor supply vessels into the diffuse tumor microvasculature, albeit the multispectral analysis was more accurate, showing more details of microvasculature than the image subtraction approach.

Ultimately, we imaged the entire AuNR enhanced tumor at 800nm illumination wavelength and confirmed the non-invasive findings on the anatomical appearance of tumor vasculature by means of invasive imaging methods (Fig. 6.3). We found that areas of the tumor appearing highly vascularized in the optoacoustic images (Fig. 6.3a) appeared with a reddish stain in the cryoslice color images (color slices, Fig. 6.3b), whereas areas in the optoacoustic images appearing weakly vascularized appeared white in the color slices. We attributed these appearances to high and low concentrations of hemoglobin. In particular, the color slices confirmed the above (see discussion regarding 532nm illumination) identified dense subcutaneous vasculature showing as a dark red (light-blocking) ring-shaped structure in the color slices, and hindering optoacoustically imaging the center of the tumor. This dense subcutaneous vasculature was also shown on the optoacoustic images in higher detail. Cryoslice fluorescence images of Texas Red labeled lectins allowed us to collocate strongly fluorescing areas with areas appearing reddish in cryoslice color images. Fluorescence microscopy of the respective cryosections showed that density of tumor microvasculature correlated with the strength of the fluorescence signal in the fluorescence cryoslice images, i.e., strongly fluorescing regions (cf. Fig. 6.3h) showed denser microvasculature than weakly fluorescing regions. Additionally, we investigated the transition from tumor tissue to the epidermis at various locations within the tumor by fluorescence microscopy and light microscopy of HE stained cryosections, determining the structure and width of the skin, with the skin being less than 0.5mm thick. This means that all optoacoustic images acquired at z-positions lower than 0.5mm below the tumor top contained microvasculature that penetrated the bulk tumor tissue. The high accuracy of the non-invasively obtained optoacoustic tomography images allowed us to finally three-dimensionally render the entire tumor vasculature for more thorough visual inspection. Such representation showed to facilitate the volumetric investigation of tumor heterogeneities.

Concluding on the hardware developmental point of view, the key component was the tomographic scan ring (i.e., fiber-bundle-based ring illuminator) which allowed full 360 degrees optoacoustic tomography with quasi-static in-plane illumination. The in-plane illumination geometry prevented from out-of plane artifacts, while guiding the light through a fiber bundle as close as 25mm to the tumor surface facilitated imaging at even 900nm by reducing the amount of light absorbed by the coupling medium water. Inherently, the light path is not interrupted during the entire imaging session, thus, lost-projection artifacts are avoided. As described in methods, the in-plane resolution was determined to be 32 μ m, whereas the elevational resolution, as further described in section 4.3.1, was better than 150 μ m. We proved that such resolution was ultimately necessary to separate the microvessels in the tumor, and that resolutions above 50 microns would not be sufficient (cf. Fig. 6.4). Besides the illumination and detection hardware and design, the way of positioning the animal prevented from motion artifacts in the images. From the data processing point of view, corrections for the light flux distribution inside the tissue allow a detailed insight into the core of the tumor.

In summary, we have demonstrated how high resolution in optoacoustic imaging of tumor neoangiogenesis can be maintained depth-independently, allowing to non-invasively investigate intratumoral features that could before only be visualized invasively at similar resolutions. In particular, the herein non-invasively and *in vivo* visualized shape of the tumor vasculature is comparable to the structures demonstrated in other studies with solid tumors [82] [55] [83] [84] [85] [86] [87] [69]. In addition, we showed the potential of gold nanorods as contrast agents penetrating into the tumor vasculature. We confirmed the optoacoustic imaging results by showing the self-consistency of optoacoustic images acquired with different imaging parameters, and by invasive *post mortem* validation methods. We proved that gold nanorods are a contrast agent that is valuable for optoacoustic imaging, allowing to image the whole tumor even through dense subcutaneous vasculature. The increase in optoacoustic signal attributed to the contrast agent would allow, for example, to reduce of the number of signal averages, to lower acquisition times, or respectively reduce the illumination intensity or transducer sensitivity, enabling the use of transducers that detect even higher frequencies. Such transducers will provide higher tomographic resolutions and ultimately allow visualizing even more details of the tumor vasculature, empowering new applications.

Promising future applications would be related to pharmacological investigations for drug developments via tumor xenografts. It has been proposed to avoid large numbers of ani-

mals by performing such investigations as longitudinal studies noninvasively and *in vivo* [88] [31] [25] [84]. Such a longitudinal study has been, for instance, already implemented as a photodynamic therapy study on tumors implanted in the chicken chorioallantoic membrane (CAM) upon removal the shell [55], and it would be a promising subject for further investigations in mice [64]. In general, the herein presented optoacoustic tomography approach could obliterate remaining important challenges in biological cancer imaging. From visualizing only superficial tumor structural and functional parameters, high resolution imaging throughout tumors could reveal a better understanding on the heterogeneous patterns of tumor growth, the spatially dependent drug biodistribution and the differences, for example, in apoptotic vs. surviving cells after a treatment protocol.

Chapter 7

Other applications

Although the optoacoustic imaging system was specifically developed for mouse tumor imaging, other samples were also investigated therewith, as further presented in **section 7.1** of this chapter. In subsection 7.1.1, various non-invasively acquired visualizations of the head vasculature of a mouse are described, showing subcutaneous and profound cranial vasculature. The images demonstrate the improved imaging accuracy as compared to the former state of the art. Further visualizations of the superficial mouse tumor vasculature are presented in subsection 7.1.2. Additional optoacoustic imaging of zebrafish thinner than 1mm is discussed in subsection 7.1.3, of *Gammarus* is discussed in subsection 7.1.4, and of an exemplary tissue sample of a big animal (herein pig) is discussed in subsection 7.1.5. In **section 7.2** of this chapter, a study for volumetric validation of tumor vasculature by micro-CT is presented, which, other than respective state-of-the-art methods, does not require any *in vivo* processing of the tumor.

7.1 Tomographic optoacoustic imaging

7.1.1 Mouse head vasculature

The mouse head vasculature was investigated by direct top illumination with visible and NIR light, aiming at comparing the features visualized per illumination wavelength. Moreover, the imaging performance superior to state-of-the-art imaging systems should be demonstrated

[89]. The illuminating beam was expanded by spherical lenses to cover the whole head of the mouse, and the mouse's rear head was oriented horizontally (see Fig. 7.1b), which at the same time was the imaging plane. The mouse head orientation was, therefore, comparable to that described in [59]. The transducers PNDT V319 and V320 described in section 4.3.1, as well

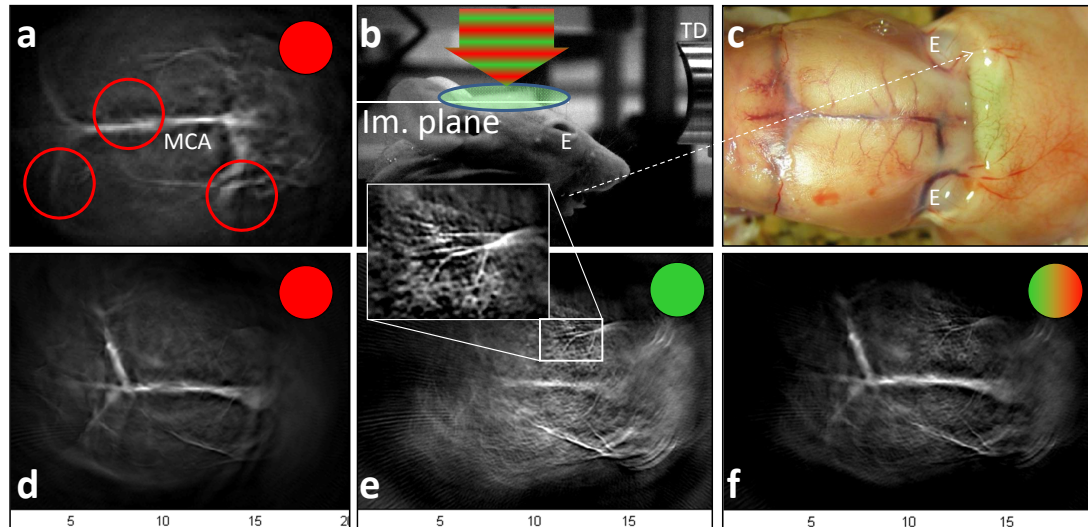


Figure 7.1: Optoacoustic tomography of mouse head vasculature. a: Optoacoustic tomography of the image plane indicated in (b) acquired with transducer PNDT V382 and 750nm illumination. Large blood vessels such as the mid-cranial artery (MCA) are shown with low resolution. Fine microvessels are not shown. b: Schematic of the planar experimental arrangement with unidirectional illumination from the top (E: Eye, TD: Transducer). c: Photograph of dissected mouse head showing major cranial blood vessels and subcutaneous vasculature. d: Optoacoustic tomography of the image plane indicated in (b) acquired with transducer PNDT V320 and 750nm illumination. e: Optoacoustic tomography of the image plane indicated in (b) acquired with transducer PNDT V320 and 532nm illumination. f: Weighted overlay of images (d) and (e) showing precisely the superficial subcutaneous microvasculature along with the profound major blood vessels of the head.

as a third cylindrically focused transducer, the PNDT V382 (focal length 38.1mm, element diameter 13mm, central frequency 3.5MHz, -6db bandwidth 76% of central frequency), were employed for imaging. The corresponding setup is described in section 4.3.2. A nude mouse was imaged *post mortem* (cf. chapter 5) without exogenous contrast agents. The images were reconstructed by backprojection as described in section 3.2.1. Where applicable, weighted overlays of images at different wavelengths were rendered to provide thorough insights on the imaged structures.

Fig. 7.1 shows the imaging results for 750nm (red dot) and 532nm (green dot) illumination wavelength with corresponding validation by dissection. It is illustrated how red illumination is advantageous for visualization of deeply situated structures, such as the mid-cranial artery (MCA). Such large blood vessel only vaguely appears in the 532nm image, which, however, shows the small micro-vessels of the skin in more detail. The reason for this lies in the

absorption spectrum of hemoglobin, influencing the blood to have at 750nm about 50 times lower absorption coefficients than at 532nm ($\mu_a(532nm) \approx 100/cm$). In consequence, the superficial microvasculature is also revealed in much lower contrast than at 532nm.

7.1.2 Mouse subcutaneous tumor vasculature - superficial imaging

If the aspect ratio of the specimen is such that its size in elevational direction (i.e. perpendicular to the tomographic image plane) is not much smaller than its size in longitudinal direction (i.e. in the image plane), top illumination results in faulty images at depths larger than approximately 0.5mm (cf. chapter 5). Then, it is crucial to collocate the imaging (detection) plane with the illumination plane, to reduce out-of-imaging-plane artifacts. In first experiments, before the fiber-bundle-based ring illuminator was developed (see section 4.3.2), tumors could be investigated with in-plane free-beam bilateral illumination only in the visible spectrum (water paths too long for NIR). The corresponding setup configuration is shown in Fig. 4.10. In consequence, only the vasculature on the periphery of the tumor, e.g., of the mouse subcutis, could be investigated.

In such a configuration, the top-most 1mm of a 4T1 tumor of approximately 8mm diameter was scanned with the V319 transducer and reconstruction was performed by back-projection. Fig. 7.2 shows a three-dimensionally rendered tumor (tile a) and a corresponding

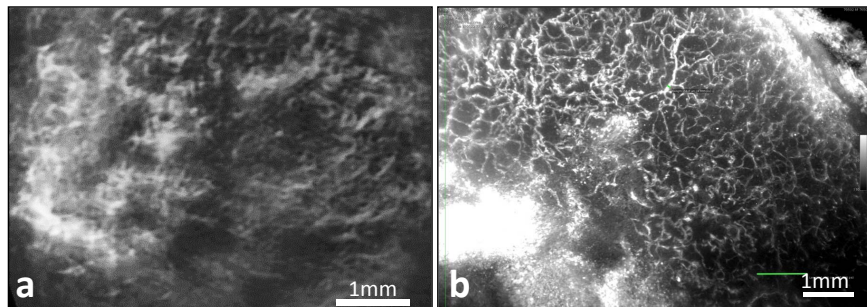


Figure 7.2: Superficial imaging of the microvasculature of a 4T1 tumor. a: Image of a three-dimensionally rendered optoacoustic image. b: Validation by fluorescence microscopy.

(invasively obtained) optical microscopy image (tile b). It illustrates that the system is capable to resolve fine subcutaneous microvasculature non-invasively with up to 0.03mm in-plane resolution. The randomly oriented tumor microvasculature revealed by optoacoustics showed to extend over large areas of the tumor, containing denser and less dense vascularized regions as

well as larger and smaller vessels. The region of high intensity towards the left of the image appeared highly vascularized. Therein, relatively large hemoglobin concentrations lead to high absorption coefficients (especially in the visible spectral range), implying strong optoacoustic signals (high initial pressures, cf. chapter 2).

7.1.3 Zebrafish in early developmental stage

Two zebrafishes were imaged by optoacoustic tomography with the goals of identifying anatomical structures, and visualizing the expression of mCherry. Thereby, two general investigative methods were applied:

1. two-dimensional sagittal projection images for the fast visualization of structures within the fish (towards mapping of probes)
2. coronal tomographic imaging with the intent to gain three-dimensional information.

The optoacoustic experiments were set up in accordance with these goals.

Experimental procedure

Sample preparation. The prepared samples are shown in Fig. 7.3. Each fish was embedded into 1.3 m-% agar gel for reproducible positioning in the imaging system. In case of sample 1, the fish's longitudinal axis was inclined by 15° relative to the imaging plane, with the head pointing downwards. In sample 2, the fish's longitudinal axis was oriented perpendicularly to the imaging plane.

The optoacoustic setup. For these proof-of-principle experiments, the whole agar phantom is illuminated from the top along its cylindrical axis at the wavelength 532nm and in the NIR, allowing for multispectral decomposition. The pulse repetition rate is 20Hz. The PZT-transducers PNDT V319 and PNDT V320 were used for the measurements for the following reasons:

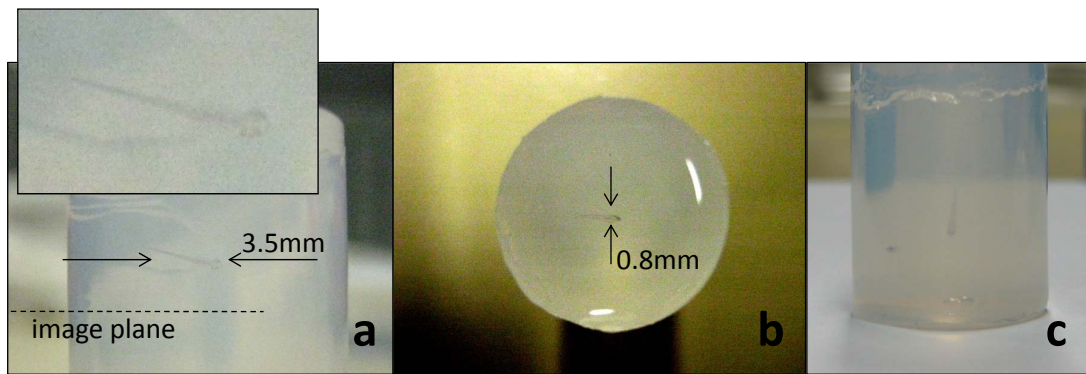


Figure 7.3: Transparent agar phantoms with 3.5mm long zebrafish. a,b: Sample 1, showing that the fish is oriented slightly inclined relative to the imaging planes (imaging planes along the dashed line). c: Sample 2. The fish is oriented perpendicular to the imaging planes, as shown in the right photograph.

- Panametrics NDT V320. With its relatively weak transversal focus (numeric aperture of 1.95), this transducer allowed to image projections of slices that were more than 300 μm thick, providing an immediate impression of the sample structure.
- Panametrics NDT V319. When three-dimensional information was of interest, this transducer was employed. The transducer's significantly tighter focus enables transversal resolutions of below 150 μm . Its elevation-independent in-plane resolution of 0.03mm allowed accurate tomography of the sample.

Reconstruction Method. Image reconstruction was done by the backprojection algorithm, wherein the data was filtered and thresholded before the reconstructions. The filter band was optimized by visual inspection and validation. For multispectral decomposition of the data, independent component analysis was applied, since the absorbers inside the fish were a-priori unknown.

Experiment 1 - Sagittal Projection Intrinsic Contrast Imaging of Sample 1. Imaging was performed with 532nm illumination and acquisition of 2000 projections per slice for assuring a high signal-to-noise ratio and minimizing imaging artifacts. In elevational direction, a region of 2mm around the level of the fish head (approximate extension in elevation: 1mm) was investigated. The signal was high-pass filtered at 20 MHz, a frequency corresponding to a tomographic in-plane resolution of below 40 μm . The obtained optoacoustic images were validated by optical transmission microscopy and by comparison with the literature.

Multispectral optoacoustic tomography - towards resolving constituents. The experiment described in the previous paragraph was repeated at the wavelengths 740 and 765nm with the intent to resolve spectrally independent constituents. Obviously, mCherry did not absorb light in the NIR. Therefore, it is expected that structures appearing at 532nm and belonging to mCherry molecules would vanish in the NIR. Lacking further information about the sample, independent component analysis was applied to simultaneously evaluate the localization of the various absorbers along with their absorption spectra.

Experiment 2 - Intrinsic Contrast Coronal Imaging of Sample 2. In this case, diffuse illumination occurred at 532nm to exploit the high intrinsic contrast. The strong focusing of the transducer V319 allowed to resolve thin planes.

Results and Discussion

Experiment 1. At first, reconstruction via backprojection of the plain unprocessed signal allowed detecting the orientation, shape and major anatomical structures like the eyes and backbone of the 3.5mm long zebrafish (Fig. 7.4). The specificity to small substructures was

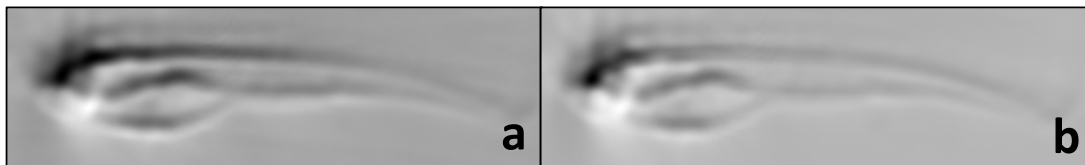


Figure 7.4: Optoacoustic images of 3.5mm long zebrafish reconstructed by backprojection of unprocessed signals at 532nm (a) and 740nm (b) illumination wavelength. Major structures (e.g., eye, pigment stripes) are shown. Also, the image at 532nm reveals a significantly higher contrast than in the NIR as can be recognized in the regions of the pigment stripes.

achieved by high-pass filtering and thresholding the signal before the backprojection. Then, additional internal structures like the backbone (BB), vasculature (V) and/or pigment spots/stripes (PS) were resolved. The pigments were expected to also be present in the strongly absorbing eyes. Substructures inside the head, which were at first unclear, were validated by comparison with the literature [90], as shown in Fig. 7.5 .

Anatomical structures shown in the optoacoustic image, comprise the eyes (E), other parts of the head / skull (SK), parts of the intestinal tract (IT) and the swim bladder (SB),

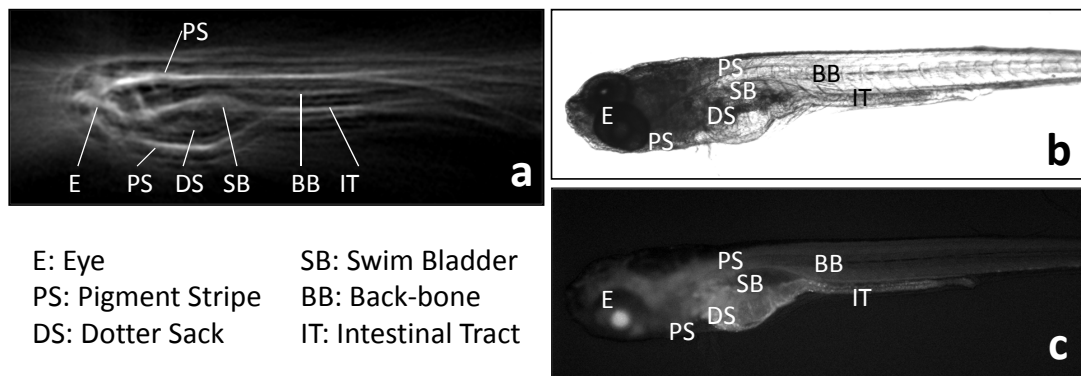


Figure 7.5: Projection images of the 3.5mm long zebrafish revealing structures like the backbone, pigment stripes and/or blood vessels, e.g., of the head, intestinal tract as well as parts of the leftover yolk sack and swim bladder. a: optoacoustic tomography image, b: optical microscopy image, c: fluorescence microscopy image selective to mCherry.

which was located in proximity of the yolk sack (DS) that was still present at that stage of growth. The yolk appeared in the mCherry fluorescence image which might partly be due to auto-fluorescence. For further validation of the optoacoustic images, volume-rendered data acquired by optical projection tomography was used (Fig. 7.6).

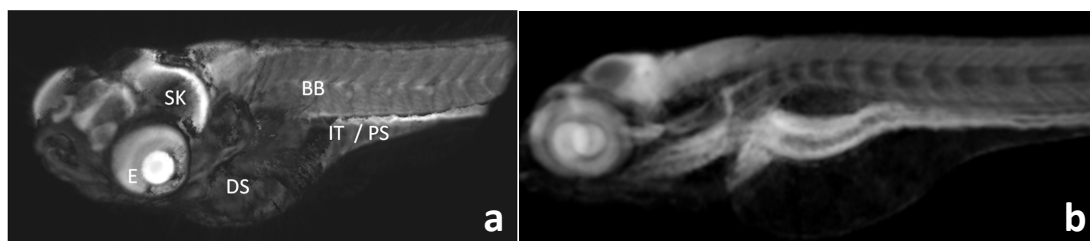


Figure 7.6: Validation images. a: Optical Projection Tomography (OPT) image of a 96 hours old zebrafish (very similar developmental stage) utilized as a reference for validation. The OPT Data was obtained from the internet presence of Monash University [90]. Identifiable are structures like the eyes (E), parts of skull and brain (SK), the yolk sack (DS), the muscle fibers incl. the backbone (BB) and the intestinal track (IT). b: sagittal MIP

Figs. 7.7a-d show that the light penetrated the entire fish well, as structures within the fish were observed in all images. Also, it appeared that generally no structures of the sample were selectively absorbing light of 532nm. Therefore, mCherry cannot have been immediately localized. To more precisely investigate the spatial distribution of mCherry, spectral decomposition methods were applied.

Depending on the elevational position of the detector, different regions within the fish were emphasized. This effect appeared especially in the head region, as illustrated in Fig. 7.6. The images acquired at 532nm, 740nm and 765nm (see Fig. 7.7) were multispectrally decomposed to indicate how absorbers with different absorption spectra were distributed throughout the sample. Before the decomposition, the images were normalized by the actual local irradi-

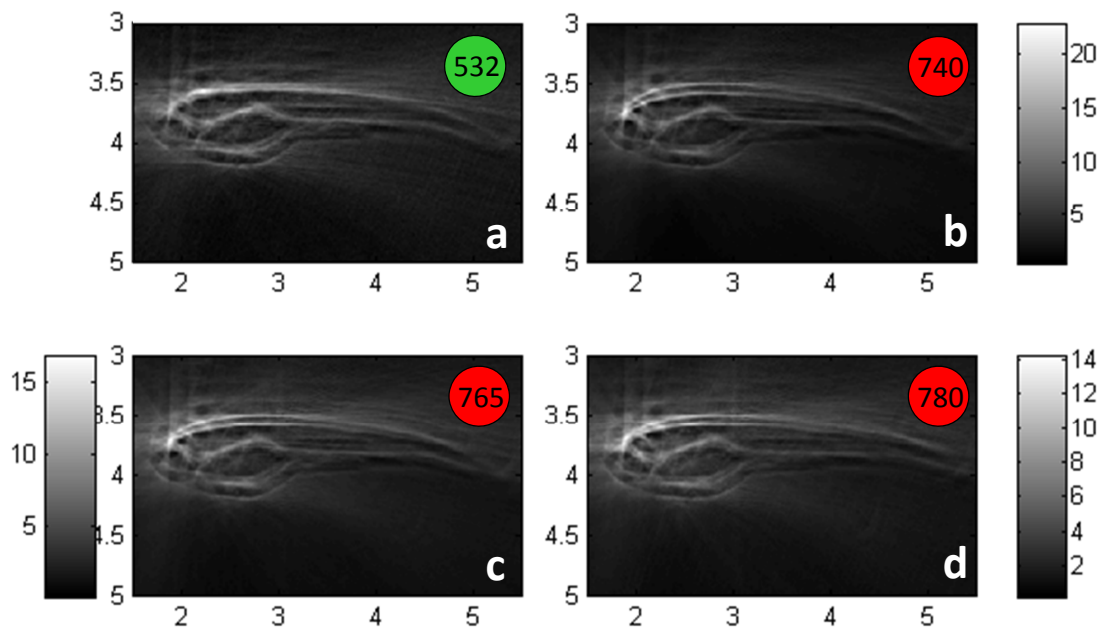


Figure 7.7: Optoacoustic images of the zebrafish at various illumination wavelengths (532nm (a), 740nm (b), 765nm (c), 780nm (d)) revealing only minor spectral dependence.

ance.

When visualizing the distribution of constituents with different absorption spectra, especially the hemoglobin could be identified. This was deduced by comparing the absorption spectra (cf. literature [20]) with the spectra shown in Fig. 7.8. It was found that component 3 was comparable with deoxygenated hemoglobin, component 2 was matched to oxygenated hemoglobin and component 1, showing a high contrast in the region of the eye and pupil and a relatively linear decrease in the absorption spectrum, was interpreted as melanin pigment-like (exponentially decreasing).

The plot of the spectra (see Fig. 7.9) suggested that the original images in Fig. 7.7 mainly consisted of component 3 - a fact further enforcing the above discussion. Essentially, the strong high-pass filtering and thresholding seemed to result in a quasi-amplification of the purely pigment like regions or quasi-suppression of the signal arising from the vasculature in this case.

Experiment 2. This experiment generally exploited the 'aspect ratio' of the fish by matching the low-resolution dimension of the detector (i.e., transversal) with the dimension in which the

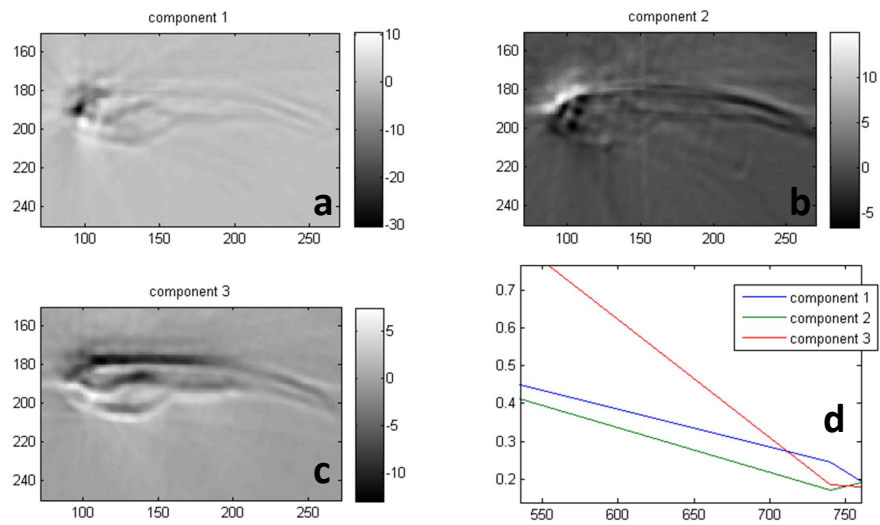


Figure 7.8: Multispectral decomposition showing the general distribution of three components with different absorption spectra of which two resemble those of oxygenated and deoxygenated hemoglobin.

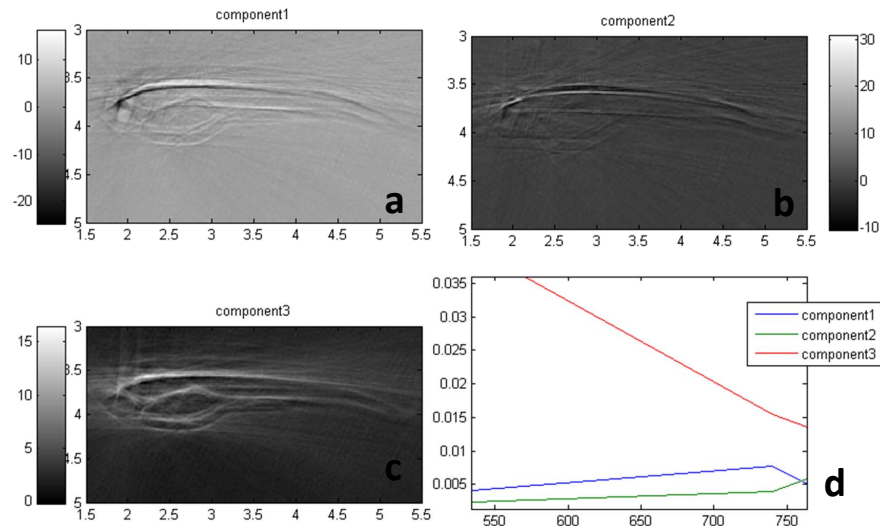


Figure 7.9: Multispectral decomposition of the images shown in Fig. 7.7 with corresponding absorption spectra.

fish anatomy did not vary significantly. An example of a resulting tomographic set is shown in Fig. 7.10, revealing, e.g., the fine-structures of the tail and other parts of the body.

Conclusion

The results discussed above point out the potential to resolve features of organisms smaller than 3.5mm long and 0.8mm thin. In this example, the organism is a zebrafish of only a few

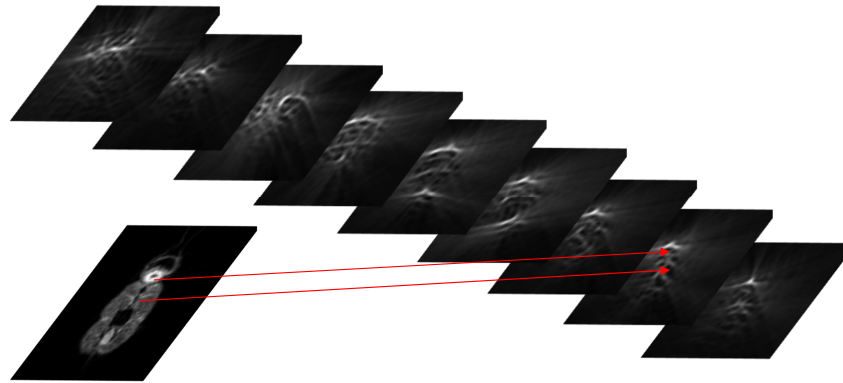


Figure 7.10: Optoacoustic tomographic image stack as coronal view with an exemplary validation of the fine-structure of the zebrafish tail. Distance between acquired slices: 250 μ m. The images are 1.5mm wide.

days age. Already the high acoustic tomographic resolution of less than 32 microns allowed to achieve such results. In combination with in-plane illumination and further elevational focusing of the laser beam, for example in form of the setup configuration presented in section 4.3.2, especially experiment 2 (fish longitudinal axis oriented perpendicular to the image plane), is expected to show better precision in terms of three-dimensional resolution.

7.1.4 Gammarus imaging

In proof-of-principle investigations, *Gammarus Lacustris* were investigated, to show another potential field of application of the developed setup. Herein, one selected exemplary optoacoustic tomography experiment is presented. The system configuration used the fiber-bundle-based ring illuminator described in section 4.3.2, which was also employed, i.a., for *in vivo* imaging of tumor vasculature (see chapter 6). The optoacoustic imaging results were validated by cryoslice color imaging.

Experimental Procedure

Two *Gammarus* were imaged by optoacoustic tomography with varying imaging parameters:

- Illumination wavelengths: 532nm and 750nm
- Illumination design: quasi-static ring illumination through four-arm fiber bundle

- Ultrasonic detectors: Panametrics NDT V319, V320

After sacrifice, the Gammarus were embedded in agar (1.3 m-% agar gel matrix, cylindrical shape, temperature at embedding below 40°C), which was then stored in distilled water at 4°C, avoiding degradation of the tissue. All Gammarus were oriented along the cylindrical axis of the agar phantom. Further experimental parameters were:

- Temperature of water bath: 35 ± 1 °C
- Laser pulse energy at sample surface: 32mJ (532nm) and 13mJ (750nm)

After the experiment, the complete agar phantoms were cryogenically preserved at -22°C. For validation purposes, they were subsequently cryosliced and partly saved for immunohistochemistry. The thereby acquired pictures may have elevational offsets of max. 500µm with respect to the optoacoustic images and shall only indicate roughly ground truth. All optoacoustic images show a 6x6mm field of view.

Results

The imaged Gammarus was ca. 1cm long and less than 2mm wide. By regarding a slice from approximately the tail region of the Gammarus, a first impression of the system performance for imaging Gammarus was obtained. In the tail region, there were no anatomic irregularities such as legs and other extremities, so that the amount of (expected) light and sound scattering artifacts was minimized. Illumination wavelength was 532nm and the unfiltered signal acquired by the PNDT V319 was used for reconstruction by backprojection. To use the unfiltered data was advantageous in the case of large offsets between two tomographic slices, because filtering the signal restricted the transversal field of view, thus complicating validation. The optoacoustic images illustrate slices of up to 350µm thickness. Though the image of the frozen Gammarus (see Fig. 7.11) did not show many details, some features like the gap in the dorsal area could be validated. Fig. 7.12, illustrates a comparison of cryoslice images and the corresponding OAT images for both used illumination wavelengths.

Due to speed of sound inhomogeneities within the Gammarus, the reconstruction needed to be adapted on a slice-to-slice basis. The automatic white balance of the cryoslicing system

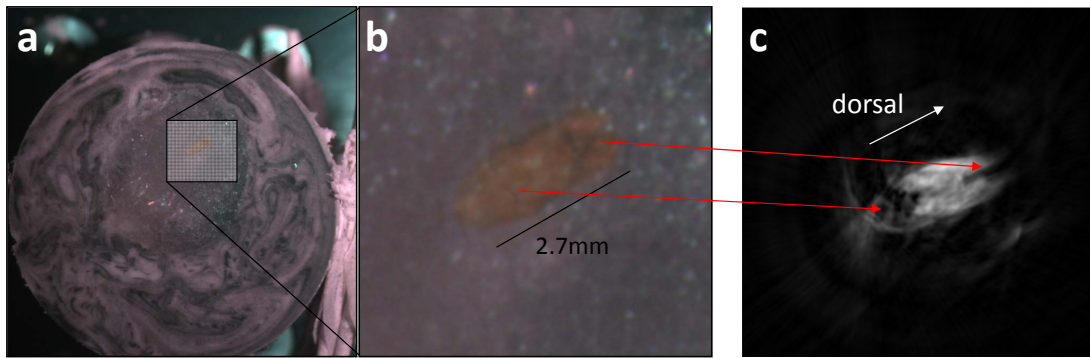


Figure 7.11: Cryoslice images (a,b) at of the tail region and corresponding optoacoustic image (c).

did not recognize the very small Gammarus, leading to color casts in the images, but which was meaningless for the validation purpose. The cryoslice images were contrast-enhanced. On the side of the optoacoustic tomography, the inherent problem of gray background that arose from the backprojection algorithm was suppressed by background subtraction. A resulting whole body scan is illustrated in Fig. 7.12.

Discussion

The optoacoustic scan of the Gammarus (see Fig. 7.12) was directed from head ($z=0$) to tail. At first, only the two antennas of the Gammarus were observed. Imaging deeper, after about $500\mu\text{m}$ the head appeared, including legs oriented anteriorly during. Especially the region of the body and tail were confirmed by the cryoslice images: Resemblance showed, e.g., in the orientation and position of the legs, stronger and weaker absorbing regions and the contour lines. Overall, also the transversal length of the organism was the same in both modalities.

For five exemplary positions, the illumination wavelength was set to 750nm . Those images also supported the images acquired at 532nm , although the background subtraction caused slight differences in the contour lines. The contrast arose from structures of another color, and light propagation also differed. Nevertheless, some structures were present at both wavelengths - typically those having rather flat absorption spectra.

It would be possible to increase the three-dimensionality by acquiring a larger amount of slices and high-pass filtering the signal before the reconstruction. Furthermore, it would be interesting to investigate why in some cases, especially in the head region, the above shown

images of cryoslices and optoacoustic tomography differ width-wise. This may be simply due to repositioning during the freezing procedure, but it may also result from a strong difference in the speed of sound of water versus the Gammarus head tissue. Further experiments, for instance investigating the speed of sound in the Gammarus, would help to clarify this issue.

7.1.5 Kidney nerve of a pig

In this very general proof-of-principle investigation, a part of a pig containing a kidney nerve was investigated. Apart of biological topics of interest, which shall not be discussed herein, the goal of this experiment was to quickly obtain three-dimensional information about the part containing the nerve, and thereby indicating the "plug and play" capabilities of the fiber-bundle-based ring illuminator (see section 4.3.2). The experimental procedure was, therefore, as simple as plugging the phantom of 16mm diameter containing the part of the pig (held by a simple phantom holder made of PMMA) into the system and scanning it at a fixed illumination wavelength, herein 532nm. Without discussing the results in detail, Fig. 7.13 shows a comparison of an exemplary 2D slice of a stack of multiple slices with the corresponding cryoslice color and green channel image. The arrows in Fig. 7.13 indicate structures corresponding between the images acquired by the two modalities. Due to the contrast mechanism of optoacoustics, red appearing structures in the cryoslice color images (i.e. absorbing green) are likely to contain high blood concentrations and show high pixel intensities in the optoacoustic images. This is generally valid under the assumption that no light is transmitted in the cryoslicing approach ($T=0$).

7.2 Validation studies by micro-CT

As discussed in section 5.2.3, there is a lack of validation methods for high resolution optoacoustic imaging of, for example, mouse tumors. The method shall ideally not require any post-experimental processing of the mouse tumor, particularly no processing that may influence the appearance of the vasculature. (X-ray) micro-CT of vascular casts of the tumor have been employed for validations of the microvasculature [33] [91]. A similar approach, which, however, advantageously avoids perfusing the animal, is presented herein.

The entire processing of the sample occurred *post mortem* and *ex vivo* and after opto-acoustic experimentation. The method is based on staining of the tumor with iodine-based solutions by a process, which was described before [92] [93]. Subsequently to the sacrifice of the mouse, the tumor (with surrounding skin) was excised and submerged in 3%-formaline solution in a plastic Eppendorf vessel. A few days later, the tumor was scanned before staining, as well as at two time points during the staining process. Further details about the staining method and other experimental implementation details are provided in the Bachelor thesis of Marie-Christine Zdora [94]. For assessing the specificity of the staining method, a mouse ear was investigated in parallel. Even more than in the tumor, in the mouse ear the true path of the vasculature is well known, which facilitates further validation.

Fig. 7.14 shows the mouse ear at time points before, and after 15 minutes and 3 hours of staining. While before the staining, no vasculature appeared in the images, the contrast of the vasculature was well increased after 15 minutes of staining. The respective images showed multiple vessels and branching of the vessels, as indicated in tile b by arrows. When scanning through the ear from b1 to b4, b1 showed one exemplary vessel, b2 showed the branching point, and b3 showed the further expanding secondary vessels. The vessels appeared as dots in those cross-section images. Further along the scan direction, tile b4 showed multiple further vessels in significant contrast over the surrounding ear tissue. After 3 hours of staining, the contrast of the vessels over the surrounding ear tissue decreased again, indicating saturation of the unspecific dye in the tissue.

The A2780 tumor is illustrated in Figs. 7.15 and 7.16. Again, before the staining procedure, no vessel-specific contrast was observed (see Fig. 7.15). At the intermediate time point, however, initial contrast increase was revealed, albeit in the periphery of the tumor only. Images acquired after 3 days of staining are cropped to show only a portion of the tumor in elevation, without the skin appearing in the images. As shown in the figures, the skin absorbed a lot of dye as compared to the tumor tissue, indicated by intensities in the skin portion that were superior to those of the tumor tissue. In summary, the tumor fine structure, including the commonly known randomly oriented tumor vasculature and further tumor heterogeneity, is shown in the figures. To point out that the structures within the three-dimensionally rendered tumor images are indeed vasculature, Fig. 7.16 illustrates a zoom on the tumor together with a corresponding cross-section view of a slice within the volume-rendered region.

For comparison and confirmation of the findings of section 5.2, a 4T1 tumor was, furthermore, investigated. The results are shown as cross-sections in Fig. 7.17 and partial projections in Fig. 7.18. In good accordance with earlier findings, the tumor tissue did not show patches of large vasculature density as, for example, the above described A2780. Yet, the tumor's vascular architecture appeared in strong contrast to the background. The illustrated partial projection images indicate the shape of the blood vessels (MIP of limited depth). The identified structures are thereby reasonably confirmed to be blood vessels. Their shape follows the shape demonstrated in the literature (cf. chapter 6).

In conclusion, the presented method provides a precise, and in case of suited staining duration, quasi vessel-specific validation method for tumor vascularisation. Further developments may be directed at how to adapt the dye for *in vivo* application. Then it may become possible to use the same dye / contrast agent for *in vivo* optoacoustic imaging and *post mortem* validation of the optoacoustic images.

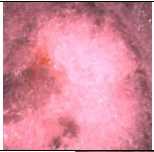
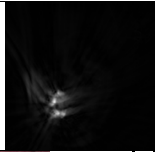
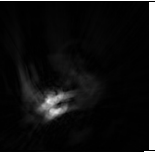
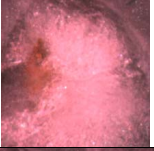
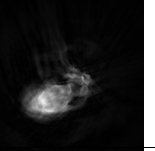
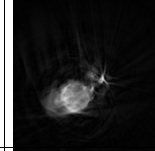
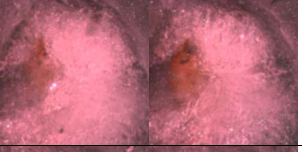
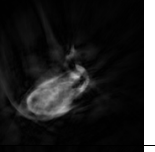
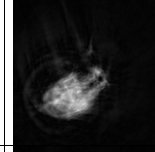
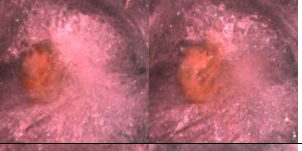
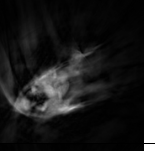
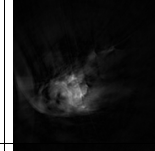
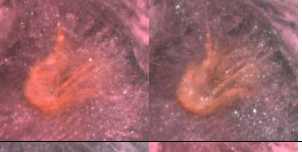
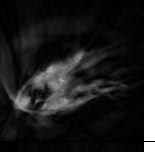
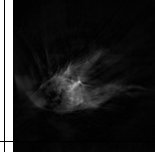
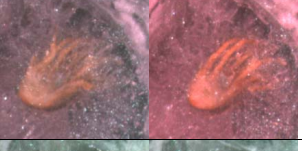
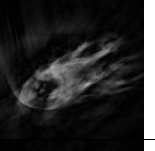
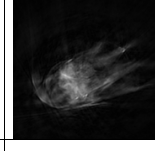

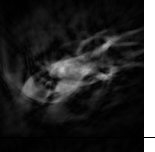
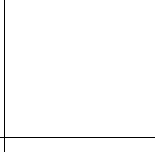

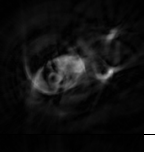
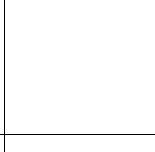
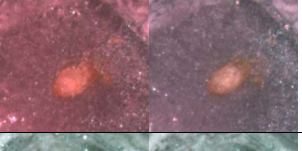
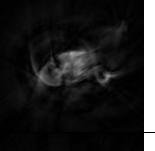
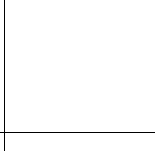

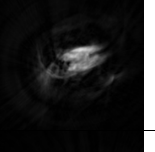
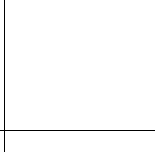
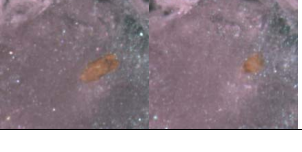

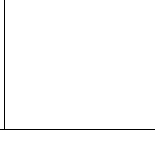
z / mm	Cryoslice	OAT 532nm	OAT 750nm
0			
0.5			
1 - 1.5			
2 - 2.5			
3 - 3.5			
4 - 4.5			
5 - 5.5			
6 - 6.5			
7 - 7.5			
8 - 8.5			
9 - 9.5			

Figure 7.12: Cryoslice images (left) of the Gammarus and corresponding optoacoustic image (right).

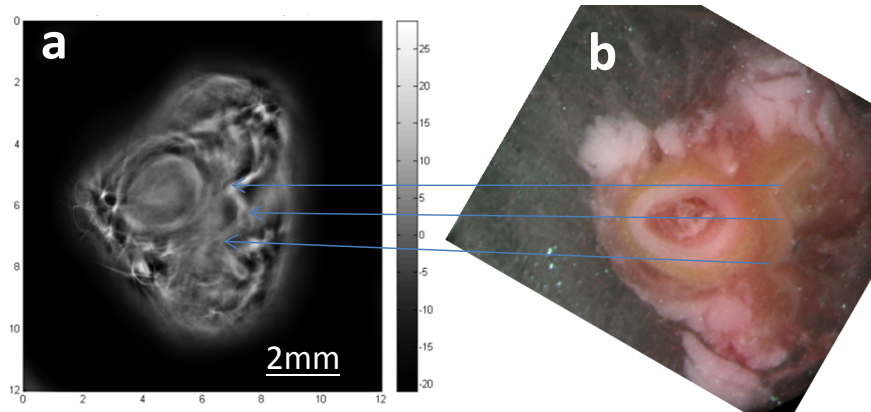


Figure 7.13: Proof-of-principle optoacoustic pig part (kidney nerve) imaging result. a: Optoacoustic image. b: Corresponding cryoslice color image.

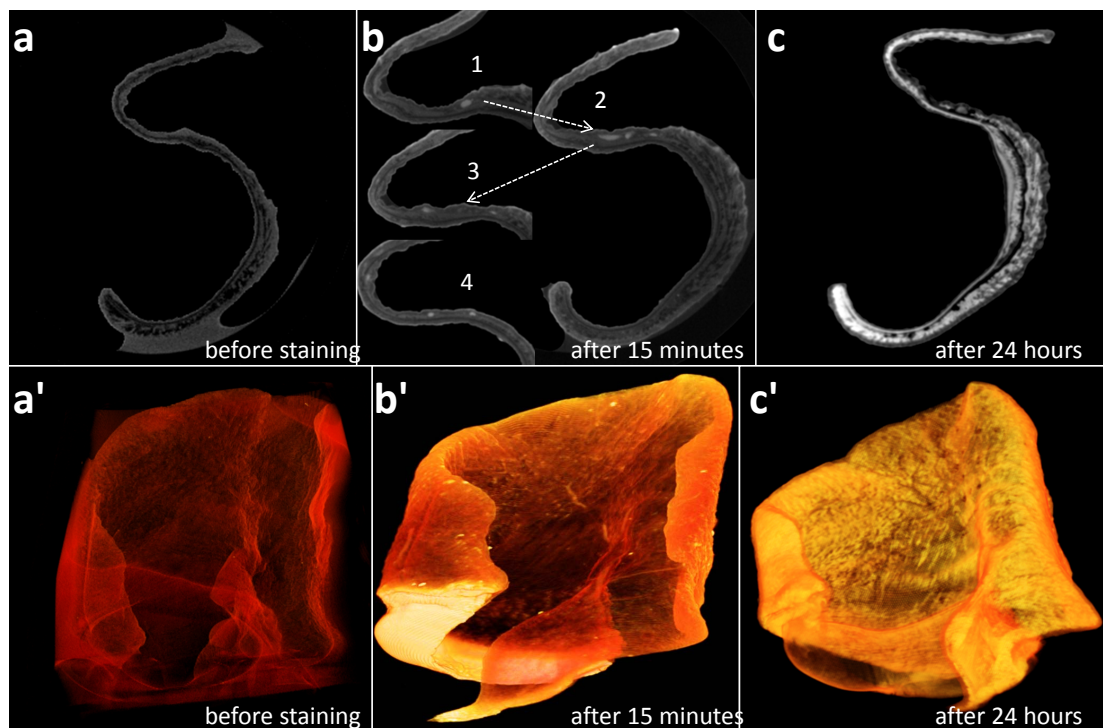


Figure 7.14: Mouse ear scanned by micro-CT at various time points of staining process (contrast agent: iodine-based solution). Top row: Tomography slices through the center of the ear. Bottom row: Three-dimensionally rendered entire mouse ears. Time points see images. b: Scan through the ear illustrates that the solution specifically increases the contrast of vessels for intermediate staining durations. c: Mouse ear saturated with staining solution.

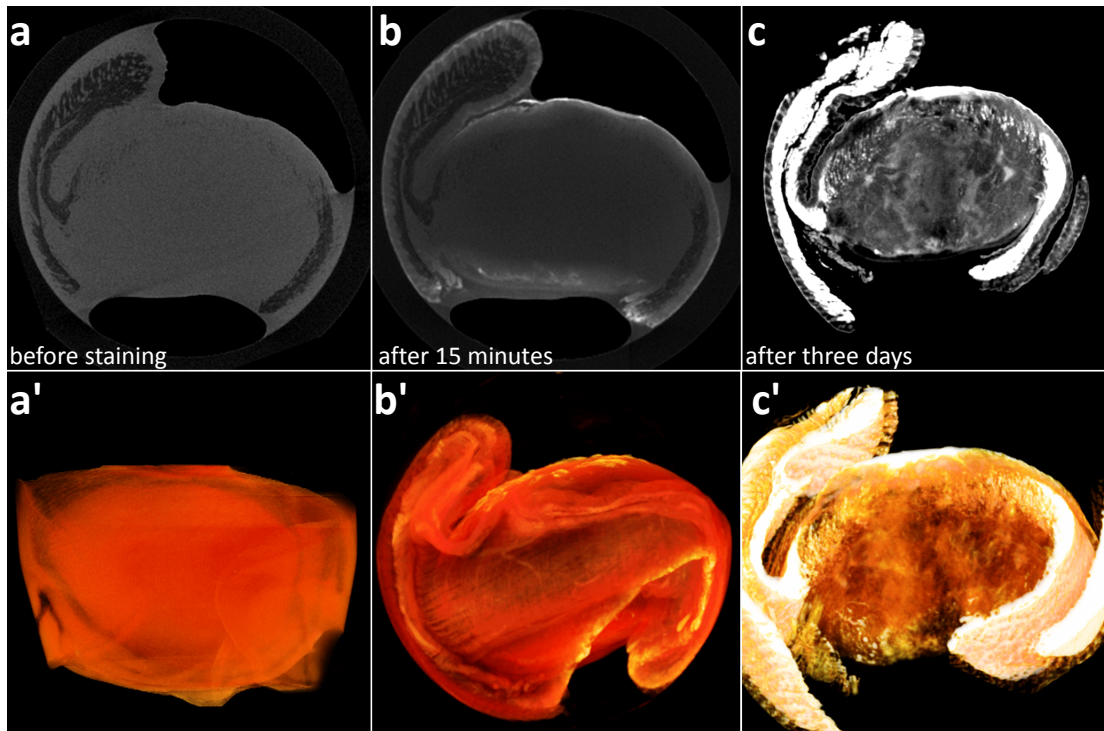


Figure 7.15: Ranged-out A2780 subcutaneous mouse tumor scanned by micro-CT at various time points of staining process (contrast agent: iodine-based solution). Top row: Tomography slices through the center of the tumor. Bottom row: Three-dimensionally rendered entire tumor. Time points see images. b: Scan through the ear illustrates that the solution specifically increases the contrast of vessels for intermediate staining durations. c: Tumor becoming saturated with staining solution, showing high contrast from parts of the vasculature.

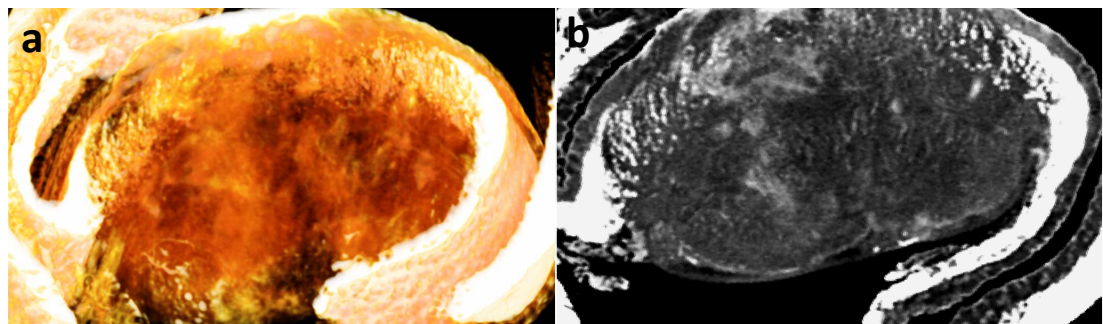


Figure 7.16: Zoom on the tumor shown in Fig. 7.15c illustrated by volume-rendering (a) and a corresponding cross-sectional view of a slice within the tumor region (b).

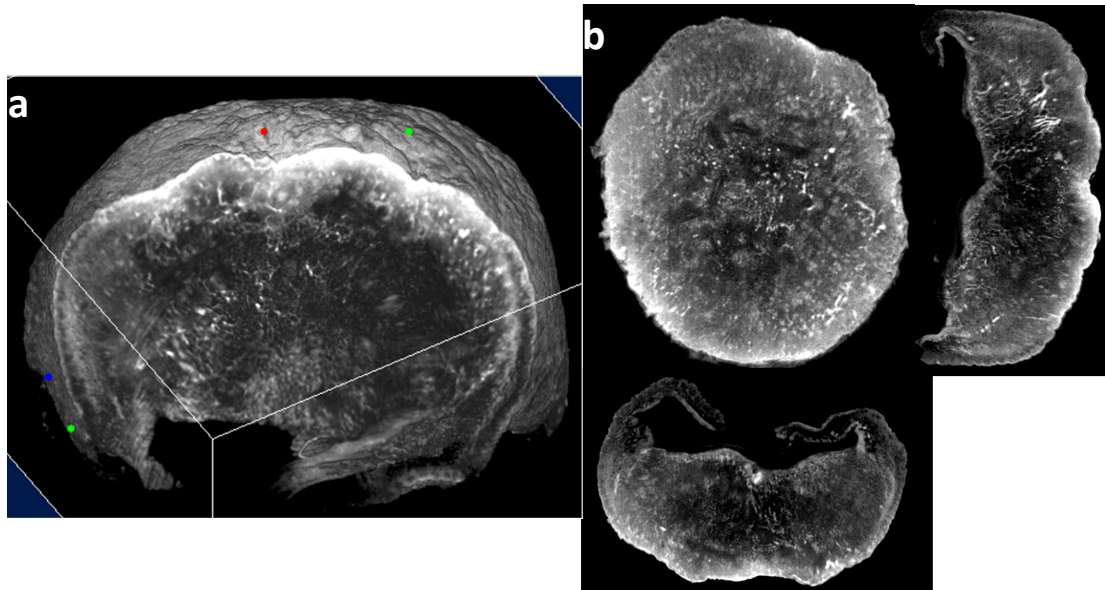


Figure 7.17: Micro-CT images of accurately stained 4T1 tumor. a: MIP of a central area within the tumor (depth of view is limited). b: Tomography of the center of the tumor.

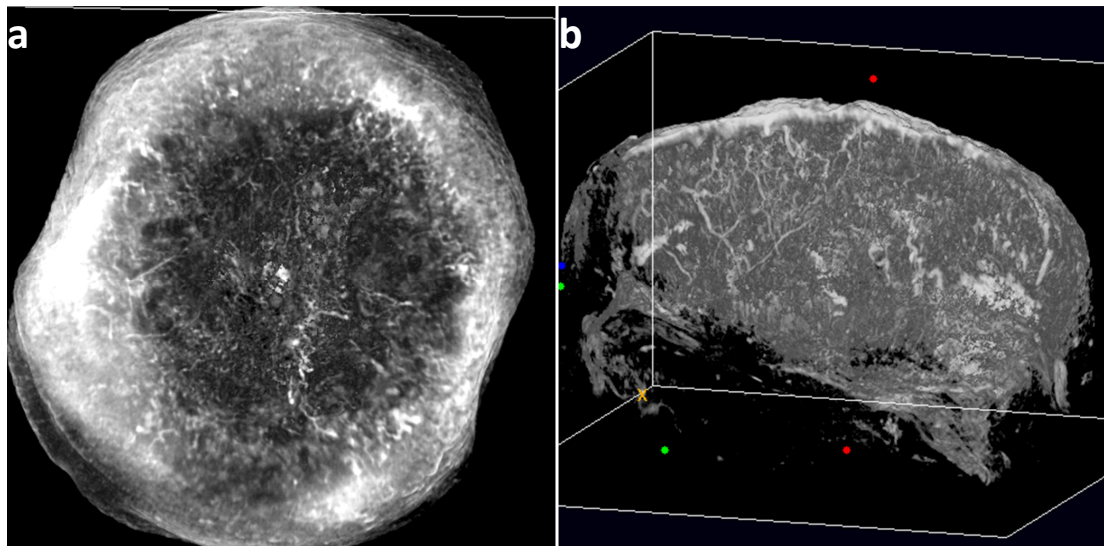


Figure 7.18: Three-dimensionally rendered 4T1 tumor calculated from micro-CT data. a: View from the top illustrating shape of vasculature. b: Cross-sectional view illustrating shape of vasculature.

Chapter 8

Conclusions and Outlook

8.1 Conclusions

In this work, I developed an optoacoustic imaging system for high resolution, non-invasive imaging of biological samples. The system was designed modularly, allowing for fast adaptation of illumination and scanning geometry to the specimen of interest. In a first step, the system's imaging performance was determined for various raster scanning and tomography configurations by means of phantom experiments and *post mortem* experiments with mice. The goal was to find an experimental configuration that would be well suited for biological investigations of subcutaneous mouse tumors (see chapters 4 and 5). Raster scanning proved to be advantageous with respect to implementing the experimental arrangement, as the tumor needed to be accessed only from one side. However, the point-focused transducers were required to be focused tightly enough, so that the depth of field would be in the range of a few hundreds of microns. At the current state of development, virtual detector techniques could also not extend the depth of field when imaging round tumors. Tomography, however, showed to be particularly advantageous due to elevation-independent tomographic in-plane resolution, meaning that the resolution was limited only by the frequency band of the transducer and the number of acquired projections. I, therefore, employed a cylindrically focused transducer (PNDT V319) sensitive to frequencies of up to 23MHz (resolution better than 32 μ m), to image the subcutaneous mouse tumors *in vivo* non-invasively. In phantom experiments (Fig. 4.14), the transducer showed to resolve structures as small as FWHM=55 μ m (true size 23 μ m).

In *post mortem* experiments (see chapter 5), the experimental arrangement was further optimized for tumor imaging, identifying a well-suited combination of tumor cell-line, mouse fixation, illumination and scanning geometry, as well as applicability of blood-pool contrast agents. From the set of investigated tumor cell lines, HT29 showed most intra-tumoral heterogeneities and least dermal damage of large grown tumors of up to 9mm diameter. 4T1, for instance, showed little intra-tumoral heterogeneities, rendering the validation of the optoacoustic results difficult. Also, the microvasculature of 4T1 showed to be finer, requiring higher imaging resolutions than the HT29. The combination of imaging with quasi-static illumination by the fiber-bundle-based ring illuminator (4.3.2), and the mouse positioned on its back, with the tumor fixed by the mouse's own body weight and hanging into the water, showed best results in *post mortem* imaging. On the other hand, planar illumination (single beam from the top of the tumor), for example, lead to strong out-of-plane signals causing ring artifacts when imaging the tumor at lower z-positions. Contrast increase by injection of blood-pool contrast agents showed to be peculiar in *post mortem* investigations, where the contrast agent is not renewed by blood circulation through the vessels. By investigating the fluorescence in the tumor, it was found that the contrast agent was bleached out during optoacoustic imaging. Detailed bleaching experiments have further proven that the bleaching half-live of potent contrast agents, such as ICG or Alexa Fluor 750, was much shorter than the necessary durations of optoacoustic experiments. Therefore, *in vivo* "renewal" of the contrast agents due to blood circulation through the tumor is generally required.

By optoacoustically imaging the tumor *in vivo* (cf. chapter 6), blood vessels with diameters of less than 17 μ m were clearly resolved (see Fig. 6.1) superficially up to deeply within the tumor. Vessel-specific contrast increase by a factor of two was achieved by injecting a gold nanorod suspension. Additional administration of Texas Red labeled tomato-lectin allowed the validation of the presence of microvasculature by fluorescence cryoslice imaging and microscopy. The results were three-dimensionally rendered to provide a profound view on the entire tumor vasculature. The structural appearance of the blood vessels *in vivo* showed strong improvement of contrast and clarity over the *post mortem* experiments. This difference is most probably attributed to the state of the organism (living vs. dead). One possible explanation for the structural differences between *post mortem* and *in vivo* imaging results regarding the shape of the vessels as a whole and of each of the vessels is the process of vaso-constriction. As soon as the heart of the mouse is at rest, the blood pressure rapidly decreases, leading to a narrowing of the blood vessels. This effect may, thus, be the reason for the vessels appearing

much thinner and even partly interrupted visually and in the optoacoustic images.

The validation methods applied in chapters 5 and 6 used gold standard optical imaging that is restricted by either lower resolutions or slice thicknesses in the range of 20 μm (cryosections). A volumetric validation of the tumor vasculature is thereby not provided. Yet, other state of the art validation methods also do not provide the necessary volumetric information. Therefore, the applicability of micro-CT as a potent volumetric validation method for optoacoustic tomography (of tumors) was investigated. The results presented in chapter 7 show that micro-CT imaging of *ex vivo* stained tumors offers precise structural details of the tumor vasculature, if the duration of the staining is chosen appropriately.

Although the optoacoustic setup was mainly developed for tumor imaging, the results presented in chapter 7 show that it is equally applicable for imaging other phantoms and biological samples, such as mouse ears, mouse head vasculature, 3mm long zebrafish, pig parts and Crustacea such as Gammarus. Owing to high tomographic in-plane resolution and setup geometry, the height of the sample (along the z-axis) plays only a marginal role.

8.2 Outlook

The field of applications of the developed optoacoustic system for mesoscopy could be particularly further extended by reducing acquisition times and increasing the imaging resolution, especially in elevational direction. To reduce acquisition times, multi-detector arrays have shown to be useful in comparable optoacoustic imaging of entire mouse bodies [43] [78]. Hence, a ring-shaped detector array of 180 elements could allow instantaneous acquisition of a single tomographic slice. Rotationally "wiggling" the detector by one degree would allow to easily increase the amount of projections, if necessary. The elevational resolution can be increased by detecting even higher frequencies, or focusing the transducer tighter (reducing the numeric aperture). Cylindrically focused transducers detecting higher frequencies can typically not be obtained "off the shelf", but have to be custom-made, applying new transducer technologies such as the thick-film technology. One such custom-made thick-film transducer was tested in this work (IS TF30), however, it had such a low sensitivity that it was not feasibly applicable for *in vivo* optoacoustic visualization of entire tumors, since it required too long acquisition times. Its sensitivity was more than one order of magnitude lower than the sensitivity

of the PNDT V319. Strong amplification of the transducer signal would allow overcoming those limitations. Tighter focusing is more difficult to implement, because the larger the element diameters or the shorter the focal lengths are, the more difficult it is to scan the transducer around the tumor.

Acquisition times may also be reduced while using single element transducers by scanning the transducers at higher velocities. This may be performed without Doppler-induced distortions, because Doppler effects will only become relevant at much higher scanning velocities (cf. [31]). A limitation that is complementary to the transducer sensitivity is the maximum permissible illumination intensity of laser light (MPE). It is wavelength-dependent, valuing $20\text{mJ}/\text{cm}^2$ at 532nm and throughout most of the visible spectral range. In the NIR, however, the MPE is much higher, valuing, for example, $100\text{mJ}/\text{cm}^2$ at 1064nm. If the light path through the coupling medium is sufficiently short in order to avoid absorption of the NIR light by the coupling medium, (e.g., by using silica fibers or fiber bundles), the low MPE limitation in the visible can be overcome by switching to said higher NIR wavelengths, allowing for even lower acquisition times and better vessel-specific contrast.

Universal backprojection showed to be well applicable for the tasks performed in this work. Therein, in order to accurately reconstruct the initial pressure distribution, the speed of sound or center of rotation in the region of interest (i.e. within the sample of interest) is typically evaluated separately for every image. To automatically determine the center of rotation, auto-focusing by optimizing the center of rotation for maximized image contrast could be employed. Preliminary tests, not further presented herein, showed promising results.¹

The tumor imaging experiments presented in this work are restricted to diagnosis of tumor vasculature at one time point. Longitudinal studies are, however, more relevant for biological studies. Other than most state of the art methods for the visualization of tumor vasculature development, the so called (neo-)angiogenesis, optoacoustics provides the option for *in vivo* experimentation. The method, therefore, enables such longitudinal studies along with tumor therapy studies. Instead of injecting a predetermined amount of tumor cells into mice, regularly measuring the size of the tumors while they grow, treating a subset of the mice with medication against tumor growth, and comparing the size-over-time graphs (growth curves) to indicate the

¹In a preliminary test, images' maximum pixel values showed to correlate well with to the accuracy of the center of rotation. The center of rotation may, hence, be optimized for the maximum pixel intensity of the reconstructed image.

effectiveness of the treatment, imaging the tumor throughout its development would be more efficient and ethically correct. Longitudinal studies are expected to provide more detailed insights on the biological processes. New, smaller optoacoustic systems derived from the system presented in this work could be developed specifically for large scale preclinical imaging of subcutaneous tumors, e.g., employing the above mentioned ring detector.

Bibliography

- [1] Alexander Graham Bell. Selenium and the photophone. *Nature*, -:500, 1880.
- [2] Alexander Graham Bell. Upon the production of sound by radiant energy. *Philosophical Magazine*, 11(68):510–528, 1881.
- [3] Rosencwaig et al. Photoacoustic spectroscopy. *Annual Reviews of Biophysics and Bio-engineering*, 9:31–54, 1980.
- [4] Rosencwaig et al. Photoacoustic spectroscopy of solids. *Optics Communications*, 7 (4):305–308, 1973.
- [5] Zharov and Letokhov. *Laser optoacoustic spectroscopy*. Springer-Verlag, 1986.
- [6] Patel et al. Pulsed optoacoustic spectroscopy of condensed matter. *Reviews of Modern Physics*, 53 (3):517–550, 1981.
- [7] Gu et al. Photoacoustic spectroscopy study on solid c60 in different crystalline states. *Solid State Communications*, 95(11):775–779, 1995.
- [8] Haiss et al. Light and sound - photoacoustic spectroscopy. *Spectroscopy Europe*, 14/5:10, 2002.
- [9] Patel et al. Laser photoacoustic spectroscopy helps fight terrorism: High sensitivity detection of chemical warfare agent and explosives. *European Physical Journal - Special Topics*, 153:1–18, 2008.
- [10] Träger et al. Infrared-laser photoacoustic spectroscopy for surface studies: S_f6 interaction with silver films. *Physical Review Letters*, 49:1720–1723, 1982.

- [11] Wickramasinghe et al. Photoacoustics on a microscopic scale. *Applied Physics Letters*, 33:923–925, 1978.
- [12] Martin et al. Photodisplacement techniques for defect detection. *Philosophical Transactions of the Royal Society London A*, 320:257–260, 1986.
- [13] Yeatman et al. Surface plasmon microscopy. *Electronics Letters*, 23 (20):1091–1092, 1987.
- [14] Ameri et al. Photo-displacement imaging. *Electronics Letters*, 17 (10):337–338, 1981.
- [15] McDonald et al. Photoacoustic, photothermal and related techniques. *Canadian Journal of Physics*, 64 (9):1023–1029, 1986.
- [16] Nakata et al. Real-time photodisplacement microscope for high-sensitivity simultaneous surface and subsurface inspection. *Applied Optics*, 45 (2):2643–2655, 2006.
- [17] Oraevski et al. Determination of tissue optical properties by piezoelectric detection of laser-induced stress waves. *Proc. of SPIE*, 1882:86, 1993.
- [18] Esenaliev et al. Sensitivity of laser opto-acoustic imaging in detection of small deeply embedded tumors. *IEEE Journal of Selected Topics in Quantum Electronics*, 5 (4):981–988, 1999.
- [19] Esenaliev et al. Optoacoustic technique for noninvasive monitoring of blood oxygenation: a feasibility study. *Applied Optics*, 42(22):4722–4731, 2002.
- [20] Razansky et al. Multispectral photoacoustic imaging of fluorochromes in small animals. *Optics Letters*, 32(19):2891–2893, 2007.
- [21] Wang et al. Multiscale photoacoustic microscopy and computed tomography. *Nature Photonics*, 3:503, 2009.
- [22] Zhang et al. In vivo high-resolution 3d photoacoustic imaging of superficial vascular anatomy. *Physics in Medicine and Biology*, 54:1035, 2009.
- [23] Tuan Vo-Dinh. *Biomedical Photonics Handbook*. CRC Press, 2003.
- [24] Ntziachristos. Going deeper than microscopy: the optical imaging frontier in biology. *Nature Methods*, 7(8):603–614, 2010.

- [25] Li et al. Visualization of hypoxia in microscopic tumors by immunofluorescent microscopy. *Cancer Research*, 67:7646–7653, 2007.
- [26] van Dam et al. Intraoperative tumor-specific fluorescence imaging in ovarian cancer by folate receptor- α targeting: first in-human results. *Nature Medicine*, 17(10):1315–1320, 2011.
- [27] Jain et al. Delivery of molecular and cellular medicine to solid tumors. *Microcirculation*, 4(1):1–23, 1997.
- [28] Vakoc et al. Three-dimensional microscopy of the tumor microenvironment in vivo using optical frequency domain imaging. *Nature Medicine*, 15:1219–1223, 2009.
- [29] Farrar et al. In vivo validation of mri vessel caliber index measurement methods with intravital optical microscopy in a u87 mouse brain tumor model. *Neuro-Oncology*, 12(4):341–350, 2010.
- [30] Willmann et al. Molecular imaging in drug development. *Nature Reviews Drug Discovery*, 7:591–607, 2008.
- [31] Ma et al. Multispectral optoacoustic tomography (msot) scanner for whole-body small animal imaging. *Optics Express*, 17(24):21414–21426, 2009.
- [32] Zhang. Functional photoacoustic microscopy for high-resolution and noninvasive in vivo imaging. *Nature Biotechnology*, 24:848–851, 2003.
- [33] Laufer et al. In vivo longitudinal photoacoustic imaging of subcutaneous tumors in mice. *Proceedings of SPIE*, 7899:789915, 2011.
- [34] Yeqi Lao et al. Noninvasive photoacoustic imaging of the developing vasculature during early tumor growth. *Physics in Medicine and Biology*, 53:4203–4212, 2008.
- [35] Karabutov et al. Backward mode detection of laser-induced wide-band ultrasonic transients with optoacoustic transducer. *Journal of Applied Physics*, 84(4):2003–2014, 2000.
- [36] Wu Wang. *Biomedical Optics - Principles and Imaging*. John Wiley & Sons, Inc., Hoboken, New Jersey, 2007.
- [37] Wang. *Photoacoustic Imaging and Spectroscopy*. CRC Press, 2009.

- [38] Thomas L. Szabo. *Diagnostic Ultrasound Imaging: Inside Out*. Elsevier Academic Press, 2004.
- [39] B. A. J. Angelsen. *Ultrasound Imaging*. Emantec AS, Trondheim, Norway, 2000.
- [40] Horst Kuchling. *Taschenbuch der Physik*. Fachbuchverlag Leipzig im Carl Hanser Verlag, 2004.
- [41] Prof. Dr. Rudolf Gross. Physik 3 - optik und quantenphaenomene. Online, March 2003.
- [42] Razansky et al. Hybrid photoacoustic fluorescence molecular tomography using finite-element-based inversion. *Medical Physics*, 34(11):4293, 2007.
- [43] Taruttis et al. Real-time imaging of cardiovascular dynamics and circulating gold nanorods with multispectral photoacoustic tomography. *Optics Express*, 18:19592–19602, 2010.
- [44] Xu and Wang. Universal back-projection algorithm for photoacoustic computed tomography. *Physical Review E*, 71:016706, 2005.
- [45] Rozenal et al. Fast semi-analytical model-based acoustic inversion for quantitative photoacoustic tomography. *IEEE Transactions on Medical Imaging*, 29(6):1275, 2010.
- [46] Glatz et al. Blind source unmixing in multi-spectral photoacoustic tomography. *Optics Express*, 19(4):3175–3184, 2011.
- [47] Olympus NDT Inc., Waltham, MA 02453, USA. *Panametrics Ultrasonic Transducers*, 2009.
- [48] Kak and Slaney. *Principles of Computerized Tomographic Imaging*. IEEE Press, 1987.
- [49] Jetzfellner et al. Photoacoustic tomography with varying illumination and non-uniform detection patterns. *Journal of the Optical Society of America A*, 27(11):2488–2495, 2010.
- [50] Buehler et al. Video rate photoacoustic tomography of mouse kidney perfusion. *Optics Letters*, 35:2475–2477, 2010.
- [51] Li et al. Improved in vivo photoacoustic microscopy based on a virtual-detector concept. *Optics Letters*, 31:474–476, 2006.

- [52] Liao et al. Optoacoustic imaging with synthetic aperture focusing and coherence weighting. *Optics Letters*, 29(21):2506–2508, 2004.
- [53] Frazier et al. Synthetic aperture techniques with a virtual source element. *IEEE Transactions on ultrasonics, ferroelectrics, and frequency control*, 45(1):196–207, 1998.
- [54] Dean Ben et al. Statistical approach for optoacoustic image reconstruction in the presence of strong acoustic heterogeneities. *IEEE Transactions on Medical Imaging*, 30:401, 2011.
- [55] Xiang et al. Real-time optoacoustic monitoring of vascular damage during photodynamic therapy treatment of tumor. *Journal of Biomedical Optics*, 12:014001, 2007.
- [56] Zhang et al. Noninvasive photoacoustic imaging of the developing vasculature during early tumor growth. *Nature Biotechnology*, 24:848–851, 2006.
- [57] Ansi-Standards. American national standards for the safe use of lasers in health care facilities (standard z136.1). Technical report, American National Standards Institute, 2000.
- [58] Ku et al. Imaging of tumor angiogenesis in rat brains in vivo by photoacoustic tomography. *Applied Optics*, 44:770–775, 2005.
- [59] Lungu et al. In vivo imaging and characterization of hypoxia-induced neovascularization and tumor invasion. *International Journal of Oncology*, 30:45–54, 2007.
- [60] Maslov et al. Optical-resolution photoacoustic microscopy for in vivo imaging of single capillaries. *Optics Letters*, 33:929–931, 2008.
- [61] Xie et al. Laser-scanning optical-resolution photoacoustic microscopy. *Optics Letters*, 34(12):1771–1773, 2009.
- [62] Muller, editor. *Laser-Induced Interstitial Thermotherapy*, volume PM25, 1995.
- [63] Kang et al. Quantitative analysis of peripheral tissue perfusion using spatiotemporal molecular dynamics. *PLoS ONE*, 4:e4275, 2009.
- [64] Dickerson et al. Gold nanorod assisted near-infrared plasmonic photothermal therapy (pptt) of squamous cell carcinoma in mice. *Cancer Letters*, 269:57–66, 2008.

- [65] Sarantopoulos et al. Imaging the bio-distribution of fluorescent probes using multispectral epi-illumination cryoslicing imaging. *Molecular Imaging and Biology*, 13:874–885, 2010.
- [66] Newman. The role of pecam-1 in vascular cell biology. *Annals New York Academy of Sciences*, 1:165–174, 1994.
- [67] Torzicky. Platelet endothelial cell adhesion molecule-1 (pecam-1/cd31) and cd99 are critical in lymphatic transmigration of human dendritic cells. *Journal of Investigative Dermatology*, 132(4):1149–57, 2011.
- [68] Delfortrie. Egfl7 promotes tumor escape from immunity by repressing endothelial cell activation. *Cancer Research*, 71:7176–7186, 2011.
- [69] Baker et al. Irinophore c, a novel nanoformulation of irinotecan, alters tumor vascular function and enhances the distribution of 5-fluorouracil and doxorubicin. *Clinical Cancer Research*, 14:7260–7271, 2008.
- [70] Jain et al. Dissecting tumour pathophysiology using intravital microscopy. *Nature Reviews Cancer*, 2:266–276, 2002.
- [71] Kiessling et al. Volumetric computed tomography (vct): a new technology for noninvasive, high-resolution monitoring of tumor angiogenesis. *Nature Medicine*, 10:1133–1138, 2004.
- [72] Sipkinns et al. Detection of tumor angiogenesis in vivo by avb3-targeted magnetic resonance imaging. *Nature Medicine*, 4:623–626, 1998.
- [73] Mikhaylov et al. Ferri-liposomes as an mri-visible drug-delivery system for targeting tumours and their microenvironment. *Nature Nanotechnology*, 6:594–602, 2011.
- [74] Cai et al. Magnetic resonance imaging of glutamate. *Nature Medicine*, 18:602–606, 2012.
- [75] Kirsch et al. A spatially and temporally restricted mouse model of soft tissue sarcoma. *Nature Medicine*, 13:992–997, 2007.
- [76] Backer et al. Molecular imaging of vegf receptors in angiogenic vasculature with single-chain vegf-based probes. *Nature Medicine*, 13:504–509, 2007.

- [77] Weissleder et al. Shedding light onto live molecular targets. *Nature Medicine*, 9:123 – 128, 2003.
- [78] Taruttis et al. Fast multispectral optoacoustic tomography (msot) for dynamic imaging of pharmacokinetics and biodistribution in multiple organs. *PLoS ONE*, 7:30491, 2012.
- [79] Kim et al. In vivo photoacoustic tomography of chemicals high-resolution functional and molecular optical imaging at new depths. *Chemical Reviews*, 110:2756–2782, 2010.
- [80] Razansky et al. Multispectral opto-acoustic tomography of deep-seated fluorescent proteins in vivo. *Nature Photonics*, 3:412–417, 2009.
- [81] Alekseev et al. Reflection and penetration of millimeter waves in murine skin. *Bioelectromagnetics*, 29:340–344, 2008.
- [82] Wang et al. Photoacoustic tomography of a nanoshell contrast agent in the in vivo rat brain. *Nano Letters*, 4:1689–1692, 2004.
- [83] Konerding et al. 3d microvascular architecture of precancerous lesions and invasive carcinomas of the colon. *British Journal of Cancer*, 84:1354–1362, 2001.
- [84] Zhang et al. Inhibition of proliferation of prostate cancer cell line pc-3 in vitro and in vivo using -gossypol. *Asian Journal of Andrology*, 12:390–399, 2010.
- [85] Jin et al. A superficial colon tumor model involving subcutaneous colon translocation and orthotopic transplantation of green fluorescent protein-expressing human colon tumor. *Journal of Carcinogenesis and Mutagenesis*, 1:1000104, 2010.
- [86] Ellis et al. Down-regulation of vascular endothelial growth factor in a human colon carcinoma cell line transfected with an antisense expression vector specific for c-src. *The Journal of Biological Chemistry*, 273:1052–1057, 1998.
- [87] Prewett et al. Enhanced antitumor activity of anti-epidermal growth factor receptor monoclonal antibody imc-c225 in combination with irinotecan (cpt-11) against human colorectal tumor xenografts. *Clinical Cancer Research*, 8:994–1003, 2002.
- [88] Laufer et al. In vivo preclinical photoacoustic imaging of tumor vasculature development and therapy. *Journal of Biomedical Optics*, 17:056016, 2012.
- [89] Wang et al. Noninvasive laser-induced photoacoustic tomography for structural and functional in vivo imaging of the brain. *Nature Biotechnology*, 21:803–806, 2003.

- [90] Monash University. <http://www.fishnet.org.au>.
- [91] Grabherr et al. Angiofil-mediated visualisation of the vascular system by microcomputed tomography. a feasibility study. *Microscopy Research and Technique*, 71:551–556, 2008.
- [92] Brian Metscher et al. Microct for developmental biology: A versatile tool for high-contrast 3d imaging at histological resolutions. *DEVELOPMENTAL DYNAMICS*, 238:632–640, 2009.
- [93] Metscher et al. Microct for comparative morphology: simple staining methods allow high-contrast 3d imaging of diverse non-mineralized animal tissues. *BMC Physiology*, 9:11, 2009.
- [94] Marie-Christine Zdora. *Evaluation of staining protocols for improved soft tissue contrast in absorption-based microCT*. PhD thesis, Technische Universität München - Fakultät für Physik, 2011.
- [95] Herzog et al. Optical imaging of cancer heterogeneity with multispectral optoacoustic tomography. *Radiology*, 263:461–8, 2012.
- [96] Müller et al. Image scanning microscopy. *Physical Review Letters*, 104 (19):198101, 2010.
- [97] John Annegers. A study of total body water in rats and mice. Technical report, Naval Medical Research Institute (U.S.), 1954.
- [98] James G. Fox. *The Mouse in Biomedical Research: Normative Biology, Husbandry, and Models*. Academic Press, 2007.
- [99] Oregon Medical Laser Center Scott Prahl. Optical absorption of hemoglobin. <http://omlc.ogi.edu/spectra/hemoglobin/index.html>, 12 1999.
- [100] Precision Acoustics Ltd., Hampton Farm Business Park, Higher Bockhampton, Dorchester, UK. *HP Series High Performance Hydrophone Measurement System*.
- [101] Wasser-eigenschaften: Absorption von elektromagnetischer strahlung. http://www.wissenschaft-technik-ethik.de/wasser_eigenschaften.html, 2006.

List of Figures

2.1	Schematic of a thick spherical lens (n_2).	11
2.2	Schematic of a conical lens (axicon) with geometrical optics.	13
2.3	Fluence rate distribution in arbitrary units after initial injection of a photon package of energy E at $t=0$	16
3.1	Sensitivity field for the example of a cylindrically focused transducer.	23
3.2	Principle of the sum-and-delay algorithm.	26
4.1	Scheme of the developed scanning geometries indicating advantageous combinations of illumination and detection.	32
4.2	The open microscanning setup.	34
4.3	The scanner device.	35
4.4	The developed inhalation narcosis device	36
4.5	Internal design and beam profile of the Opotek Vibrant 532I laser system.	38
4.6	The wavelength dependent output energy (per pulse) of the OPOTEK Vibrant 532I laser system.	39

4.7	Sensitivity fields in Gaussian approximation.	41
4.8	Design of the (prototype) fiber bundle.	45
4.9	The mouse holders.	46
4.10	Exemplary implementation of the setup for free-beam four-side orthogonal in- imaging-plane illumination of the sample.	47
4.11	The fiber-bundle-based ring illuminator.	50
4.12	The confocal microscanning device.	52
4.13	Experimental arrangement for imaging the agar phantom with insertion in shape of a hexagon.	53
4.14	Imaging results of the phantom with hexagonal insertion.	55
4.15	Experimental arrangement for microscanning through a 7mm thick slab of turkey breast.	57
4.16	Results for microscanning through a 7mm thick slab of turkey breast.	58
4.17	Results for microscanning a cross printed on paper.	59
4.18	Photographs of the samples for confocal point raster scanning.	60
4.19	Results of confocal point raster scanning.	61
5.1	Photographs of solid subcutaneous tumors, i.e., subjects of interest.	66
5.2	Experimental arrangements for determining the speed of sound in tumor tissue optoacoustically and and for determining qualitative wavelength dependence of attenuation in mouse skin.	67
5.3	RGB decomposition of photograph (reflection image) of a tumor and surround- ing skin under white light illumination on a white table.	70

5.4	Spectra of ICG, AF750, and Gold Nanorods after illumination at peak wavelength in dependence of deposited energy (photobleaching).	72
5.5	Configurations of the optoacoustic system (scanning device) for <i>post mortem</i> imaging of tumors.	75
5.6	Temporal dependencies of tumor sizes during growth processes.	79
5.7	Optoacoustic imaging and validation results for HT29 tumor scanned in system configuration I.	80
5.8	Optoacoustic imaging and validation results for 4T1 tumor scanned in system configuration I.	81
5.9	Optoacoustic imaging and validation results for HT29 tumor scanned in system configuration I with homogeneous unidirectional illumination.	83
5.10	Optoacoustic imaging and validation results for 4T1 tumor scanned in system configuration I.	84
5.11	Optoacoustic tomography stack of the entire 4T1 tumor (up to 4mm below the top of the tumor) scanned in system configuration I with 532nm illumination.	91
5.12	Optoacoustic imaging and validation results for HT29 tumor scanned in system configuration II.	92
5.13	Optoacoustic imaging and validation results for 4T1 tumor scanned in system configuration II.	93
5.14	Fluorescence cryoslice images showing the photobleaching of the contrast agent Angiosense750 in the tumor.	94
6.1	Intrinsic contrast optoacoustic imaging of tumor vascularisation.	101
6.2	Signal and contrast increase by injection of gold nanorods.	103

6.3	Profound imaging of tumor vasculature.	105
6.4	Intensity profile across tumor vasculature.	106
6.5	Three-dimensionally rendered shape of the tumor blood vasculature.	107
7.1	Optoacoustic tomography of mouse head vasculature.	113
7.2	Superficial imaging of the microvasculature of a 4T1 tumor.	114
7.3	Transparent agar phantoms with 3.5mm long zebrafish.	116
7.4	Optoacoustic images of 3.5mm long zebrafish reconstructed by backprojection of unprocessed signals at 532nm (a) and 740nm (b) illumination wavelength.	117
7.5	Projection images (optoacoustic, light microscopy and fluorescence microscopy) of the 3.5mm long zebrafish	118
7.6	Validation: Optical Projection Tomography (OPT) images of a 96 hours old zebrafish.	118
7.7	Optoacoustic images of the zebrafish at various illumination wavelengths.	119
7.8	Multispectral decomposition showing the general distribution of three compo- nents with different absorption spectra of which two resemble those of oxy- genated and deoxygenated hemoglobin.	120
7.9	Multispectral decomposition of the images shown in Fig. 7.7 with correspond- ing absorption spectra.	120
7.10	Optoacoustic tomographic image stack as coronal view with an exemplary val- idation of the fine-structure of the zebrafish tail.	121
7.11	Cryoslice stack of Gammarus I.	123
7.12	Cryoslice stack of the Gammarus II.	127

7.13	Proof-of-principle optoacoustic pig part (kidney nerve) imaging result.	128
7.14	Mouse ear scanned by micro-CT at various time points of staining process (contrast agent: iodine-based solution).	128
7.15	Ranged-out A2780 subcutaneous mouse tumor scanned by micro-CT at various time points of staining process (contrast agent: iodine-based solution).	129
7.16	Zoom on stained tumor imaged by micro-CT.	129
7.17	Micro-CT images of accurately stained 4T1 tumor.	130
7.18	Three-dimensionally rendered 4T1 tumor calculated from micro-CT data.	130
A.1	Light absorption in water.	149
A.2	Light absorption by oxygenated and deoxygenated hemoglobin.	150
A.3	Optoacoustic imaging with a PVDF detector.	152
A.4	Blood oxygenation derived by linear multispectral decomposition.	153

Appendix A

Appendix

A.1 Light absorption by water and blood

In chapter 2 of this thesis, the physical effects along the path of light propagation from the laser to the sample are discussed. In addition to reflections at media boundaries, attenuation (here: absorption) of light has to be taken into account when NIR light travels through water. The light

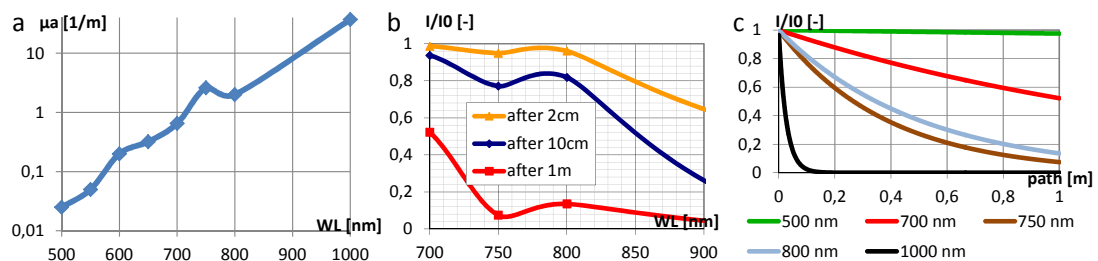


Figure A.1: Light absorption in water in various representations. The graphs are reconstructed with data published in [101].

absorption in water is illustrated in Fig. A.1. The graphs are reconstructed with data published in [101]. As Fig. A.1a shows, the light absorption increases exponentially with the wavelength. Further shown in Figs. A.1b-c, light paths through the coupling medium (herein: water) have to be particularly short when intending to image the sample with NIR illumination. In water, for example, already after a path length of 10cm the light intensity is reduced to less than a quarter of the initial intensity. Consequently, in the NIR, wavelength-dependent irradiance corrections have to be applied, whereas those corrections are irrelevant at 532nm illumination.

Further considering that the water content of a mouse values between 70% and 78% of the

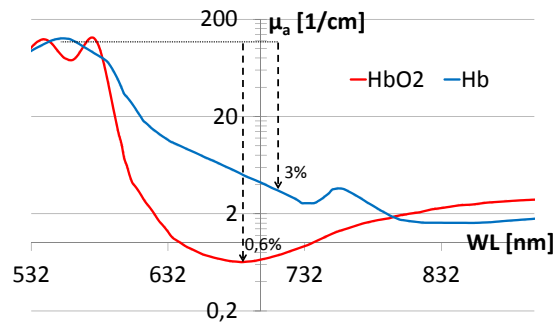


Figure A.2: Light absorption by oxygenated and deoxygenated hemoglobin.

mouse's body weight [97] [98], imaging in the NIR, e.g. at 1064 nm illumination wavelength, the shown spectral dependence of the absorption by water allows for optoacoustic imaging of the water distribution in the mouse, whereby the water distribution typically correlates with optical (visible) contrast: for example, blood has high water content of over 90%, whereas bone has low water content of less than 30%.

For completeness, the absorption spectra of oxygenated hemoglobin and deoxygenated hemoglobin are reproduced after [99] and the results are illustrated in Fig. A.2. The graph shows that absorption by hemoglobin, the chromophore of blood, is about two orders of magnitude lower in the NIR than at 532nm.

A.2 PZT and PVDF ultrasonic detectors for optoacoustic imaging - a phenomenological comparison

These two detector element materials were of highest relevance for the optoacoustic imaging tasks presented in this thesis: the piezoelectric ceramic (PZT: lead-zirconate-titanate) and the piezoelectric organic polymers (PVDF: poly-vinyl-inden-fluoride). I herein shortly discuss findings that lead to the decision to use PZT transducers for tumor and other biological imaging, as presented in chapters 5, 6, and 7. For further details about transducer technology, the reader is referred to [100] and [38]. The performance of PZT transducers, such as the PNDT V319 or V320, and applicability to tumor imaging is discussed in section 4.4.1 of this thesis. To find out if images of similar or better quality can be obtained with suitable PVDF ultrasonic detectors that have comparable hardware characteristics, the phantom experiment discussed in section

4.4.1 was repeated with such a PVDF detector.

Method. A custom-made, cylindrically focused PVDF detector (element size: 7.5mm x 2.5mm, focal length: 15mm, Precision Acoustics, Dorchester, United Kingdom) is tomographically scanned around an agar phantom with optical and acoustic properties as described in section 4.4.1, albeit with the insertion being 6mm wide. The experimental arrangement and procedure is identical to the experimental arrangement and procedure presented in section 4.4.1. Unlike the PZT transducer, the herein employed PVDF detector requires the use of a submersible preamplifier (8dB voltage gain). The nominal detection band extends from 10kHz to 60MHz.

Results. Fig. A.3 shows optoacoustic images of the agar phantom. By performing the reconstruction with unfiltered signal (Fig. A.3a-c), one can observe the hexagonal shape of the insertion and the circular shape of the background, however, all edges appear soft, when in fact they are sharp as presented in section 4.4.1. To bring up the fine structure of the phantom, reconstruction was also performed with signal high-passed at 2MHz (Fig. A.3d), filtering out large structures such as the bulk of the insertion. However, this resulted in an inaccurate visualization of the phantom. It was, hence, not possible with reasonable effort to optoacoustically image a simple tissue mimicking phantom as accurately or even more accurately by means of the representative PVDF detector than by the PNDT V319 PZT transducer.

Discussion. Caring to find the reason for the inaccuracy of the optoacoustic images acquired with the PVDF detector, we compared the spectral sensitivity of the representative PVDF detector (Fig. A.3e) with the spectral sensitivity of the comparable PNDT V319 PZT transducer (Fig. A.3f) [100]. Therein, it is shown that the sensitivity spectrum of the PVDF detector is not Gaussian, but rather exponentially decreasing up to about 23MHz, before it slightly increases again up to 30MHz. These sensitivity spectra are measured with calibrated sources of tunable frequencies. In optoacoustic imaging with unfocused detectors / transducers¹, another effect has to be taken into account, namely the true spectrum of the emitted pressure wave. Large absorbers will inherently produce large amplitudes of the sound wave. Therefore, if one spectrally

¹similar applies to cylindrically focused detectors / transducers, which are only focused in one direction, i.e., focused to a line

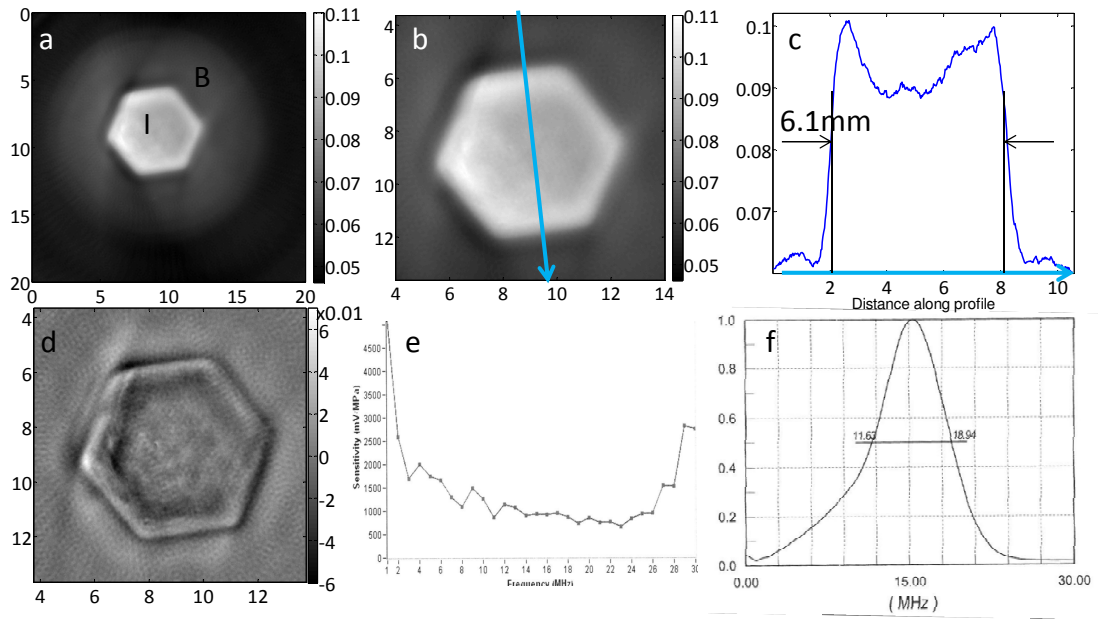


Figure A.3: Optoacoustic imaging with a PVDF detector. a-b: Optoacoustic tomography images of a phantom with background (B) and insertion (I). c: Line profile recorded along the arrow in (b). d: Optoacoustic tomography image reconstructed with high-pass filtered signal. e: Spectral sensitivity of the representative PVDF detector. f: Spectral sensitivity of the PNDT V319 PZT detector.

decomposes optoacoustic signal detected with an ideal detector that detects all frequencies with the same sensitivity, the spectral intensity will decrease with increasing frequencies. Detecting with the representative PVDF detector further amplifies this unwanted effect. PZT transducers, however, significantly equalize the lower intensities of the optoacoustic pressure wave at larger frequencies, resulting in a more thorough representation of the phantom. This effect is of particular relevance for tumor imaging, where heterogeneities of different sizes inside tumors shall be imaged. An additional advantage of the PZT transducers is the better SNR, so that a submersible preamplifier is not required.

A.3 Supplementary results on *in vivo* imaging of tumor vasculature

Spectral decomposition of the tumor vasculature images acquired by optoacoustic tomography at various illumination wavelength allowed to visualize the biodistribution of extrinsically administered contrast agents (gold nanorods). Intrinsic absorbers, such as oxygenated and deoxygenated hemoglobin, had been imaged by this method, determining the concentrations of

oxygenated and deoxygenated hemoglobin, albeit with lower resolution than achieved in this work (cf. [95]). As a side result of the investigations presented in chapter 6, obtained by linear decomposition as described in section 3.3.1, the oxy- and deoxyhemoglobin concentration in the tumor discussed in chapter 6 is shown qualitatively in Fig. A.4, allowing to resolve fine arteries appearing red and penetrating into the tumor along with veins appearing blue, *in vivo*. The raw direct results of plain backprojection reconstruction are also shown.

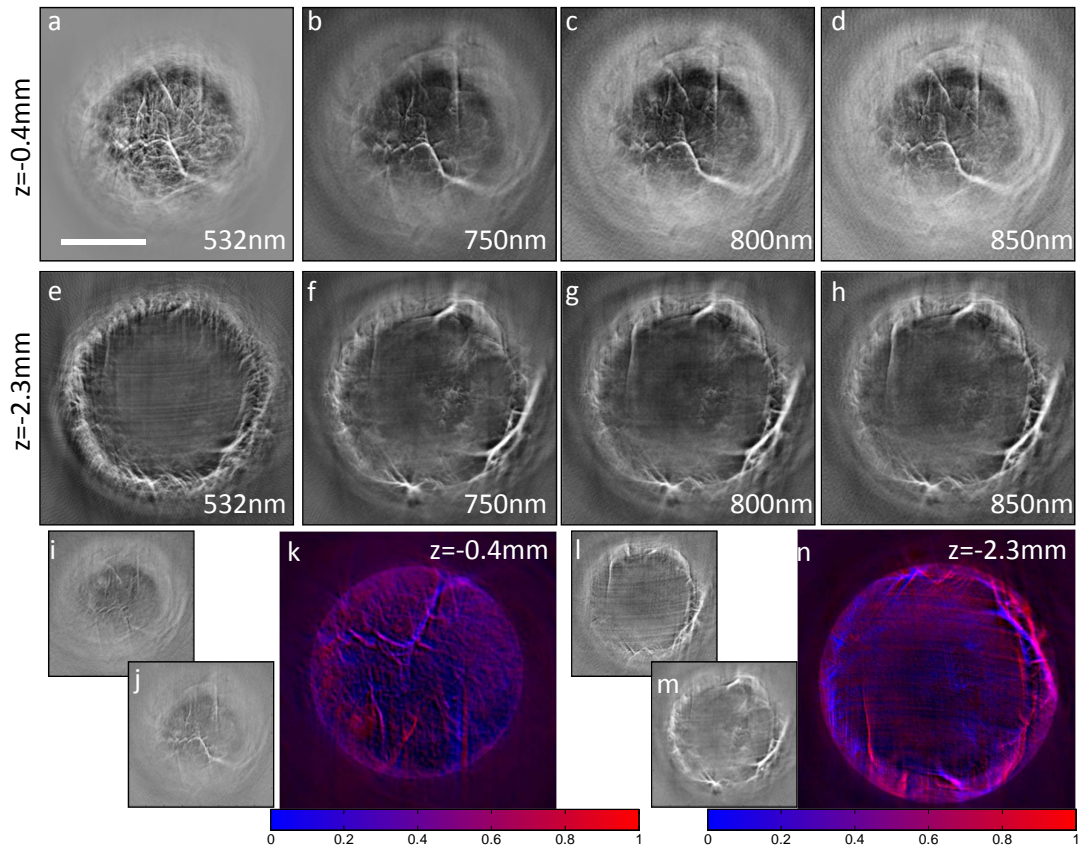


Figure A.4: Blood oxygenation derived by linear multispectral decomposition. a-d: Single wavelength optoacoustic tomography images acquired 0.4mm below the top of the tumor. e-h: Single wavelength optoacoustic tomography images acquired 2.3mm below the top of the tumor. i-j: Decomposed concentrations of oxygenated (i) and deoxygenated (j) hemoglobin 0.4mm below the top of the tumor. k: Pseudo-colored overlay of images (i) and (j), showing highly oxygenated blood in red and blood of low oxygenation in blue. i-j: Decomposed concentrations of oxygenated (i) and deoxygenated (j) hemoglobin 2.3mm below the top of the tumor. k: Pseudo-colored overlay of images (i) and (j), showing highly oxygenated blood in red and blood of low oxygenation in blue. NIR images are unprocessed to show the systematic performance. Scalebar 3mm.